FLEXOELECTRICITY AT SURFACE INSTABILITIES AND STRESS SINGULARITIES

Hossein Mohammadi

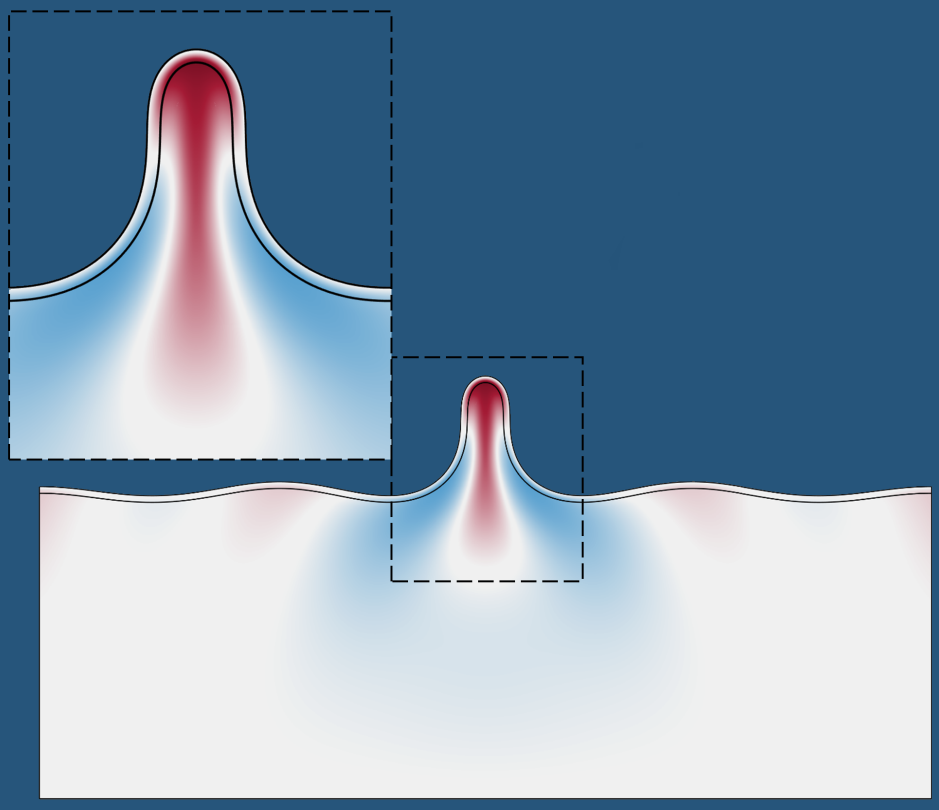

Doctoral Thesis
Barcelona, April 2023

FLEXOELECTRICITY AT SURFACE INSTABILITIES AND STRESS SINGULARITIES

Hossein Mohammadi

Doctoral Thesis
Advisor: Irene Arias
Barcelona, April 2023

School of Mathematics and Statistics
Doctoral Degree in Applied Mathematics
Universitat Politècnica de Catalunya

UNIVERSITAT POLITÈCNICA DE CATALUNYA
BARCELONATECH
Facultat de Matemàtiques i Estadística

Doctoral Degree in Applied Mathematics
School of Mathematics and Statistics
Universitat Politècnica de Catalunya

Flexoelectricity at surface instabilities and stress singularities

by

Hossein Mohammadi

LaCàN: Laboratory of Mathematical and Computational Modeling

Advisor: Irene Arias
Barcelona, April 6, 2023

“The important thing is not
to stop questioning.
Curiosity has its own reason
for existing.”
–Albert Einstein

Abstract

Flexoelectricity at surface instabilities and stress singularities

Hossein Mohammadi

The flexoelectric effect, the two-way linear coupling between strain gradient and electric polarization (direct flexoelectricity) or electric field gradient and strain (converse flexoelectricity) universally present in any dielectric, has given rise to a new research area referred to as strain gradient engineering in which in contrast to the conventional wisdom that views strain gradients as undesirable, researchers seek to mobilize strain gradients in a smart way to design sensors, actuators, and energy harvesting devises for next-generation micro/nano electromechanical systems. Ionic crystals with high dielectricity, such as ferroelectric perovskites at their paraelectric phase, achieve the best flexoelectric properties and have thus been a favorite to explore the flexoelectric effect. Nevertheless, large strain gradients are required for the flexoelectric effect to be noticeable. In these materials, large enough strain gradients are only achieved at very small scales. Soft and deformable materials, on the other hand, can endure large strains at larger scales before failure making them suitable candidates for the development of electromechanical devices. The focus of this thesis is two-fold, on the one hand, it explores novel ways to generate electricity in soft materials, including non-piezoelectric dielectric elastomers, under non-homogeneous fields. In particular, surface instabilities in flexoelectric film/ dielectric substrate are explored in depth. On the other hand, the manifestations of flexoelectricity on material behavior, in particular around stress singularities are explored.

Keywords: Flexoelectricity, Continuum mechanics, Mathematical modeling, Computational modeling, Surface instability.

Acknowledgments

First and foremost, I would like to express my sincere gratitude to my supervisor Prof. Irene Arias for giving me the opportunity to work in this exciting research area, for her valuable knowledge and support during these years, and for creating a research environment in which the quality of research is favored. I truly appreciate the freedom she gave me during these years to develop some independence and confidence.

I extend my gratitude to Prof. Dennis Kochmann for supporting me during my research stay at the Mechanics and Materials Laboratory at ETH Zurich, for the insightful discussions we had during my time there, and for the chance of being exposed to the broad range of topics in his group.

I want to acknowledge Prof. Sonia Fernández-Méndez and Prof. Marino Arroyo from whom I gained valuable insights about my research project. I also appreciate all the help and support received from the past and present researchers and colleagues in the FLEXOCOMP group, especially Dr. David Codony, Dr. Onofre Marco, Dr. Amir Abdollahi, Dr. Francessco Greco, Jordi Barceló-Mercader, and Juan Carlos Tarin.

I want to thank all of my amazing friends who shaped my experience over the last four years and supported me with valuable advice and encouraged me during difficult times.

Lastly, I would like to thank my parents, my siblings, and Banafsheh for their unconditional love, support, and empathy throughout my studies and my Ph.D.

I gratefully acknowledge the financial support of a fellowship from "laCaixa" foundation (ID 100010434). The fellowship code is LCF/BQ/DI20/11780036. I also acknowledge the support from the European Research Council (Starting Grant 679451 to Prof. Irene Arias).

Contents

List of Figures

List of Tables

Chapter 1

Introduction

1.1 Motivation

Electromechanical effects, the couplings between mechanical and electrical fields, have found significant applications in electromechanical transduction devices including sensors, actuators, and energy harvesters (Fig. 1.1) (Dagdeviren *et al.*, 2016). Sustainable power sources in consumer electronics (Beeby *et al.*, 2006), MEMS resonators for timing applications (Ng *et al.*, 2015), and sensors for blood pressure measurements (Terry *et al.*, 1990) are a few examples of the broad applications of electromechanics.

These effects are present in a wide variety of materials from engineered to biological materials and have been shown to play an important role in biological functions such as auditory sensing, swelling of neurons associated with action potentials, and protein mechanical motors including stress-activated ion channels (Nguyen *et al.*, 2013a).

Most current technologies for electromechanical transduction rely on the well-known piezoelectric effect. It refers to the two-way linear coupling between mechanical deformation and electric field (Fig. 1.2a) (Ikeda, 1996). This effect is present only in a specific class of dielectric materials, namely those exhibiting a non-centrosymmetric atomic or molecular structure. This intrinsic material polarity is an essential property of all piezoelectrics, from ionic crystals such as ferroelectrics, e.g Lead zirconate titanate (PZT) or barium titanate (Jaffe *et al.*, 1955), to piezoelectric polymers such as polyvinylidene difluoride (PVDF). The best-known piezoelectrics are ubiquitous in current technologies but exhibit limitations such as brittleness, toxicity, lack of biocompatibility, and a small range of operating temperatures (Haertling, 1999, Jaffe, 1958, Saito *et al.*, 2004, Stevenson *et al.*, 2015, Wu, 2020).

Beyond piezoelectricity, other electromechanical couplings have also been studied extensively, also as potential alternatives to piezoelectricity. On one hand, electrostriction, or the Maxwell-stress effect has received significant attention. It refers to the deformation universally induced in all dielectrics by an applied electric field, through the Coulombic attraction between the charges of the opposite sign located on both sides of the material (Fig. 1.2b).

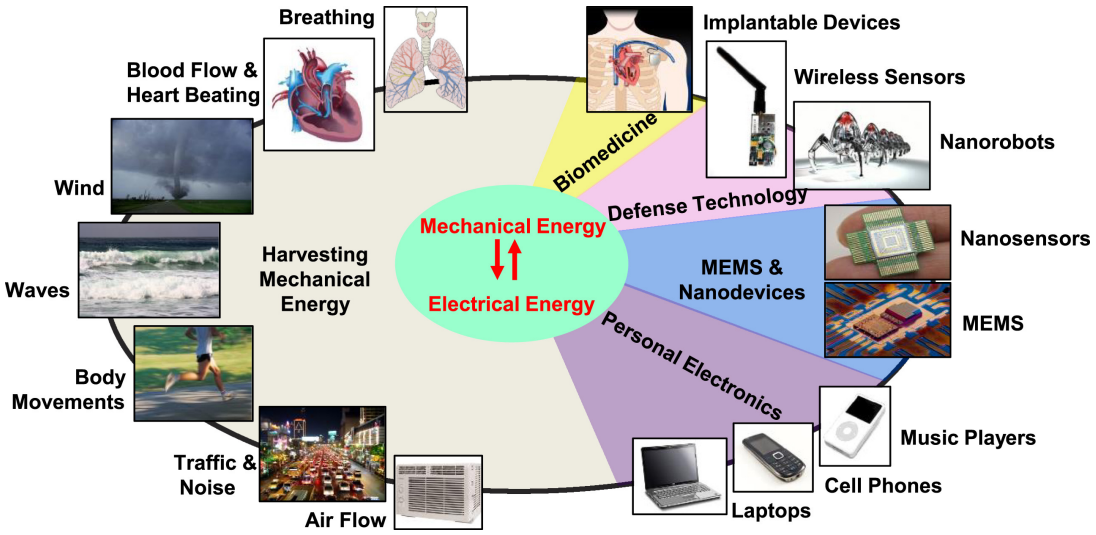

Figure 1.1: Broad applications of electromechanical transduction. Possible sources of energy harvesting (left) and its usage for sensing and actuation (right). Figure adapted from (Dagdeviren *et al.*, 2016).

The resulting strain depends quadratically on the applied electric field. Being significant in dielectric elastomers, it has been explored for technological applications (Kornbluh *et al.*, 1998, Lallart *et al.*, 2012, Pelrine *et al.*, 1997, 1998). These applications are limited to actuation since it is a one-way coupling as the deformation of a dielectric does not produce an electric field by electrostriction. Furthermore, this actuation is limited by the quadratic nature of the effect, as the reversal of the electric field does not reverse the sign of the deformation, and by the need for high voltages for actuation in most elastomers.

The third branch of electromechanical couplings namely flexoelectricity has been comparatively less understood and studied. In recent decades, due to its potential applications to overcome some of the limitations of other electromechanical couplings, flexoelectricity is increasingly attracting researchers' interest. A brief comparison between the electromechanical coupling mechanisms has been provided in Fig. 1.2.

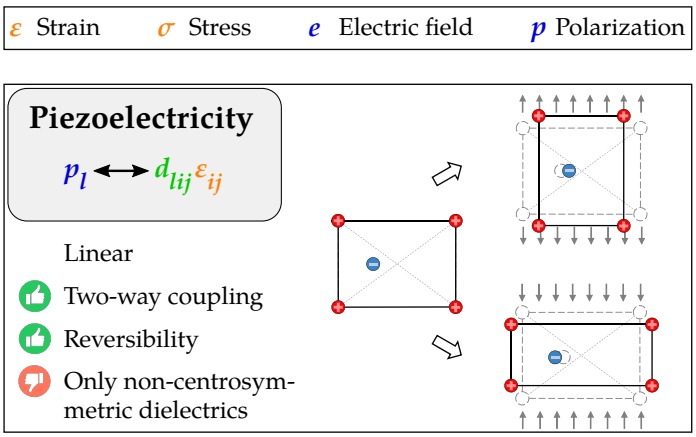

(a) Piezoelectricity

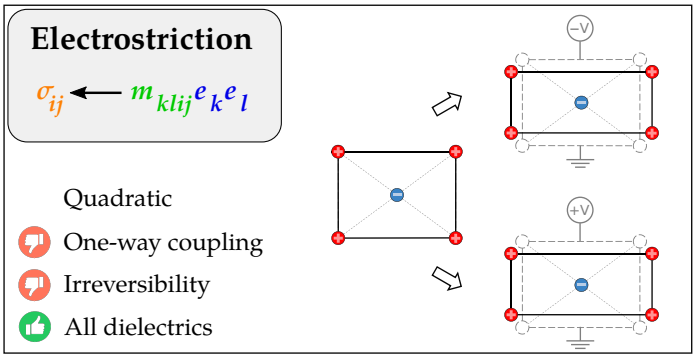

(b) Electrostriction

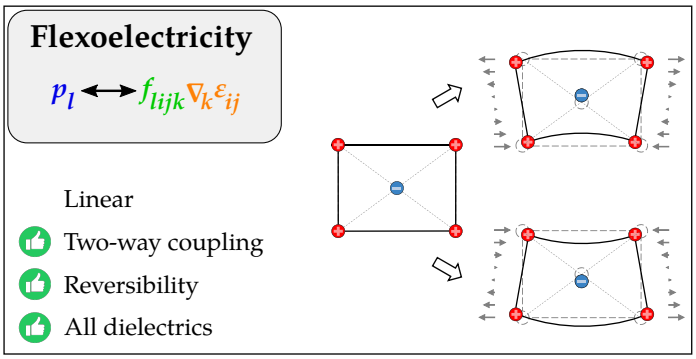

(c) Flexoelectricity

Figure 1.2: 2D sketches of different physics for electromechanical transduction in a crystalline dielectric. Figure adapted from (Codony, 2021).

1.2 Flexoelectricity

The flexoelectric effect is a two-way linear coupling between strain gradient and electric field (direct flexoelectricity) or between electric field gradient and strain (converse flexoelectricity). However, unlike piezoelectricity, which is only present in non-centrosymmetric dielectrics, flexoelectricity is a property of all dielectric materials including crystals, polymers, biomaterials, liquid crystals, etc. (Jiang *et al.*, 2013, Nguyen *et al.*, 2013b, Wang *et al.*, 2019a, Zubko *et al.*, 2013). In piezoelectric materials, under the application of a homogeneous mechanical loading, due to a lack of symmetry in the atomic structure of the material, an electric field is generated (Fig. 1.2a). In flexoelectric materials on the other hand, as a result of a non-uniform deformation applied on a crystalline dielectric material, regardless of its initial atomic structure symmetry, strain gradient can break its spatial inversion symmetry resulting in inducing electric response (Fig. 1.2c). Ionic crystals with high dielectric constant, such as ferroelectric perovskites at their paraelectric phase, exhibit the largest flexoelectric properties. Nevertheless, large enough field gradients are required for a noticeable flexoelectric response. Since gradients scale up with the decrease of the specimen size, large gradients can usually be found only at small-length scales. This implies that flexoelectricity may not be noticeable in larger scales (Jiang *et al.*, 2013, Nguyen *et al.*, 2013b, Wang *et al.*, 2019a).

The first theoretical (Mashkevich and Tolpygo, 1957), and experimental (Bursian and Zaikovskii, 1968) studies on flexoelectricity date back to the 50s and 60s. Over the past decade, several flexoelectric-based electromechanical prototypes such as sensors (Huang *et al.*, 2014, 2012, Kwon *et al.*, 2016, Merupo *et al.*, 2017), actuators (Bhaskar *et al.*, 2016, Zhang *et al.*, 2017) or energy harvesters (Choi and Kim, 2017, Deng *et al.*, 2014a, Zhu *et al.*, 2018) have been designed and fabricated. The concept of piezoelectric composites without piezoelectric materials (Sharma *et al.*, 2007) has enabled the design of geometrically polarized non-piezoelectric dielectrics with apparent piezoelectricity through flexoelectricity (Mocci *et al.*, 2021). In this concept, the flexoelectric response at small structural components is up-scaled to the macroscale, avoiding internal cancellation through geometrical polarization.

Apart from applications, several physical and biological phenomena such as triboelectricity (Fig. 1.3a) (Mizzi *et al.*, 2019, Mizzi and Marks, 2022), flexo-caloric effect (Liu *et al.*, 2016), flexo-photovoltaic effect (Fig. 1.3b) (Shu *et al.*, 2020, Yang *et al.*, 2018), auditory sensing (Breneman *et al.*, 2009, Deng *et al.*, 2019), bone self-repair and remodeling (Fig. 1.3c) (Vasquez-Sancho *et al.*, 2018) among others, have been explained by flexoelectricity which implies the growing significance of this electromechanical mechanism. Also, it has been shown that flexoelectricity can affect the physics of crack formation and propagation (Abdollahi *et al.*, 2015b, Cordero-Edwards *et al.*, 2019, Núñez-Toldrà *et al.*, 2020, Wang *et al.*, 2019c). Abdollahi *et al.* (2015b) showed that flexoelectricity can cause a toughening effect as well as a toughness asymmetry. The predicted toughness asymmetry (Abdollahi *et al.*, 2015b), has recently been evidenced in an experimental study (Fig 1.3d) (Cordero-Edwards *et al.*, 2019). Besides, Wang *et al.* (2019c) demonstrated the presence of a huge flexoelectric polarization around the crack tip which

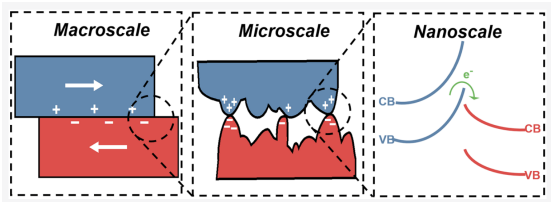

(a) Flexoelectricity as a potential driver of triboelectricity.

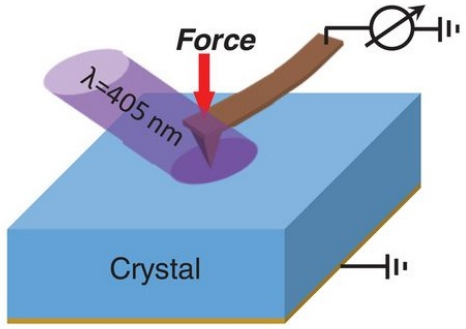

(b) Strain gradient induces bulk photovoltaic effect in centrosymmetric single crystals.

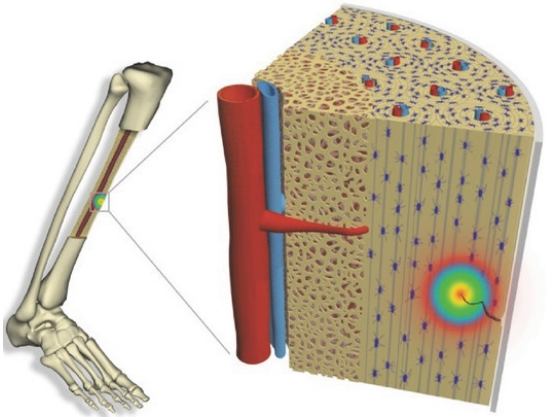

(c) Flexoelectricity has been suggested to be a potential mechanism behind bone self-repair and remodeling.

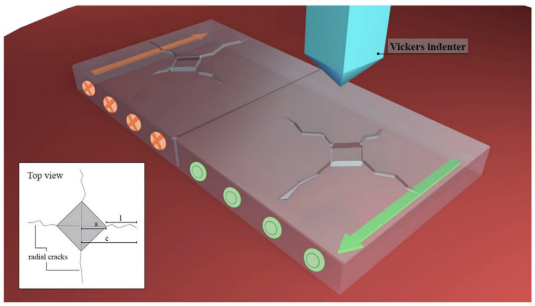

(d) Toughness asymmetry due to flexoelectricity.

Figure 1.3: Some examples of the physical manifestations of flexoelectricity. Figure adapted from (Cordero-Edwards *et al.*, 2019, Mizzi and Marks, 2022, Vasquez-Sancho *et al.*, 2018, Yang *et al.*, 2018).

reveals the relevance of flexoelectricity in the fracture phenomenon.

1.2.1 Flexoelectricity in soft materials

Soft robotics, biomedical devices, flexible electronics, energy harvesting, and sensors are some of the applications enabled by electroactive soft materials. In soft electromechanics, a device is generally required to simultaneously be able to (1) undergo large deformation under a moderate electric field and (2) generate a noticeable electric field under the application of moderate deformation. In the context of flexoelectricity, soft materials such as dielectric polymers can undergo large deformation enabling the possibility of achieving higher strain gradients and thus a potentially higher electric response at larger scales compared to hard crystalline materials. This can provide further opportunities to design soft functional biocompatible

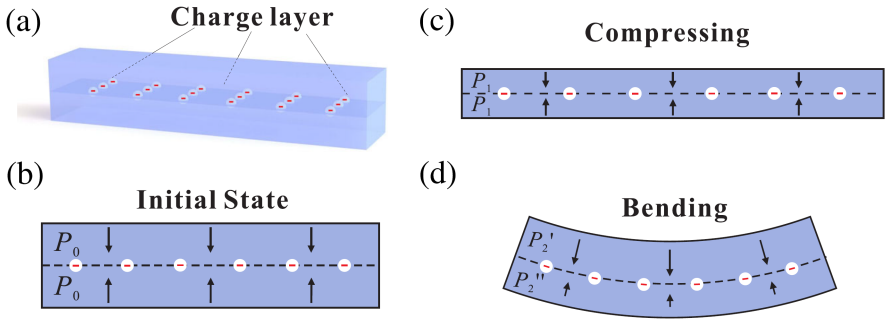

Figure 1.4: Schematic image of the mechanism of flexoelectrets. Figure adapted from (Wen *et al.*, 2019).

and environmentally friendly (soft and non-toxic) materials. Flexoelectricity emerges in soft materials such as liquid crystals or lipid bilayers due to the reorientation of irregularly shaped polarized molecules under strain gradients (Ahmadpoor *et al.*, 2013, Ahmadpoor and Sharma, 2015, Liu and Sharma, 2013, Meyer, 1969, Mohammadi *et al.*, 2014, Morozovska *et al.*, 2018, Petrov, 1999, Rey, 2006). However, since flexoelectricity is a size-dependent property being weaker at large scales, and the fact that the intrinsic flexoelectric coefficients of soft materials are considerably lower than that of dielectric ceramics (Wen *et al.*, 2019), how to enhance flexoelectric properties in soft materials has been an important question.

Deng *et al.* (2014b) developed a one-dimensional theoretical model for flexoelectricity in solids. They showed that the electromechanical coupling can be enhanced by combining the electret-Maxwell stress mechanism and flexoelectricity.

By depositing a layer of electrical charges on the middle plane of a soft beam and forming an electret (Fig.1.4-a,b), Rahmati *et al.* (2019) and Wen *et al.* (2019) proposed the generation of a flexoelectric-like effect in electrets under bending deformation. Under the application of uniform compression (Fig.1.4-c), the shape of the beam changes but remains symmetric with respect to the middle plane resulting in zero net polarization between upper and lower surfaces. Under bending (Fig.1.4-d), the symmetry of the bar is broken which causes a generation of net polarization along the thickness direction. Wen *et al.* (2019) showed that by depositing a charge layer with a surface potential of -5723 V, the apparent material's flexoelectric coefficient can be enhanced by two orders of magnitude. The same group in another study (Wen *et al.*, 2021) showed that the electrets can generate curvature in response to a uniform electric field.

Grasinger *et al.* (2021) developed a statistical-mechanics theory underpinning flexoelectricity in elastomers. They showed that giant flexoelectricity can be achieved in incompressible elastomers if the material is prestretched in the direction of the strain gradient.

Through a phenomenological model verified with experiments, Zhang et. al. (Zhang *et al.*, 2020a) showed that the flexoelectric coefficient of elastomers can be enhanced by increasing the cross-linking density of the elastomers.

1.2.2 Continuum modeling of flexoelectricity

The first continuum theory of flexoelectricity in soft materials goes back to the paper by Liu (Liu, 2014a) in which he proposed an energy formulation for a coupled magneto-electro-elasticity continuum in which based on the principle of minimum free energy, he derived the linear and nonlinear theories for different materials including dielectric elastomers, piezoelectric ceramics, ferroelectrics, flexoelectric materials, etc. Following that work, a few papers further developed the continuum theory of flexoelectricity in soft materials (McBride *et al.*, 2020, Nguyen *et al.*, 2019, Poya *et al.*, 2019, Thai *et al.*, 2018, Yvonnet and Liu, 2017, Zhuang *et al.*, 2020a). In contrast with previous works, Codony *et al.* (2020) presented a formulation with a fully material flexoelectric coupling between strain gradient and electric polarization, which yields an objective enthalpy functional by construction. Nevertheless, this and the previous works postulate an energy contribution for bulk flexoelectricity in which the strain gradient is coupled with a measure of electric response (either the electric displacement, the electric field, or the electric polarization), but neglecting the explicit coupling between the gradient of electric responses with strain (converse flexoelectricity). Although converse flexoelectricity is implicitly modeled in these formulations, this causes a non-symmetric flexoelectric response for direct and converse flexoelectricity unless boundary conditions are treated adequately. Besides, to model flexoelectricity in soft materials such as polymers, it is important to consider the incompressibility constraint in the elastic material model. Neglecting the incompressibility constraint may compromise the validity of the models for polymers and rubber-like materials.

Regardless of considering hard or soft materials, the governing equations of flexoelectricity are a coupled system of 4th-order partial differential equations. Solving them in the weak form, we require C1-continuous basis functions. This precludes the use of the standard finite element technique and commercial software such as ABAQUS using the C0-continuous basis function (which is continuous itself but not the derivatives). Meshfree (Abdollahi *et al.*, 2014), immersed boundary B-spline (Codony *et al.*, 2019), and body fitted B-spline (Codony *et al.*, 2020) approaches have been employed in our group to solve the governing equations of flexoelectricity. Several approaches have also been proposed in the literature including mixed finite element formulation (Deng *et al.*, 2017, Mao *et al.*, 2016), isogeometric analysis (Liu *et al.*, 2019, Thai *et al.*, 2018), C1 discretization with triangular elements (Yvonnet and Liu, 2017), and C0 interior penalty methods (Ventura *et al.*, 2021).

1.3 Surface instabilities in film/substrate systems

In recent years, several potential functionalities of surface instability-based systems have been demonstrated including biomimetic cell-culture substrates, stretchable super-hydrophobic coatings, pressure and strain sensors, supercapacitors, artificial muscle actuators, etc. (Bowden *et al.*, 1998, Cao *et al.*, 2014, Chen *et al.*, 2013, Park *et al.*, 2016, Stafford *et al.*, 2004, Wang *et al.*, 2011, Zang *et al.*, 2013).

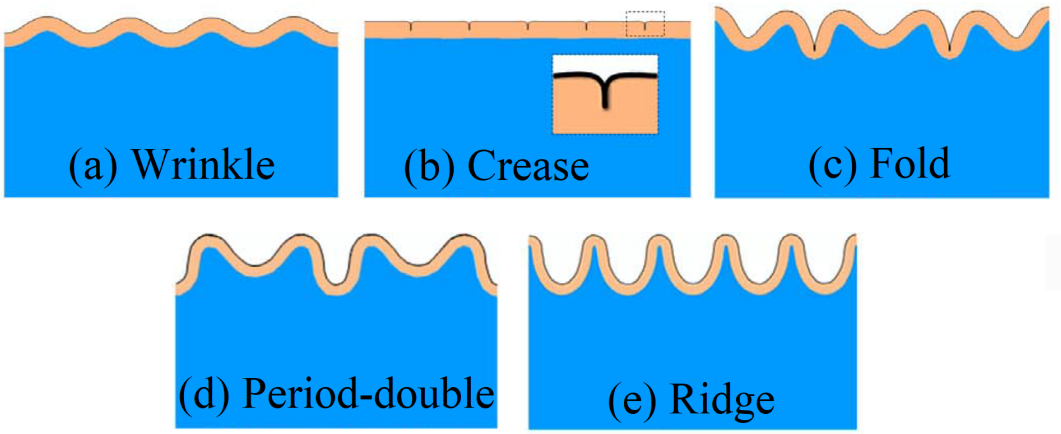

Figure 1.5: Schematics of surface instability patterns (a) Wrinkle, (b) Crease, (c) Fold, (d) Period-double, (e) Ridge. Figure adapted from (Wang and Zhao, 2015).

The early studies of wrinkling of film/substrate systems go back to the theoretical study of Allen (Allen, 1969) which focused on the prevention of instability of layered composites such as sandwich panels. Several papers in recent years have focused on the identification of various surface instability patterns (Fig. 1.5.) namely wrinkle (Cao and Hutchinson, 2012b), crease (Cai *et al.*, 2012), fold (Sun *et al.*, 2011), period-double (Budday *et al.*, 2015), and ridge (Cao *et al.*, 2014, Zang *et al.*, 2012) and the transitions between them (Auguste *et al.*, 2014, Brau *et al.*, 2013, 2011, Jin *et al.*, 2015, Wang and Zhao, 2014, 2015). In a two-dimensional case of a perfectly bound thin film/substrate system in which the substrate has been subjected to a prestretch, it has been shown that the bifurcation strain and surface instability patterns depend only on the modulus ratio and mismatch strain between film and substrate (Auguste *et al.*, 2014, Wang and Zhao, 2015).

Wang and Zhao (Wang and Zhao, 2015) constructed a three-dimensional phase diagram for the instability patterns in which three non-dimensional parameters (1) mismatch strain, (2) modulus ratio, and (3) normalized adhesion energy determine the instability pattern. The phase diagram for cases with high adhesion energies can be seen in Fig. 1.6.

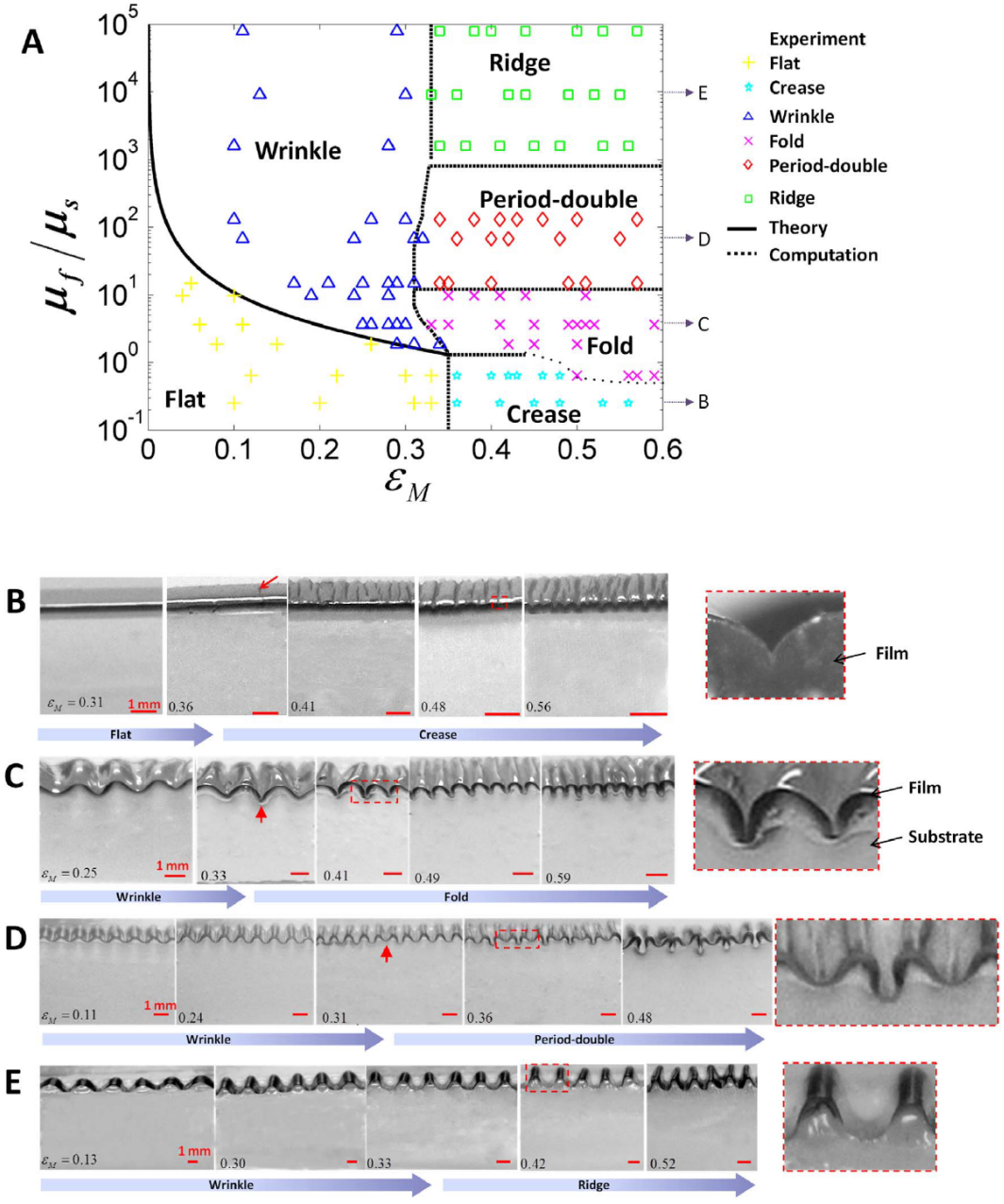

Figure 1.6: Phase diagram for instability patterns in a perfectly bound film/substrate system and its experimental validation. Figure adapted from (Wang and Zhao, 2015).

1.3.1 Electromechanical studies on surface instabilities

Several papers have studied the electromechanical instabilities of dielectric elastomers. Zhao and Suo (Zhao and Suo, 2007), proposed an approach for analyzing the electromechanical stability of dielectric elastomers. They showed that electromechanical instability occurs when the Hessian of free-energy function discontinues being positive definite. Stability analysis of min-max problems requires a different approach, i.e. the instability occurs when the signature of the global stiffness matrix changes (Dortdivanlioglu and Linder, 2019).

The wrinkling of dielectric elastomers has been investigated experimentally and theoretically (Kollosche *et al.*, 2012, Shui *et al.*, 2019, Su *et al.*, 2018b, Wang and Zhao, 2013, Zhu *et al.*, 2012). Su *et al.* (2019) investigated the bending deformation of a dielectric-elastic bilayer based on the nonlinear theory of electroelasticity and the associated linearized incremental field theory. They studied the stability of the bilayer and showed that the formation of patterns in the wrinkled bilayer can be controlled by tuning the physical properties of the bilayer and the applied voltage.

Surface instabilities such as wrinkling are sources of strain gradients, making this subject an attractive area for further investigations in the flexoelectric community. A common structure in stretchable electronics is a film/substrate system in which a thin layer of active material is bonded to a passive mostly compliant substrate (Dickey, 2017, Gong and Cheng, 2017, Wang *et al.*, 2018) which may develop surface instabilities due to strain mismatch between film and substrate.

Regarding the study of the surface instabilities in flexoelectric materials, through a theoretical study, Su *et al.* (2018a) investigated the wrinkling of a flexoelectric nano-film/substrate system and showed that both flexoelectricity and surface effects significantly change wrinkling critical condition and wrinkling deformation, especially at very small length scales. The same group in a theoretical study (Su *et al.*, 2021) proposed a flexoelectric energy harvester based on controllable wrinkling mechanism to enhance the energy harvesting efficiency. Shang *et al.* (2022) studied flexoelectricity in wrinkled thin films and demonstrated that increased flexoelectricity in thinner films can enhance the available energy and stretchability of the wrinkled thin films. Nevertheless, to the best of our knowledge, to this date, no computational framework is present in the literature to study surface instabilities in flexoelectric bilayers. In particular, a computational model that is able to study complex nonlinear instabilities such as folding and creasing in flexoelectric materials is not present in the literature.

1.4 Goals and objectives

The main objective of this thesis is to explore surface instabilities in soft materials to harness strain inhomogeneities and the flexoelectric effect. In particular, surface instabilities occurring in a film/substrate system are studied in detail. Surface instabilities in film/substrate systems have been shown to provide significant potential applications in the design of advanced

materials. As a result of surface instability in a film/substrate system, different patterns are formed on the surface in which a noticeable local strain gradient is generated. In dielectrics, this results in the generation of a localized electric response through direct flexoelectricity. Furthermore, as shown in (Wang and Zhao, 2015), depending on the relative stiffness of the thin film and the substrate, the adhesion energy, and strain, one can produce surface morphologies that are noncentrosymmetric, including buckle delaminations, folding, period doubling, and ridging (see Section 1.3). In these patterns, the geometrical polarization deriving from the lack of up-down symmetry gives rise to a net electrical response through the flexoelectric effect. In other situations without significant up-down symmetry, the internal cancellation of the flexoelectric fields should be prevented through proper device design. Therefore, the study of surface instabilities in an electromechanical continuum can provide further opportunities to design sensors, actuators, and energy harvesting systems exploiting the flexoelectric effect. Besides, it can highlight some fundamental manifestations of flexoelectricity on material behavior. Towards this goal, the specific objectives are:

- Study the surface effects that inherently exist in flexoelectric continuum models. We will study a general form of flexoelectric coupling in infinitesimal strains from which direct, converse, and Lifshitz-invariant flexoelectric models can be obtained. We will first show that when the body is infinite, flexoelectric materials do not show electromechanical response under homogeneous loading. However, when the size of the body is finite, due to the symmetry-breaking nature of surfaces, homogeneous loading (mechanical or electrical) can cause an electromechanical response near the surfaces. We will show that the electromechanical response is similar to surface piezoelectricity causing boundary layers in components of strains and electric fields near the surfaces. We will obtain closed-form solutions that can accurately describe the boundary layers.

- Extend the large deformation framework in (Codony *et al.*, 2020) to a symmetric flexoelectric formulation explicitly accounting for converse flexoelectricity (Lifshitz-invariant model), and to account for incompressibility and material interfaces. We will extend and implement the weak enforcement of interface conditions reported in (Barceló-Mercader *et al.*, 2022) to the large deformation setting. We will also implement the subdivision stabilization technique to circumvent the well-known locking phenomenon for the incompressibility constraint (Dortdivanlioglu *et al.*, 2018).

- Validate the formulation and implementation. Several numerical tests such as gradient checking, verification with the infinitesimal strain formulation for small loadings, convergence tests, etc. will be performed.

- Explore surface instabilities in a flexoelectric film/substrate system. First, we will study the system without flexoelectricity for validation. Then, we will address the full electromechanical problem and will aim at capturing the well-known mechanical instability patterns of wrinkling, creasing, folding, period-doubling, and ridging. In

order to gain understanding and ultimately control over the instability patterns, we will study in detail the transitions between them and their dependence on the model parameters (moduli ratio, substrate pre-stretch, etc.).

- Study the flexoelectricity-induced electromechanical response of each family of instability patterns and extract the design criteria for large-area flexoelectric devices with optimal flexoelectric performance. In particular, the effect of model parameters on the flexoelectricity-induced electrical response will be studied in detail. Possibilities for enhancing the response will be explored.
- Propose potential applications for flexoelectric devices employing surface instabilities.
- Explore the manifestations of flexoelectricity in stress singularities such as folds and sharp notches. We will show that flexoelectricity can result in a delaying effect in the formation of folds. Besides, we will show that flexoelectricity can contribute to notch strengthening effect and flaw-insensitive fracture.

1.5 Outline

The manuscript is organized as follows. Chapter 2 is devoted to the theoretical modeling of flexoelectricity. We first review the different formulations of flexoelectricity at infinitesimal strains (accounting explicitly for only direct or converse or both direct and converse flexoelectricity) regarding inherent finite sample effects. We then present a large-deformation continuum model for flexoelectricity accounting for converse flexoelectricity explicitly, material incompressibility, and multimaterial configurations. Chapter 3 explores different instability patterns in flexoelectric-dielectric bilayers and their flexoelectric-induced electromechanical response. Based on the understanding gained in this chapter, we propose in Chapter 4 several conceptual designs that lay the ground for soft large-area electromechanical materials and devices harnessing flexoelectricity as a functional property. Chapter 5 explores the effect of flexoelectricity on stress singularities such as folds in soft materials and notches in hard materials. Finally, Chapter 6 summarizes and concludes the dissertation.

1.6 List of publications

This manuscript gathers most of the published and unpublished (to this date) original research done by the author during his PhD. They are provided in the following lists.

1.6.1 Journal papers

- H. Mohammadi, O. Marco, I. Arias, Continuum modeling of surface instabilities in flexoelectric materials (To be submitted).

- H. Mohammadi, D. Codony, I. Arias, Flexoelectricity causes surface piezoelectric-like effect in dielectrics (To be submitted).
- H. Mohammadi, I. Arias, Gradient effects cause notch-strengthening and flaw insensitive fracture – contribution of flexoelectricity (To be submitted).

1.6.2 Other related publications

- F. Greco, D. Codony, H. Mohammadi, S. Fernandez, I. Arias, Topology optimization of flexoelectric metamaterials with apparent piezoelectricity (to be submitted).

1.6.3 Conference presentations

- H. Mohammadi, I. Arias, Computational modelling of surface instabilities in flexoelectric materials, 18th European Mechanics of Materials Conference (EMMC18) April 4 - 6, 2022, Oxford, UK.

Chapter 2

Continuum and computational modeling of flexoelectricity

In this chapter, with the aim of better understanding the flexoelectricity models, we first study finite sample effects in the different existing formulations of flexoelectricity, and in particular the emergence of surface-piezoelectric effects. For simplicity, we focus at this point on infinitesimal strains, but all drawn conclusions apply also to the large deformation setting. Next, following Codony *et al.* (2020), we present a Lifshitz-invariant formulation for flexoelectricity, explicitly accounting for both direct and converse flexoelectricity. This formulation is extended to multimaterial configurations and to material incompressibility. Finally, we present the computational model.

2.1 State of the art

After the early theoretical studies by Mashkevich and Tolpygo (1957) and Tolpygo (1963), Kogan (1964) proposed a phenomenological model for flexoelectricity in crystalline dielectrics. The distinction between piezoelectricity and flexoelectricity was clarified in Tagantsev (1986, 1991)'s first comprehensive theoretical works. Mindlin (1968) formalized the converse flexoelectric effect in elastic dielectrics in the mechanics community. Later, Sahin and Dost (1988) proposed a complete unified continuum framework that included strain gradient elasticity, direct and converse flexoelectric couplings, and the polarization inertia effect. Maranganti *et al.* (2006) recently proposed a simplified framework for isotropic dielectrics.

There are numerous continuum flexoelectricity theories currently available. Some of them reformulate the models using gradient elasticity theory (Askes and Aifantis, 2011b, Mindlin and Eshel, 1968b) variants such as couple-stress theory (Hadjesfandiari, 2013, Mindlin and Tiersten, 1962, Poya *et al.*, 2019) and rotation-gradient theory (Anqing *et al.*, 2015, Li *et al.*, 2015). Other authors consider couplings with additional physics, such as the flexoelectric effect in ferroelectrics (Catalan *et al.*, 2004, Eliseev *et al.*, 2009), coupling with magnetic fields

(Eliseev *et al.*, 2011, Liu, 2014b), or photovoltaics (Shu *et al.*, 2020, Yang *et al.*, 2018), as well as surface effects (Shen and Hu, 2010). General variational principles for flexoelectric materials can be found in Hu and Shen (2010), Liu (2014b), Shen and Hu (2010).

All of the aforementioned flexoelectricity theories can be classified based on the following criteria:

- The choice of variables describing the flexoelectric effect. For the mechanics, either the displacement gradient or its symmetrized form (i.e. strain) can be used, which gives rise to type-I or type-II flexoelectricity, respectively. For the dielectrics, either the electric polarization, the electric field, or the electric displacement is used.
- The considered flexoelectric coupling, either the direct, the converse, both, or the Lifshitz-invariant form.

2.1.1 Different flexoelectric models

The direct flexoelectric effect is defined as material polarization caused by inhomogeneous deformation (for example, bending or twisting) and is expressed mathematically as

$$p_l = f_{lijk}\frac{\partial \varepsilon_{ij}}{\partial x_k}, \tag{2.1}$$

where $\boldsymbol{f}$ is the flexocoupling tensor. There is also a thermodynamically conjugate converse flexoelectric effect, which involves the generation of stress $\boldsymbol{\sigma}$ as a result of the application of an inhomogeneous electric field $\boldsymbol{e}$, i.e.

$$\sigma_{ij} = f_{lijk}\frac{\partial e_l}{\partial x_k}. \tag{2.2}$$

Describing the bulk static flexoelectric effect in centrosymmetric dielectrics, the internal energy density under the assumption of infinitesimal deformations can be written in terms of the strain tensor $\boldsymbol{\varepsilon}$, the electric polarization field $\boldsymbol{P}$ and their corresponding spatial gradients in the following form (Codony *et al.*, 2021):

$$\begin{aligned}\psi^{(0)}(\boldsymbol{\varepsilon}, \nabla\boldsymbol{\varepsilon}, \boldsymbol{P}, \nabla\boldsymbol{P}) = &\frac{1}{2}c_{ijkl}\varepsilon_{ij}\varepsilon_{kl} + \frac{1}{2}h_{ijklmn}\varepsilon_{ij,k}\varepsilon_{lm,n} + \frac{1}{2}a_{kl}P_kP_l + \frac{1}{2}b_{ijkl}P_{i,k}P_{j,l}\\ &- f^{(1)}_{lijk}\varepsilon_{ij,k}P_l - f^{(2)}_{lijk}\varepsilon_{ij}P_{l,k},\end{aligned} \tag{2.3}$$

where

- $\boldsymbol{c}$ is the usual fourth-order elasticity tensor,
- $\boldsymbol{a}$ is the usual second-order reciprocal dielectric susceptibility tensor,
- $\boldsymbol{h}$ is the sixth-order strain gradient elasticity tensor, representing the purely non-local elastic effects,

- $\boldsymbol{b}$ is the fourth-order polarization gradient tensor, representing the purely non-local effects of polarization,
- $\boldsymbol{f}^{(1)}$ is the direct flexocoupling tensor,
- $\boldsymbol{f}^{(2)}$ is the polarization gradient-strain coupling tensor, also known as the converse flexocoupling tensor.

Assuming uniform material constants, the two latter terms in Eq. (2.3) can be rewritten as follows (Codony *et al.*, 2021):

$$\begin{aligned} -f^{(1)}_{lijk}\varepsilon_{ij,k}P_l - f^{(2)}_{lijk}\varepsilon_{ij}P_{l,k} &= \\ -f_{lijk}\varepsilon_{ij,k}P_l - f^{(2)}_{lijk}\frac{\partial\left(\varepsilon_{ij}P_l\right)}{\partial x_k} &= \qquad (2.4a)\\ f_{lijk}\varepsilon_{ij}P_{l,k} - f^{(1)}_{lijk}\frac{\partial\left(\varepsilon_{ij}P_l\right)}{\partial x_k} &= \qquad (2.4b)\\ -\frac{1}{2}f_{lijk}\left(\varepsilon_{ij,k}P_l - \varepsilon_{ij}P_{l,k}\right) - \frac{1}{2}\left(f^{(1)}_{lijk} + f^{(2)}_{lijk}\right)\frac{\partial\left(\varepsilon_{ij}P_l\right)}{\partial x_k}, & \qquad (2.4c) \end{aligned}$$

with the (effective) flexocoupling tensor

$$f_{lijk} = f^{(1)}_{lijk} - f^{(2)}_{lijk}. \qquad (2.5)$$

The first terms in (2.4a)-(2.4c) are referred to, respectively, as the *direct*, *converse* and *Lifshitz invariant* flexocouplings (Landau and Lifshitz, 2013, Lifshitz and Landau, 1984, Sharma *et al.*, 2010), and all of them implicitly represent both the direct and converse flexoelectric effects. The second terms in (2.4a)-(2.4c) are null-Lagrangians (Evans, 2010), as such their bulk integral can be written as a surface integral using the divergence theorem, e.g. for (2.4c):

$$\begin{aligned} \int_\Omega \frac{1}{2}\left(f^{(1)}_{lijk} + f^{(2)}_{lijk}\right)\frac{\partial\left(\varepsilon_{ij}P_l\right)}{\partial x_k}\,\mathrm{d}\Omega = \\ \int_\Gamma \frac{1}{2}\left(f^{(1)}_{lijk} + f^{(2)}_{lijk}\right)\varepsilon_{ij}P_l n_k\,\mathrm{d}\Gamma. \end{aligned} \qquad (2.6)$$

Despite the fact that they affect boundary conditions, null Lagrangians are frequently overlooked in the literature (Sharma *et al.*, 2010, Yudin and Tagantsev, 2013), resulting in different internal energy densities to Eq. (2.3) as

$$\psi^{(\mathrm{Dir})}(\boldsymbol{\varepsilon}, \nabla\boldsymbol{\varepsilon}, \boldsymbol{P}, \nabla\boldsymbol{P}) = \frac{1}{2}c_{ijkl}\varepsilon_{ij}\varepsilon_{kl} + \frac{1}{2}h_{ijklmn}\varepsilon_{ij,k}\varepsilon_{lm,n} + \frac{1}{2}a_{kl}P_kP_l + \frac{1}{2}b_{ijkl}P_{i,j}P_{k,l} - f_{lijk}\varepsilon_{ij,k}P_l, \qquad (2.7)$$

$$\psi^{(\mathrm{Con})}(\boldsymbol{\varepsilon}, \nabla\boldsymbol{\varepsilon}, \boldsymbol{P}, \nabla\boldsymbol{P}) = \frac{1}{2}c_{ijkl}\varepsilon_{ij}\varepsilon_{kl} + \frac{1}{2}h_{ijklmn}\varepsilon_{ij,k}\varepsilon_{lm,n} + \frac{1}{2}a_{kl}P_kP_l + \frac{1}{2}b_{ijkl}P_{i,j}P_{k,l} + f_{lijk}\varepsilon_{ij}P_{l,k}, \qquad (2.8)$$

and

$$\psi^{(\mathrm{Lif})}(\boldsymbol{\varepsilon}, \nabla\boldsymbol{\varepsilon}, \boldsymbol{P}, \nabla\boldsymbol{P}) = \frac{1}{2}c_{ijkl}\varepsilon_{ij}\varepsilon_{kl} + \frac{1}{2}h_{ijklmn}\varepsilon_{ij,k}\varepsilon_{lm,n} + \frac{1}{2}a_{kl}P_kP_l + \frac{1}{2}b_{ijkl}P_{i,j}P_{k,l} - \frac{1}{2}f_{lijk}\left(\varepsilon_{ij,k}P_l - \varepsilon_{ij}P_{l,k}\right). \quad (2.9)$$

Taking polarization field $\boldsymbol{P}$ as the electrical state variable results in a variational formulation in terms of the free energy of the system such that, upon minimization over the admissible states, Euler-Lagrange equations and boundary conditions follow as necessary conditions. However, in these formulations, the irrotationality of the electric field emerges as a constraint that complicates the numerical treatment. Therefore, many authors prefer electric field-based models to polarization-based models because the electric field can be irrotational by construction yielding an unconstrained min-max problem. The connection between the two families of models is Legendre transformation. Therefore, in this dissertation, we resort to electric field-based formulations.

2.1.2 Flexoelectric formulation based on electromechanical enthalpy

We consider a general form of flexoelectric coupling from which different forms such as direct, converse, and Lifshitz-invariant flexoelectric models can be derived. In the limit of infinitesimal deformations, the electromechanical enthalpy can be written as:

$$\begin{aligned}\mathcal{H}\left(\varepsilon_{ij}, \varepsilon_{ij,k}, E_l, E_{l,m}\right) =& \frac{1}{2}\mathbb{C}_{ijkl}\varepsilon_{ij}\varepsilon_{kl} + \frac{1}{2}h_{ijklmn}\varepsilon_{ij,k}\varepsilon_{lm,n} + \zeta\mu_{lijk}\varepsilon_{ij}E_{l,k} - (1-\zeta)\mu_{lijk}\varepsilon_{ij,k}E_l \\ & - \frac{1}{2}\kappa_{lm}E_lE_m - \frac{1}{2}M_{ijkl}E_{i,j}E_{k,l},\end{aligned} \quad (2.10)$$

where $\zeta = 0$ is related to the direct model, $\zeta = 1$ is related to the converse model, and $\zeta = 0.5$ is related to the Lifshitz-invariant model. In Eq. (2.10), $\mathbb{C}$ is the elasticity tensor, $\boldsymbol{h}$ is the strain gradient elasticity tensor, $\boldsymbol{\mu}$ is the flexoelectricity tensor, $\boldsymbol{\kappa}$ is the dielectricity tensor, and $\boldsymbol{M}$ is the gradient dielectricity tensor. The material tensors have been defined in Appendix A. The constitutive equations are:

$$\hat{\sigma}_{ij} = \frac{\partial\mathcal{H}}{\partial\varepsilon_{ij}} = \mathbb{C}_{ijkl}\varepsilon_{kl} + \zeta\mu_{lijk}E_{l,k}, \quad (2.11)$$

$$\tilde{\sigma}_{ijk} = \frac{\partial\mathcal{H}}{\partial\varepsilon_{ij,k}} = h_{ijklmn}\varepsilon_{lm,n} - (1-\zeta)\mu_{lijk}E_l, \quad (2.12)$$

$$\hat{D}_l = -\frac{\partial\mathcal{H}}{\partial E_l} = \kappa_{lm}E_m + (1-\zeta)\mu_{lijk}\varepsilon_{ij,k}, \quad (2.13)$$

$$\widetilde{D}_{ij} = -\frac{\partial\mathcal{H}}{\partial E_{i,j}} = M_{ijkl}E_{k,l} - \zeta\mu_{lijk}\varepsilon_{ij}. \quad (2.14)$$

The physical stress and physical electric displacement are:

$$\sigma_{ij} = \frac{\partial \mathcal{H}}{\partial \varepsilon_{ij}} - \left(\frac{\partial \mathcal{H}}{\partial \varepsilon_{ij,k}} \right)_{,k} = \mathbb{C}_{ijkl}\varepsilon_{kl} + \mu_{lijk}E_{l,k} - h_{ijklmn}\varepsilon_{lm,nk}, \tag{2.15}$$

and

$$D_i = \frac{\partial \mathcal{H}}{\partial E_i} - \left(\frac{\partial \mathcal{H}}{\partial E_{i,j}} \right)_{,j} = \kappa_{ij}E_j + \mu_{ijkl}\varepsilon_{jk,l} - M_{ijkl}E_{k,lj}. \tag{2.16}$$

The strong form of the problem can be written as:

$$\begin{cases} \sigma_{ij,j} + f_i^{ext} = 0 \quad \text{in } \Omega, \\ D_{l,l} - q = 0 \quad \text{in } \Omega, \end{cases} \tag{2.17}$$

where f_i^{ext} is the external body forces per unit volume, and q represents the external electric free charges per unit volume. The strong form is complemented with the following Neumann boundary conditions (Codony *et al.*, 2021):

$$\left(\hat{\sigma}_{ij} - \tilde{\sigma}_{ijk,k} + \nabla_l^S(n_l)\tilde{\sigma}_{ijk}n_k\right) n_j - \nabla_j^S(\tilde{\sigma}_{ijk}n_k) = t_i \quad \text{on } \partial\Omega_t, \tag{2.18}$$

$$\tilde{\sigma}_{ijk}n_j n_k = r_i \quad \text{on } \partial\Omega_r, \tag{2.19}$$

$$-\left(\hat{D}_l - \widetilde{D}_{lk,k} + \nabla_i^S(n_i)\widetilde{D}_{lk}n_k\right) n_l + \nabla_l^S(\widetilde{D}_{lk}n_k) = w \quad \text{on } \partial\Omega_w, \tag{2.20}$$

$$-\widetilde{D}_{jk}n_j n_k = v \quad \text{on } \partial\Omega_v, \tag{2.21}$$

where $\boldsymbol{n}$ is the normal vector to the surface, $\boldsymbol{t}$ is traction, $\boldsymbol{r}$ is double traction, $\boldsymbol{w}$ is surface charge density, $\boldsymbol{v}$ is double charge density. In regions where the boundary is not smooth, some additional boundary conditions arise. The reader is referred to (Codony *et al.*, 2021) for more details.

2.2 Finite sample effects

The flexoelectric couplings, which were first predicted theoretically (Mashkevich and Tolpygo, 1957) have since been confirmed experimentally. Bursian and Zaikovskii (1968) demonstrated beam bending of non-piezoelectric thin cantilever beams under applied electric bias in closed circuit (Fig. 2.1a), an evidence of inverse flexoelectricity producing non-homogeneous deformations in response to an applied homogeneous electric field (see Eq. (2.1)). This effect has been later used in proof-of-concept flexoelectric MEMS (Bhaskar *et al.*, 2016). Ma and Cross (2001, 2002) and Cross (2006) conducted a series of experiments showing electric fields emerging in cantilever nanobeams under bending and nanopyramids under compression, a testament of the direct flexoelectric effect (Fig. 2.1b). The flexoelectric response induced by mechanical gradients has been shown to be strong enough to: (1) switch polarization in

ferroelectrics, which opens avenues for mechanical writing of ferroelectric memories without any electrical bias (Lu *et al.*, 2012), (2) change the conductivity of LAO/STO interfaces by purely mechanical means, which can find application in transistors (Sharma *et al.*, 2015), and (3) provide a charge separation mechanism in non-centrosymmetric materials for photovoltaic applications (Yang *et al.*, 2018). Finally, deformation under in-homogeneous electric fields due to converse flexoelectricity has been observed in Piezoresponse Force Microscopy (PFM) (Fig. 2.1c) (Abdollahi *et al.*, 2019). All these settings have been successfully modeled with the self-consistent two-way coupled electromechanical continuum framework described in Section 2.1.2, demonstrating the ability of the model to capture flexoelectric physics (Abdollahi *et al.*, 2015a, 2019, 2014, Codony *et al.*, 2021).

In all three flexoelectric mechanisms, the actuating field, namely a mechanical gradient (direct), an electric field (inverse) and an electric field gradient (converse) are polar in nature and thus able by themselves to break material centro-symmetry. This is not expected to happen under homogeneous strain, cf. Section 1.2. Indeed, the self-consistent simulation of a non-piezoelectric dielectric square sample with generalized periodic boundaries (Barceló-Mercader *et al.*, 2023), i.e. representing an infinite medium, under uniform compression shows no flexoelectric response as expected (Fig. 2.2b). Interestingly, simulations in finite samples for all three models in Section 2.1.2 exhibit a boundary layer in the electric potential or the strain, which vanishes in the bulk as expected (Fig. 2.2c). This boundary layer emerges naturally from the model in the presence of a free surface. Intuitively, this localized electric response can be viewed as the piezoelectric-like response of a thin layer of material close to the free surface. It is thus reminiscent of surface piezoelectricity. This effect manifests itself in finite samples as an emerging thin piezoelectric boundary layer resulting from symmetry loss at the surface (Fig. 2.3) (Zubko *et al.*, 2013).

Regardless of the intrinsic symmetry of the bulk material, the presence of a free surface breaks the symmetry by surface relaxation and induces the emergence of a thin layer of non-centrosymmetric material with piezoelectric-like behavior. Surface piezoelectricity has been modeled as a zero-thickness layer of piezoelectric material, in the spirit of (Tagantsev and Yurkov, 2012, Yudin and Tagantsev, 2013, Yurkov and Tagantsev, 2016). However, it is known that surface relaxation can be described by strain gradient elasticity (Danescu, 2012). Similarly, here a piezoelectric-like boundary layer emerges naturally from the rich continuum model, without a specific ad-hoc model for surface piezoelectricity. Similar to the boundary layers in strain gradient elasticity models (Lam *et al.*, 2003, Shu *et al.*, 1999), the observed boundary layers present an exponential growth near the surfaces, and their width is directly related to the length scale parameters of the inherent higher-order physics.

An in-depth understanding of the inherent surface effects of flexoelectric models is essential from modeling, computational, and physical perspectives. From the modeling side, the emergence of boundary layers from surface relaxation in the flexoelectric models in Section 2.1.2 needs to be taken into account when incorporating ad-hoc surface piezoelectricity models such as the zero-thickness piezoelectric surface layer as done in Dai *et al.* (2011) and Pan *et al.* (2011).

Furthermore, a rigorous characterization of the boundary layers provides an opportunity to model surface effects resulting from surface relaxation as an emergent property. Obviously, surface effects resulting from physical or chemical surface specificity cannot be captured by the present rich continuum models. On the computational side, the inherent surface effects of the flexoelectric models can cause steep boundary layers resulting in numerical instabilities if the computational mesh is not sufficiently fine. Quantitative knowledge of the inherent surface effects of the flexoelectric models can be a useful guide for careful consideration of the mesh size and/or regularization parameters. Finally, the detailed study of specific boundary value problems based on the rich continuum models can provide further insights on the physics of the free surface effects.

In the following sections, we present a theoretical exploration and characterization of the observed boundary layers. We first study two examples in which a homogeneous electric field or strain causes surface effects in a thin flexoelectric film. As an additional example, we then explore the uniform bending of a flexoelectric beam showing that it exhibits surface effects that could be well-explained with the surface effects seen due to the application of homogeneous strain.

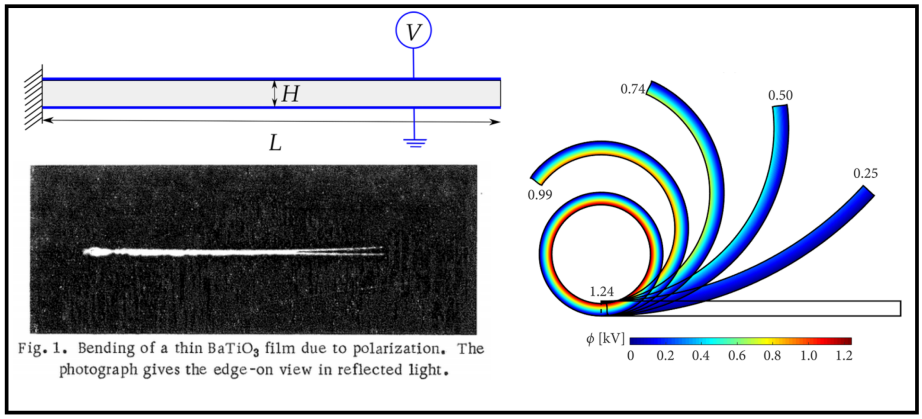

Fig. 1. Bending of a thin $BaTiO_3$ film due to polarization. The photograph gives the edge-on view in reflected light.

(a) Inverse flexoelectricity in experiments and simulations. Figure adapted from (Bursian and Zaikovskii, 1968, Codony *et al.*, 2021).

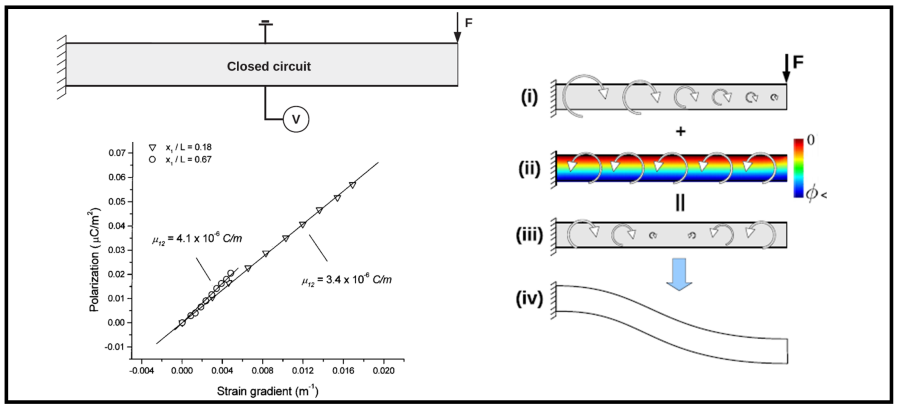

(b) Direct flexoelectricity in experiments and simulations. Figure adapted from (Abdollahi *et al.*, 2014, Ma and Cross, 2001).

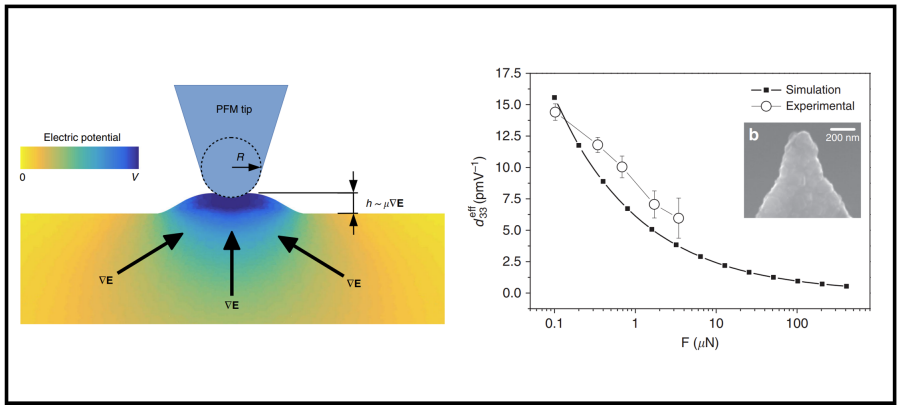

(c) Converse flexoelectricity in experiments and simulations. Figure adapted from (Abdollahi *et al.*, 2019).

Figure 2.1: Inverse, direct, and converse flexoelectricity has been observed in experiments and self-consistent computational simulations.

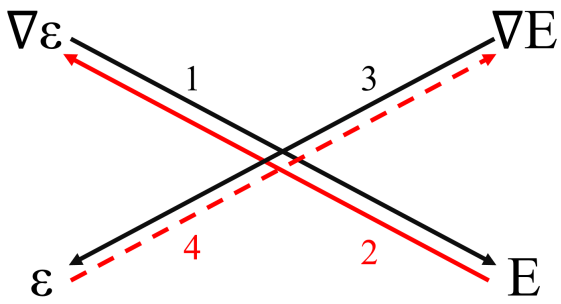

(a) Four-way coupling in the continuum models of flexoelectricity namely (1) direct flexoelectricity, (2) inverse flexoelectricity, (3) converse flexoelectricity, (4) inverse-converse flexoelectricity. The first three phenomena have been confirmed experimentally, while the fourth one has not yet been observed.

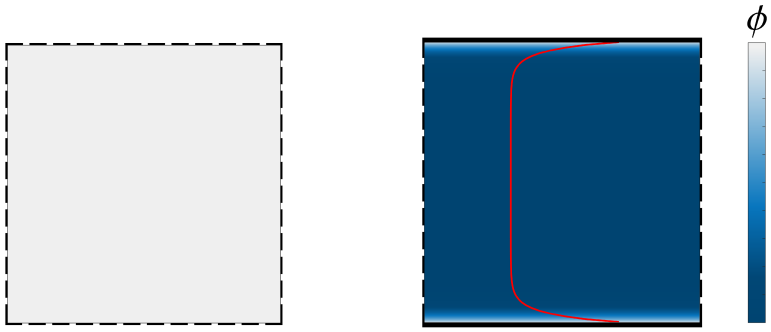

(b) Horizontal Compression of an infinite flexoelectric body (periodic in x and y directions) does not induce any electric response, as symmetry is not broken with compression. The distribution of electric potential has been plotted. The Lifshitz-invariant model has been used.

(c) Horizontal compression of an infinite flexoelectric film (periodic in x but not in y direction) induces an electric response close to the free top and bottom boundaries, as surfaces are sources of symmetry-breaking. The distribution of electric potential has been plotted. Horizontal surfaces are assumed to be free of tractions and surface charges. The Lifshitz-invariant model has been used.

Figure 2.2: The inverse phenomena (couplings shown with red arrows) can cause surface effects in flexoelectric models in finite samples.

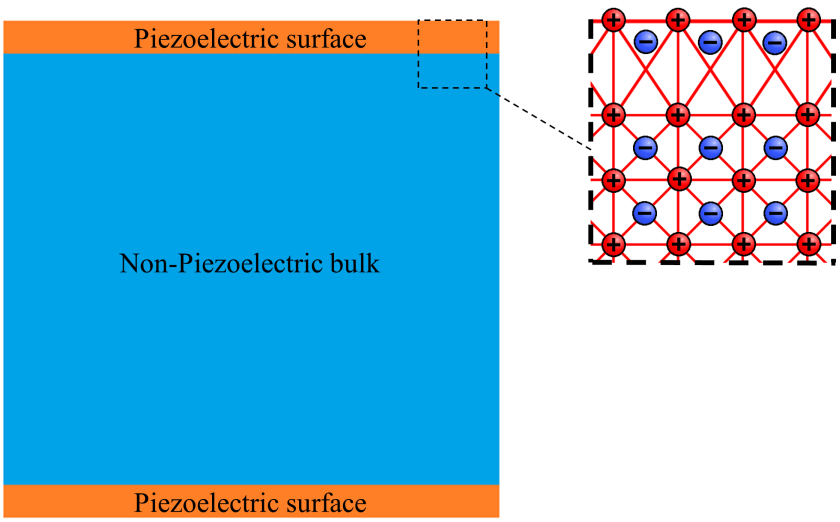

Figure 2.3: Symmetry breaking nature of surfaces causes a piezoelectric-like behavior of a thin layer of material close to free surfaces. Figure adapted from (Zubko *et al.*, 2013).

2.2.1 Analytical solutions for different cases

We provide next the analytical solution for three boundary value problems corresponding to a plane-strain microbeam under three loading conditions: axial electric actuation (Fig. 2.4a), axial compression (Fig. 2.4b), and uniform bending (Fig. 2.4c). For all the examples, we consider a thin flexoelectric film along the x-direction occupying $[-T/2, T/2]$ in the y-coordinate. The thin film is modeled as being infinite along x and z directions, for one-dimensional kinematics. For the described geometry, the boundary conditions presented in Eqs. (2.18)-(2.21) simplify to:

$$t_i = \sigma_{i2}\,\mathrm{sign}(y) \qquad \text{on } y = \pm T/2, \tag{2.22}$$

$$r_i = \tilde{\sigma}_{i22} \qquad \text{on } y = \pm T/2, \tag{2.23}$$

$$w = -D_2\,\mathrm{sign}(y) \qquad \text{on } y = \pm T/2, \tag{2.24}$$

$$v = -\widetilde{D}_{22} \qquad \text{on } y = \pm T/2. \tag{2.25}$$

Homogeneous Neumann mechanical and electric boundary conditions have been considered on the free surfaces for all the cases, i.e. $t_i = 0$, $r_i = 0$, $w = 0$, and $v = 0$. The obtained analytical results have been illustrated for each case considering a BST microbeam of thickness $T = 1$ micrometer. The material properties are given in Table 2.1. Worth noting that all analytical results have been verified against numerical simulations.

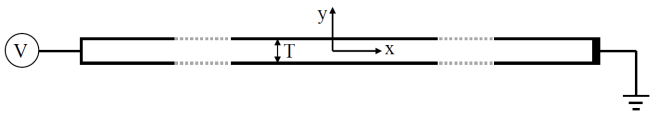

(a) Electrical actuation of a thin film along its length.

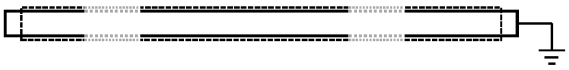

(b) In-plane compression of a thin film along its length.

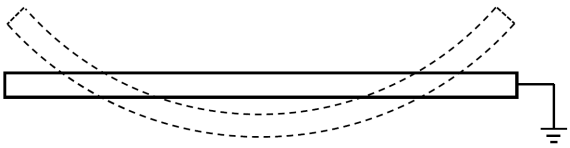

(c) Uniform bending of a thin film.

Figure 2.4: Loadings and boundary conditions of three cases studied in the paper. Dark dashed lines represent the deformed shape.

Table 2.1: Material parameters used in the simulation.

E [Gpa]	ν	l_1 [nm]	κ [nC/Vm]	l_2 [nm]	μ_L [μC/m]	μ_T [μC/m]	μ_S [μC/m]
152	0.33	20	8	30	1.21	1.10	0.055

2.2.1.1 Axial Electric actuation of a microbeam

Suppose we apply a far-field horizontal electric field $\bar{E}_x$ to the system. Fig. 2.4a shows the boundary conditions and loadings for this case. Consequently, the applied electric field results in y-dependent shear strain $\varepsilon_{xy}(y) = \varepsilon_{yx}(y)$. Here we consider strain-free conditions at infinity so that $\varepsilon_{xx} = \varepsilon_{yy} = 0$ and $E_y = 0$. However, as shown in Appendix H, the stress $\sigma_{xx} = 0$ on each cross-section which implies that the conclusions are not affected by the choice of stress or strain-free boundary conditions at infinity. Therefore:

$$\boldsymbol{\varepsilon} = \begin{bmatrix} 0 & \varepsilon_{xy}(y) \\ \varepsilon_{xy}(y) & 0 \end{bmatrix}, \qquad \boldsymbol{E} = \begin{bmatrix} \bar{E}_x \\ 0 \end{bmatrix}. \tag{2.26}$$

Considering homogeneous Neumann boundary conditions on the free surfaces, $\varepsilon_{xy}(y)$ can be obtained as:

$$\varepsilon_{xy}(y) = \frac{-(1-\zeta)\mu_S \bar{E}_x}{(1+\exp(-T/l_1))\, C_S l_1} \left[\exp\left(\frac{-y - T/2}{l_1} \right) - \exp\left(\frac{y - T/2}{l_1} \right) \right]. \tag{2.27}$$

The details of the derivation of the solution are provided in Appendix H.

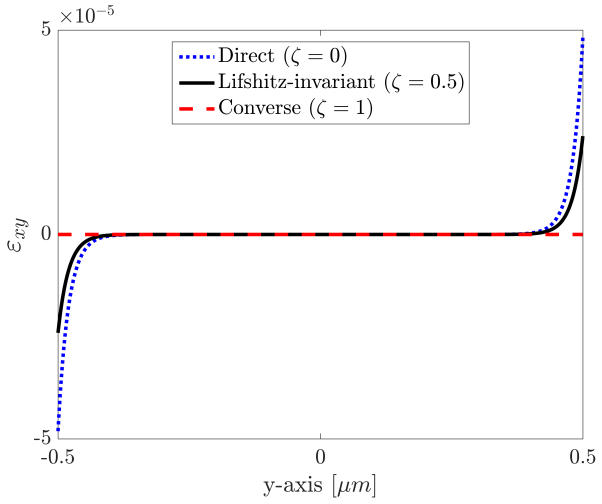

Figure 2.5: Electrical actuation of a thin flexoelectric film made of BST along its length with $\bar{E}_x = 1 V/\mu m$ shows inverse surface piezoelectric-like effect. The thickness considered here is 1 μm.

Fig. 2.5, depicts ε_{xy} along the cross-section, Eq. (2.27), for different flexoelectric models. Fig. 2.5 shows that for direct and Lifshitz-invariant models, as a result of the applied in-plane electric field the top and bottom surfaces of the body experience shear strains. The shear strain vanishes at a certain distance from the surfaces. The profile of the shear strain is controlled by the strain gradient elasticity length scale l_1 and its magnitude is proportional to the applied electric field $\bar{E}_x$ and the shear flexoelectric coefficient μ_S, and is inversely proportional to the shear component of the elasticity tensor C_S, and the strain gradient elasticity length scale l_1. This behavior is similar to the actuation of a thin layer of a piezoelectric surface due to an application of external voltage, or inverse surface piezoelectricity. Fig. 2.5 shows that for this case, the converse model does not show surface effect.

2.2.1.2 Axial compression of a microbeam

Suppose we apply far-field plane-strain axial compression $\bar{\varepsilon}_{xx}$ to the microbeam, Fig. 2.4b. Both the deformation field and electric potential are independent of the x-direction. Therefore, the applied compression results in y-dependent vertical strain $\varepsilon_{yy}(y)$ and electric field $E_y(y)$. Note that $\varepsilon_{xy} = \varepsilon_{yx} = 0$ and $E_x = 0$. Therefore:

$$\boldsymbol{\varepsilon} = \begin{bmatrix} \bar{\varepsilon}_{xx} & 0 \\ 0 & \varepsilon_{yy}(y) \end{bmatrix}, \qquad \boldsymbol{E} = \begin{bmatrix} 0 \\ E_y(y) \end{bmatrix}. \tag{2.28}$$

Considering homogeneous Neumann boundary conditions on the free surfaces, $E_y(y)$ and $\varepsilon_{yy}(y)$ can be obtained with the following expressions:

$$E_y(y) = K\frac{\bar{\varepsilon}_{xx}(C_L\mu_T - C_T\mu_L)}{\epsilon C_L}\Bigg[-\beta_2\left[\exp\left(\frac{-y - T/2}{a_1}\right) - \exp\left(\frac{y - T/2}{a_1}\right)\right] + \beta_1\left[\exp\left(\frac{-y - T/2}{a_2}\right) - \exp\left(\frac{y - T/2}{a_2}\right)\right]\Bigg], \tag{2.29}$$

$$\varepsilon_{yy}(y) = K\frac{\bar{\varepsilon}_{xx}(C_L\mu_T - C_T\mu_L)}{\mu_L C_L}\Bigg[-a_1\alpha_1\beta_2\left[\exp\left(\frac{-y - T/2}{a_1}\right) + \exp\left(\frac{y - T/2}{a_1}\right)\right] + a_2\alpha_2\beta_1\left[\exp\left(\frac{-y - T/2}{a_2}\right) + \exp\left(\frac{y - T/2}{a_2}\right)\right]\Bigg] - \frac{C_T}{C_L}\bar{\varepsilon}_{xx}, \tag{2.30}$$

where

$$K = \frac{\zeta}{a_1\beta_2\gamma_1 - a_2\beta_1\gamma_2}, \tag{2.31}$$

$$a_1, a_2 = \sqrt{l_1 l_2}\sqrt{\frac{A}{1 \pm \sqrt{1 - A^2}}}, \quad A = \frac{2l_1 l_2}{l_1^2 + l_2^2 + l_\mu^2}, \tag{2.32}$$

$$l_\mu^2 = \frac{\mu_L^2}{C_L \epsilon}, \tag{2.33}$$

$$\alpha_i = 1 - \frac{l_2^2}{a_i^2}, \tag{2.34}$$

$$\beta_i = (1 - \exp(-T/a_i)) \left(\frac{l_1^2}{l_\mu^2} \alpha_i + 1 - \zeta \right), \tag{2.35}$$

$$\gamma_i = (1 + \exp(-T/a_i)) \left(\frac{l_2^2}{a_i^2} (1 - \zeta) + \zeta \right). \tag{2.36}$$

The details of the derivation of the solution are provided in Appendix I. Note that in Eqs. (2.35), and (2.36), the thickness dependence of β_i and γ_i vanishes if $T \gg a_i$.

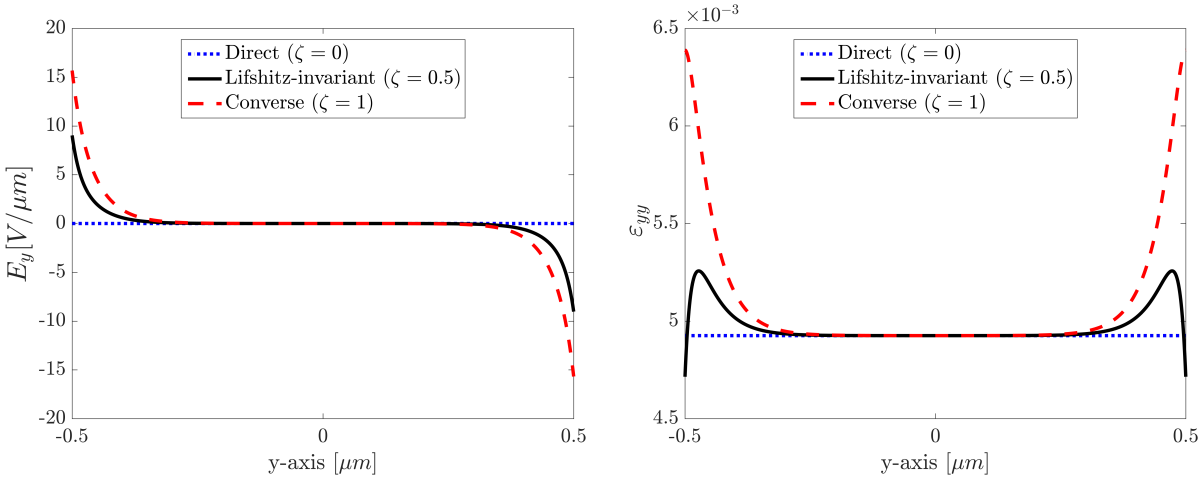

Figure 2.6: In-plane compression of a thin flexoelectric film made of BST along its length with $\bar{\varepsilon}_{xx} = -0.01$ shows surface-piezoelectric like effect. The thickness considered here is 1 μm.

Fig. 2.6, depicts E_y and ε_{yy} along the beam cross-section, Eqs. (2.29) and (2.30), respectively, for different flexoelectric models. Fig. 2.6 shows that for Lifshitz-invariant and converse models, a boundary layer develops on the transversal electric field E_y, which vanishes away from the surface. This behavior is inherently similar to direct surface piezoelectricity in non-piezoelectric materials, where a thin layer of the surface shows an electric response under mechanical deformation. Due to the generated electric field gradient near the surfaces, the strain ε_{yy} also experiences a boundary layer due to converse flexoelectricity.

2.2.1.3 Uniform bending of a microbeam

Suppose the beam is uniformly bent so that the curvature of the beam κ is the same in all cross-sections normal to it. Fig. 2.4c shows the boundary conditions and loadings for this case.

Following a slender beam approximation, the strains and electric fields can be written as:

$$\boldsymbol{\varepsilon} = \begin{bmatrix} -\kappa y & 0 \\ 0 & \varepsilon_{yy}(y) \end{bmatrix}, \qquad \boldsymbol{E} = \begin{bmatrix} 0 \\ E_y(y) \end{bmatrix}. \tag{2.37}$$

Considering homogeneous Neumann boundary conditions on the free surfaces, $E_y(y)$ and $\varepsilon_{yy}(y)$ can be obtained with the following expressions:

$$E_y(y) = \frac{-\kappa(C_L\mu_T - C_T\mu_L)}{C_L\epsilon}\left[\hat{k}_1\left[\exp\left(\frac{-y - T/2}{a_1}\right) + \exp\left(\frac{y - T/2}{a_1}\right)\right] - \hat{k}_2\left[\exp\left(\frac{-y - T/2}{a_2}\right) + \exp\left(\frac{y - T/2}{a_2}\right)\right]\right] - \frac{\kappa}{\epsilon}\left(\mu_L\frac{C_T}{C_L} - \mu_T\right), \tag{2.38}$$

$$\varepsilon_{yy}(y) = \frac{-\kappa(C_L\mu_T - C_T\mu_L)}{C_L\mu_L}\left[\hat{k}_5\left[\exp\left(\frac{-y - T/2}{a_1}\right) - \exp\left(\frac{y - T/2}{a_1}\right)\right] - \hat{k}_6\left[\exp\left(\frac{-y - T/2}{a_2}\right) - \exp\left(\frac{y - T/2}{a_2}\right)\right]\right] + \frac{C_T}{C_L}\kappa y. \tag{2.39}$$

where

$$\hat{k}_1 = \frac{\left(2a_2\hat{\gamma}_2(\zeta - 1) + \hat{\beta}_2 T\zeta\right)}{2\left(a_1\hat{\beta}_2\hat{\gamma}_1 - a_2\hat{\beta}_1\hat{\gamma}_2\right)}, \tag{2.40}$$

$$\hat{k}_2 = \frac{\left(2a_1\hat{\gamma}_1(\zeta - 1) + \hat{\beta}_1 T\zeta\right)}{2\left(a_1\hat{\beta}_2\hat{\gamma}_1 - a_2\hat{\beta}_1\hat{\gamma}_2\right)}, \tag{2.41}$$

$$\hat{k}_5 = \frac{a_1\alpha_1\left(2a_2\hat{\gamma}_2(\zeta - 1) + \hat{\beta}_2 T\zeta\right)}{2\left(a_1\hat{\beta}_2\hat{\gamma}_1 - a_2\hat{\beta}_1\hat{\gamma}_2\right)}, \tag{2.42}$$

$$\hat{k}_6 = \frac{a_2\alpha_2\left(2a_1\hat{\gamma}_1(\zeta - 1) + \hat{\beta}_1 T\zeta\right)}{2\left(a_1\hat{\beta}_2\hat{\gamma}_1 - a_2\hat{\beta}_1\hat{\gamma}_2\right)}, \tag{2.43}$$

$$\hat{\beta}_i = (1 + \exp(-T/a_i))\left(\frac{l_1^2}{l_\mu^2}\alpha_i + 1 - \zeta\right), \tag{2.44}$$

$$\hat{\gamma}_i = (1 - \exp(-T/a_i))\left(\frac{l_2^2}{a_i^2}(1 - \zeta) + \zeta\right). \tag{2.45}$$

where a_i, l_μ, and α_i have been defined in Eqs. (2.32)-(2.34). The details of the derivation of the solution have been provided in J. Note that in Eqs. (2.44), and (2.45), the thickness dependence

of $\hat{\beta}_i$ and $\hat{\gamma}_i$ vanishes if $T \gg a_i$.

Fig. 2.7, depicts E_y and ε_{yy} along the cross-section, Eqs. (2.38) and (2.39), respectively, for different flexoelectric models. It is important to note that the surface effects seen in the case of bending are mainly a combination of the surface effects in the compression case, yet with opposite signs of the applied compression on two sides of the neutral axis. That is why the results shown in Fig. 2.7 exhibit an opposite symmetry compared to Fig. 2.6. Furthermore, the coupling between $\varepsilon_{yy,y}$ and E_y through μ_L causes an additional surface effect. That is why a small surface effect can be seen with the direct model in the case of bending.

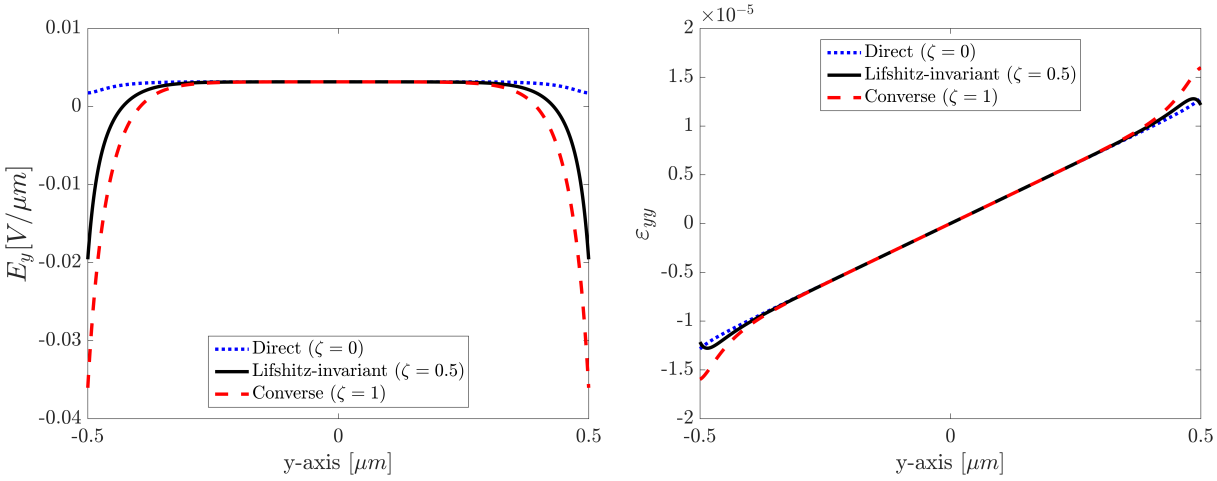

Figure 2.7: Surface effects of a flexoelectric thin film made of BST under uniform bending with $\kappa = 50[1/m]$. The thickness considered here is 1 μm.

2.2.2 Discussion

Three forms of coupling are mainly considered in the flexoelectric literature. Direct flexoelectricity is modeled as $-\mu_{lijk}\epsilon_{ij,k}E_l$, converse flexoelectricity is modeled as $\mu_{lijk}\epsilon_{ij}E_{l,k}$, and Lifshitz-invariant flexoelectricity is modeled as $\frac{1}{2}\mu_{lijk}\epsilon_{ij}E_{l,k} - \frac{1}{2}\mu_{lijk}\epsilon_{ij,k}E_l$. As shown in Section 2.1.2, considering any of the mentioned coupling terms explicitely in the electromechanical enthalpy would not change the governing equations, yet the definition of Neumann boundary conditions is different in the three flexoelectric models. This results in solving different boundary value problems if the Neumann boundary condition is imposed anywhere on the boundaries. Table 2.2 summarizes the components of the strain and electric field that exhibit boundary layers for the different case studies and different flexoelectric models. Electrical actuation and compression cases are of particular importance as the electromechanical response is isolated from the bulk flexoelectric response. As explained in Section 2.2.1.1, a homogeneous electric field can cause a shear strain gradient due to inverse flexoelectricity. This means that the surface of the body exhibits a mechanical response due to the application of an external

Table 2.2: The components of the strain or electric field that exhibit boundary layers for different cases and different flexoelectric models

Case	Direct ($\zeta = 0$)	Lifshitz-invariant ($\zeta = 0.5$)	Converse ($\zeta = 1$)
Electric actuation	ε_{xy}	ε_{xy}	-
Compression	-	ε_{yy}, E_y	ε_{yy}, E_y
Bending	ε_{yy}, E_y	ε_{yy}, E_y	ε_{yy}, E_y

electrical stimulus, or inverse surface piezoelectricity. Besides, as shown in Section 2.2.1.2, a homogeneous strain can cause an electric field gradient due to inverse converse flexoelectricity, a behavior that is similar to direct surface piezoelectricity. Considering either the direct or the converse flexoelectric models result in a one-way surface piezoelectric-like effect (direct or inverse), while the Lifshitz-invariant model shows a two-way surface piezoelectric-like effect (direct and inverse). The inherent surface effects of flexoelectricity with different models have already been seen in different studies (Abdollahi *et al.*, 2014, Codony *et al.*, 2021, Yurkov and Tagantsev, 2016, Zhuang *et al.*, 2020b). In particular, (Codony *et al.*, 2021) studied a cantilever beam under bending and showed that the Lifshitz-invariant model exhibits a boundary layer on E_y. This is in agreement with the results of this paper. However, as in (Codony *et al.*, 2021) the longitudinal flexoelectric coefficient μ_L was neglected, no boundary layer in E_y was observed in the direct model. The boundary layers have also been seen in a cantilever beam actuator (Abdollahi *et al.*, 2014, Codony *et al.*, 2021, He *et al.*, 2019, Zhuang *et al.*, 2020b). One could perform a similar exercise as Section 2.2.1.1 by changing the boundary conditions (applying Dirichlet electric boundary conditions instead of homogeneous Neumann electric boundary conditions on free surfaces), and explaining the boundary layers seen in the vertical electric field of the cantilever beam actuator. However, as our aim was to shed light on the origins of the surface effects in the flexoelectricity models and not explain every single example, we did not provide more examples.

2.2.3 Concluding remarks

In this section, we explored the continuum models of flexoelectricity in dielectrics. We showed that when the size of the body is finite, the continuum models of flexoelectricity in bulk exhibit surface piezoelectric-like effects. We attributed the surface effects to be due to inverse flexoelectricity and inverse converse flexoelectricity. Comparing different flexoelectric couplings, we showed that the direct and converse flexoelectric models exhibit a one-way surface piezoelectric-like effect, while the Lifshitz-invariant model shows a two-way surface piezoelectric-like effect. Furthermore, we characterized the observed boundary layers in terms of the length scales of the model. Future research can be carried out to explore the interaction of the inherent surface effects of flexoelectricity with other physics (bulk piezoelectricity, surface piezoelectricity, and surface flexoelectricity). Besides, how to model flexoelectricity is

still an open question (there is no clear physical understanding that which ζ parameter can well describe reality). There are also no clear insights into the high-order boundary conditions for which homogeneous Neumann conditions are commonly imposed in the literature for convenience. Furthermore, characterization of the physical length scales of the model still needs to be further researched. By comparing with other approaches (atomistic simulations or experiments), the results provided here may be useful to find some of the parameters that are not yet well understood.

2.3 Variational formulation for flexoelectric solids at finite deformation

After exploring the continuum models of flexoelectricity in infinitesimal strains, in this section, we aim to extend the continuum models of flexoelectricity for finite deformation. We extend the formulation presented in (Codony *et al.*, 2020) to a Lifshitz-invariant flexoelectric model accounting for material incompressibility and material interfaces.

2.3.1 Preliminaries

Consider a deformable continuum dielectric body denoted by Ω_0 in the undeformed configuration, and by Ω in the deformed configuration. The deformation map $\boldsymbol{\chi} : \Omega_0 \longrightarrow \Omega$ carries every material point $\boldsymbol{X} \in \Omega_0$ to a spatial point $\boldsymbol{x} = \boldsymbol{\chi}(\boldsymbol{X}) \in \Omega$. Let $F_{iI}(\boldsymbol{X}) = \partial\chi_i(\boldsymbol{X})/\partial X_I$ be the deformation gradient, $J := \det(\mathbf{F})$ be the Jacobian, $C_{IJ} := F_{kI}F_{kJ}$ be the right Cauchy-Green tensor and $\mathfrak{E}_{IJ} := \frac{1}{2}\left(C_{IJ} - \delta_{IJ}\right)$ be the Green-Lagrange strain tensor, with δ_{IJ} the Kronecker delta. The theory of flexoelectricity involves higher order derivatives of deformation. We introduce the gradients of the deformation gradient, the right Cauchy-Green tensor and the Green-Lagrange strain tensor as

$$\widetilde{F}_{iJK} := \frac{\partial F_{iJ}}{\partial X_K} = \frac{\partial^2 \chi_i}{\partial X_J \partial X_K}, \quad \widetilde{C}_{IJK} := \frac{\partial C_{IJ}}{\partial X_K} = 2\,\underset{IJ}{\text{symm}}\left(\widetilde{F}_{kIK}F_{kJ}\right), \quad \widetilde{\mathfrak{E}}_{IJK} := \frac{\partial \mathfrak{E}_{IJ}}{\partial X_K} = \frac{1}{2}\widetilde{C}_{IJK}, \tag{2.46}$$

where $\text{symm}_{IJ}\left(A_{IJ}\right) := \left(A_{IJ} + A_{JI}\right)/2$.
The electric potential in the material frame is denoted by $\Phi(\boldsymbol{X})$. Then, the nominal electric field $\boldsymbol{E}$ and its first gradient $\tilde{\boldsymbol{E}}$ are defined as

$$E_I := -\frac{\partial \Phi}{\partial X_I}, \qquad \tilde{E}_{IJ} := \frac{\partial E_I}{\partial X_J} = -\frac{\partial^2 \Phi}{\partial X_I \partial X_J}. \tag{2.47}$$

2.3.2 Variational formulation in material form

Largely following (Codony *et al.*, 2020), the total electromechanical enthalpy density of a flexoelectric solid in the absence of piezoelectricity consists of five contributions namely the

elastic Ψ^{Elast}, the strain gradient elastic Ψ^{SGEla}, the flexoelectric Ψ^{Flexo}, the dielectric Ψ^{Diele} and the gradient dielectric Ψ^{GDiele} energy densities:

$$\Psi^{\text{Enth}}(\mathfrak{E}, \widetilde{\mathfrak{E}}, \boldsymbol{E}, \tilde{\boldsymbol{E}}) = \Psi^{\text{Elast}}(\mathfrak{E}) + \Psi^{\text{SGEla}}(\widetilde{\mathfrak{E}}) + \Psi^{\text{Flexo}}(\mathfrak{E}, \widetilde{\mathfrak{E}}, \boldsymbol{E}, \tilde{\boldsymbol{E}}) + \Psi^{\text{Diele}}(\mathfrak{E}, \boldsymbol{E}) + \Psi^{\text{GDiele}}(\tilde{\boldsymbol{E}}). \tag{2.48}$$

For the elastic contribution, a conventional Neo-Hookean model is chosen to model the shear elasticity of the incompressible solid,

$$\Psi^{\text{Elast}}(\mathfrak{E}) = \frac{1}{2} G\,(\operatorname{tr} \mathbf{C} - 2) - G \ln(J), \tag{2.49}$$

where G is the shear modulus. The strain gradient elastic contribution is written as

$$\Psi^{\text{SGEla}}(\widetilde{\mathfrak{E}}) = \frac{1}{2} \widetilde{\mathfrak{E}}_{IJK} h_{IJKLMN} \widetilde{\mathfrak{E}}_{LMN}, \tag{2.50}$$

where $\mathbf{h}$ is a sixth-order strain gradient elasticity tensor given by Eq. (B.1) in terms of an elastic material length scale ℓ_1.

In contrast to (Codony *et al.*, 2020), we consider here a symmetric form for the flexoelectric energy density taking into account contributions of both direct and converse flexoelectricity (Codony *et al.*, 2021, Sharma *et al.*, 2010, Zhuang *et al.*, 2020b) given by

$$\Psi^{\text{Flexo}}(\mathfrak{E}, \widetilde{\mathfrak{E}}, \boldsymbol{E}, \tilde{\boldsymbol{E}}) = -\frac{1}{2} J C^{-1}_{AB} \mu_{AIJK} E_B \widetilde{\mathfrak{E}}_{IJK} + \frac{1}{2} J C^{-1}_{AB} \mu_{AIJK} \tilde{E}_{BK} \mathfrak{E}_{IJ}, \tag{2.51}$$

where $\boldsymbol{\mu}$ is the flexoelectricity tensor described in Eq. (B.2). The dielectric energy density is

$$\Psi^{\text{Diele}}(\mathfrak{E}, \boldsymbol{E}) = -\frac{1}{2} J \epsilon E_K C^{-1}_{KL} E_L, \tag{2.52}$$

where ϵ is the electric permittivity of the material. The gradient dielectric energy density contribution can be defined as (Zhuang *et al.*, 2020b)

$$\Psi^{\text{GDiele}}(\tilde{\boldsymbol{E}}) = -\frac{1}{2} \tilde{E}_{IJ} M_{IJKL} \tilde{E}_{KL}, \tag{2.53}$$

where $\boldsymbol{M}$ is the fourth-order gradient dielectricity tensor defined in Eq. (B.4) in terms of a dielectric material length scale ℓ_2. Similarly to the linear case, see Eq. A.6, a third material length scale arises, the flexoelectric length scale as defined in Eq. B.3.

We note that one can formulate the theory in terms of a Lagrangian internal energy density that, instead of $\boldsymbol{E}$ and $\tilde{\boldsymbol{E}}$, depends on Lagrangian polarization $\boldsymbol{P}$ and its gradient $\tilde{\boldsymbol{P}}$. In Appendix F, we assess the relation of such model with that considered in the present study.

The boundary of the body in the undeformed configuration, $\partial\Omega_0$, is split into several

disjoint Dirichlet and Neumann sets as follows:

$$\partial\Omega_0 = \partial\Omega_0^{\chi} \cup \partial\Omega_0^{T} = \partial\Omega_0^{V} \cup \partial\Omega_0^{R} = \partial\Omega_0^{\Phi} \cup \partial\Omega_0^{W} = \partial\Omega_0^{M} \cup \partial\Omega_0^{O}. \tag{2.54}$$

On the Dirichlet boundaries $\partial\Omega_0^{\chi}$, $\partial\Omega_0^{V}$, $\partial\Omega_0^{\Phi}$ and $\partial\Omega_0^{M}$, the deformation map $\boldsymbol{\chi}$, normal derivatives of the deformation map $\partial^N\chi$, the electric potential Φ, and the normal derivative of the electric potential $\partial^N\Phi$ are prescribed. On the Neumann boundaries $\partial\Omega_0^{T}$, $\partial\Omega_0^{R}$, $\partial\Omega_0^{W}$ and $\partial\Omega_0^{O}$ their associated work conjugate quantities (per unit undeformed area) are prescribed. The Neumann boundary data consists of the surface traction $\overline{\boldsymbol{T}}$, the surface double traction $\overline{\boldsymbol{R}}$, the surface charge density $\overline{W}$ and the surface double charge $\overline{O}$. Because of the strain gradient elasticity and the gradient dielectricity terms in the electromechanical enthalpy, additional boundary conditions emerge on the non-smooth regions of $\partial\Omega_0$, i.e. edges (corners) C_0 in a 3D (2D) domain. We also split them into Dirichlet and Neumann sets as follows:

$$C_0 = C_0^{\chi} \cup C_0^{J} = C_0^{\Phi} \cup C_0^{K}. \tag{2.55}$$

On the Dirichlet sets C_0^{χ} and C_0^{Φ}, the deformation map $\boldsymbol{\chi}$ and the electric potential Φ are prescribed, while on the Neumann sets C_0^{J} and C_0^{K}, the edge force per unit length in 3D (or corner force in 2D) $\overline{\boldsymbol{J}}$ and the charge density per unit length in 3D (or charge in 2D) $\overline{K}$ are prescribed. We consider dead loads for simplicity.

The total electromechanical enthalpy of an incompressible flexoelectric material in 3D can be written as

$$\begin{aligned}\Pi[\boldsymbol{\chi},\Phi,p] = &\int_{\Omega_0} \left[\Psi^{\text{Enth}}(\mathfrak{E},\widetilde{\mathfrak{E}},\boldsymbol{E},\tilde{\boldsymbol{E}}) + p(J-1) - B_i\chi_i + Q\Phi\right] \mathrm{d}\Omega_0 \\ &- \int_{\partial\Omega_0^{T}} \overline{T}_i\chi_i \,\mathrm{d}\Gamma_0 - \int_{\partial\Omega_0^{R}} \overline{R}_i\partial^N\chi_i \,\mathrm{d}\Gamma_0 - \int_{C_0^{J}} \overline{J}_i\chi_i \,\mathrm{d}s_0 \\ &+ \int_{\partial\Omega_0^{W}} \overline{W}\Phi \,\mathrm{d}\Gamma_0 + \int_{\partial\Omega_0^{O}} \overline{O}\partial^N\Phi \,\mathrm{d}\Gamma_0 + \int_{C_0^{K}} \overline{K}\Phi \,\mathrm{d}s_0,\end{aligned} \tag{2.56}$$

where the pressure field p is the Lagrange multiplier imposing point-wise the incompressibility constraint $J = 1$, and B and Q are body force and and electric charge per unit undeformed volume. In 2D, $d\Omega_0$ is an area element, $d\Gamma_0$ a line element, and $\mathrm{d}s_0$ just denotes evaluation of the integrand at corner points.

In equilibrium, the first variation of $\Pi[\boldsymbol{\chi},\Phi,p]$ must vanish yielding

$$\begin{aligned}0 =&\delta\Pi[\boldsymbol{\chi},\Phi,p;\delta\boldsymbol{\chi},\delta\Phi,\delta p] \\ =&\int_{\Omega_0} \left(\frac{\partial\Psi^{\text{Enth}}}{\partial\mathfrak{E}_{IJ}}\delta\mathfrak{E}_{IJ} + \frac{\partial\Psi^{\text{Enth}}}{\partial\widetilde{\mathfrak{E}}_{IJK}}\delta\widetilde{\mathfrak{E}}_{IJK} + \frac{\partial\Psi^{\text{Enth}}}{\partial E_L}\delta E_L + \frac{\partial\Psi^{\text{Enth}}}{\partial\tilde{E}_{LM}}\delta\tilde{E}_{LM} + (J-1)\delta p - B_i\delta\chi_i + Q\delta\Phi \right) \mathrm{d}\Omega_0 \\ &- \int_{\partial\Omega_0^{T}} \overline{T}_i\delta\chi_i \,\mathrm{d}\Gamma_0 - \int_{\partial\Omega_0^{R}} \overline{R}_i\partial^N\delta\chi_i \,\mathrm{d}\Gamma_0 - \int_{C_0^{J}} \overline{J}_i\delta\chi_i \,\mathrm{d}s_0\end{aligned}$$

$$
\begin{aligned}
&+ \int_{\partial\Omega_0^W} \overline{W}\delta\Phi \,\mathrm{d}\Gamma_0 + \int_{\partial\Omega_0^O} \overline{O}\partial^N\delta\Phi \,\mathrm{d}\Gamma_0 + \int_{C_0^K} \overline{K}\delta\Phi \,\mathrm{d}s_0 \\
&= \int_{\Omega_0} \left(\hat{S}_{IJ}\delta\mathfrak{E}_{IJ} + \tilde{S}_{IJK}\delta\widetilde{\mathfrak{E}}_{IJK} - \hat{D}_L\delta E_L - \widetilde{D}_{LM}\delta\tilde{E}_{LM} + (J-1)\delta p - B_i\delta\chi_i + Q\delta\Phi \right) \mathrm{d}\Omega_0 \\
&\quad - \int_{\partial\Omega_0^T} \overline{T}_i\delta\chi_i \,\mathrm{d}\Gamma_0 - \int_{\partial\Omega_0^R} \overline{R}_i\partial^N\delta\chi_i \,\mathrm{d}\Gamma_0 - \int_{C_0^J} \overline{J}_i\delta\chi_i \,\mathrm{d}s_0 \\
&\quad + \int_{\partial\Omega_0^W} \overline{W}\delta\Phi \,\mathrm{d}\Gamma_0 + \int_{\partial\Omega_0^O} \overline{O}\partial^N\delta\Phi \,\mathrm{d}\Gamma_0 + \int_{C_0^K} \overline{K}\delta\Phi \,\mathrm{d}s_0,
\end{aligned} \tag{2.57}
$$

for all admissible variations $\delta\boldsymbol{\chi}$, $\delta\Phi$ and δp consistent with the Dirichlet boundary conditions, where

$$
\delta E_L := -\frac{\partial(\delta\Phi)}{\partial X_L}, \qquad \delta\tilde{E}_{LM} := -\frac{\partial^2(\delta\Phi)}{\partial X_L\partial X_M}, \qquad \delta F_{iI} := \frac{\partial(\delta\chi_i)}{\partial X_I}, \qquad \delta\tilde{F}_{iIJ} := \frac{\partial^2(\delta\chi_i)}{\partial X_I\partial X_J}, \tag{2.58}
$$

$$
\delta\mathfrak{E}_{IJ} = \frac{1}{2}\delta C_{IJ} := \underset{IJ}{\operatorname{symm}} \left(\delta F_{kI}F_{kJ} \right), \qquad \delta\widetilde{\mathfrak{E}}_{IJK} = \frac{1}{2}\delta\widetilde{C}_{IJK} := \underset{IJ}{\operatorname{symm}} \left(\delta F_{kI}\tilde{F}_{kJK} + F_{kI}\delta\tilde{F}_{kJK} \right). \tag{2.59}
$$

The local second Piola-Kirchhoff stress $\hat{S}$, the second Piola-Kirchhoff double stress $\tilde{S}$, the electric displacement $\hat{D}$ and the double electric displacement $\widetilde{D}$ are given by

$$
\begin{aligned}
\hat{S}_{IJ} &= G\left(\delta_{IJ} - C_{IJ}^{-1}\right) + pC_{IJ}^{-1} + \frac{1}{2}\mathscr{C}_{MLIJ}\left(\epsilon E_L E_M + \mu_{LABK}E_M\widetilde{\mathfrak{E}}_{ABK} - \mu_{LABK}\tilde{E}_{MK}\mathfrak{E}_{AB}\right) \\
&\quad + \frac{1}{2}C_{AB}^{-1}\mu_{AIJK}\tilde{E}_{BK},
\end{aligned} \tag{2.60}
$$

$$
\tilde{S}_{IJK} = h_{IJKLMN}\widetilde{\mathfrak{E}}_{LMN} - \frac{1}{2}C_{LM}^{-1}E_M\mu_{LIJK}, \tag{2.61}
$$

$$
\hat{D}_L = C_{KL}^{-1}\left(\epsilon E_K + \frac{1}{2}\mu_{KIJM}\widetilde{\mathfrak{E}}_{IJM}\right), \tag{2.62}
$$

$$
\widetilde{D}_{LM} = -\frac{1}{2}C_{AL}^{-1}\mu_{AIJM}\mathfrak{E}_{IJ} + \tilde{E}_{IJ}M_{IJLM}, \tag{2.63}
$$

where $\mathscr{C}_{ABCD} = \left(C_{AC}^{-1}C_{BD}^{-1} + C_{BC}^{-1}C_{AD}^{-1} - C_{AB}^{-1}C_{CD}^{-1}\right)$. These equations clearly highlight the electromechanical couplings, the influence of each material tensor, and the strong nonlinearity introduced by large deformations.

Equation (2.57) can be integrated by parts and by invoking the divergence, surface divergence and Stokes's theorems (for more details on the derivation see Appendix C), to obtain the strong form of the governing equations:

$$
\begin{cases}
(F_{iI}S_{IJ})_{,J} + B_i = 0 \quad \text{in } \Omega_0, \\
D_{L,L} - Q = 0 \quad \text{in } \Omega_0,
\end{cases} \tag{2.64}
$$

where the physical second Piola-Kirchhoff stress $\boldsymbol{S}$ and physical electric displacement $\boldsymbol{D}$ can be defined as

$$S_{IJ} = \hat{S}_{IJ} - \tilde{S}_{IJK,K}, \tag{2.65}$$
$$D_L = \widehat{D}_L - \widetilde{D}_{LM,M}. \tag{2.66}$$

This procedure also identifies the definitions of the surface traction $\boldsymbol{T}$, the surface double traction $\boldsymbol{R}$, the surface charge density W, the surface double charge density O, the edge forces $\boldsymbol{J}$ and the edge charge K as

$$T_i = \left[F_{iI}\hat{S}_{IJ} + \tilde{F}_{iIK}\tilde{S}_{IJK} - \left(F_{iI}\tilde{S}_{IJK}\right)_{,K} - \left(F_{iI}\tilde{S}_{IKJ}\right)_{,L}\mathbb{P}_{KL}\right]N_J + F_{iI}\tilde{S}_{IJK}\widetilde{N}_{JK}, \tag{2.67}$$
$$R_i = F_{iI}\tilde{S}_{IJK}N_JN_K, \tag{2.68}$$
$$J_i = [\![F_{iI}\tilde{S}_{IJK}\mathfrak{M}_JN_K]\!], \tag{2.69}$$
$$W = \left[-\widehat{D}_L + \widetilde{D}_{LM,M} + \left(\widetilde{D}_{ML}\right)_{,K}\mathbb{P}_{KM}\right]N_L - \widetilde{D}_{LM}\widetilde{N}_{LM}, \tag{2.70}$$
$$O = -\widetilde{D}_{LM}N_LN_M, \tag{2.71}$$
$$K = -[\![\widetilde{D}_{LM}\mathfrak{M}_LN_M]\!], \tag{2.72}$$

where $\boldsymbol{N}$ is the outward unit normal vector on $\partial\Omega_0$, $\mathfrak{M}$ is the outward unit co-normal vector on C_0, $\mathbb{P} = \mathbf{I} - \boldsymbol{N}\otimes\boldsymbol{N}$ is the projection operator on $\partial\Omega_0$, $\widetilde{\mathbf{N}} = (\nabla_0\boldsymbol{N} : \mathbb{P})\,\boldsymbol{N}\times\boldsymbol{N} - \nabla_0\boldsymbol{N}\cdot\mathbb{P}$, or in components, $\widetilde{N}_{IJ} = (\partial N_K/\partial X_L\,\mathbb{P}_{KL})N_IN_J - \partial N_I/\partial X_K\,\mathbb{P}_{KJ}$ is the second-order geometry tensor on $\partial\Omega_0$ and $[\![\ ]\!]$ is the jump operator defined on C as the signed sum of its argument evaluated at each boundary adjacent to C. A detailed derivation of the mentioned geometrical quantities can be found in (Codony *et al.*, 2019).

2.3.3 Variational formulation in material form including an internal material interface

Nitsche's method formulation for weak enforcement of interface conditions has been derived for infinitesimal strains (Barceló-Mercader *et al.*, 2022). In this section, the mentioned formulation has been extended for large deformations. Weak enforcement of the interface conditions can give us the flexibility to enforce the required continuities on the interfaces of arbitrary geometry (Wang *et al.*, 2015). Besides, weak enforcement enables us to deal with imposing the continuity conditions for non-conforming meshes. However, these are the future work and thus are out of the scope of this thesis.

Consider a physical domain in the undeformed configuration denoted by Ω_0 composed of two non-overlapping sub-domains as $\Omega_0 = \Omega_0^{(1)} \cup \Omega_0^{(2)}$. Each sub-domain has a boundary $\partial\Omega_0^{(i)}$. The material interface is defined as $\mathcal{I}_0 = \partial\Omega_0^{(1)} \cap \partial\Omega_0^{(2)}$. We define the weighted mean operator

and jump operator for a function A that can be discontinuous across $\mathcal{I}_0$ as

$$\{A\}_\gamma = \gamma A^1 + (1-\gamma)A^2 \quad \text{on} \quad \mathcal{I}_0, \tag{2.73}$$

$$[\![A]\!] = A^1 + A^2 \quad \text{on} \quad \mathcal{I}_0, \tag{2.74}$$

where $\gamma \in (0,1)$ and A^i denotes the value of A from sub-domain $\Omega_0^{(i)}$.

The energy potential of Nitsche's method associated with the interface can be written as

$$\begin{aligned}
\Pi^{\text{Interface}}[\chi,\Phi,p] = &\int_{I_0}\left[\frac{1}{2}\beta^{\chi_I}[\![\chi_i N_J]\!]^2 - [\![\chi_i N_J]\!]\left\{T_i N_J\right\}_\gamma\right]\mathrm{d}\Gamma_0 \\
&+\int_{I_0}\left[\frac{1}{2}\beta^{\partial^N\chi_I}\left[\!\left[\partial^N\chi_i\right]\!\right]^2 - \left[\!\left[\partial^N\chi_i\right]\!\right]\left\{R_i\right\}_\gamma\right]\mathrm{d}\Gamma_0 \\
&+\int_{I_0}\left[-\frac{1}{2}\beta^{\Phi_I}\left[\!\left[\Phi N_I\right]\!\right]^2 + \left[\!\left[\Phi N_I\right]\!\right]\left\{WN_I\right\}_\gamma\right]\mathrm{d}\Gamma_0 \\
&+\int_{I_0}\left[-\frac{1}{2}\beta^{\partial^N\Phi_I}\left[\!\left[\partial^N\Phi\right]\!\right]^2 + \left[\!\left[\partial^N\Phi\right]\!\right]\left\{O\right\}_\gamma\right]\mathrm{d}\Gamma_0 \\
&+\sum_{k=1}^{H}\int_{C_0^k}\left[\frac{1}{2}\beta^{\chi_c}(\chi_i^1-\chi_i^2)^2 - (\chi_i^1-\chi_i^2)(J_i^1-J_i^2)\right]\mathrm{d}s_0 \\
&+\sum_{k=1}^{H}\int_{C_0^k}\left[-\frac{1}{2}\beta^{\Phi_c}(\Phi^1-\Phi^2)^2 + (\Phi^1-\Phi^2)(K^1-K^2)\right]\mathrm{d}s_0,
\end{aligned} \tag{2.75}$$

where H is the numbers of edges (corners) in a 3D (2D) domain on the interface, β^{χ_I}, $\beta^{\partial^N\chi_I}$, β^{Φ_I}, $\beta^{\partial^N\Phi_I}$, β^{χ_c} and β^{Φ_c} are penalty parameters of Nitsche's method to ensure energy being concave up with respect to the deformation χ and concave down with respect to electric potential Φ. The penalty parameters should be large enough but in practice do not need to be too large, which would cause ill-conditioning. Note that at the solution, the penalty terms vanish and we recover the physical work at the interface, and hence the method is variationally consistent. This method can be trivially applied to enforce Dirichlet boundary conditions at the domain boundary, see (Codony *et al.*, 2019) for the derivation in the infinite deformation setting.

Enforcing Dirichlet boundary conditions strongly, the total energy of the domain Ω_0 including Nitsche's functional to deal with internal interfaces is then

$$\Pi^{\text{Bimaterial}}[\chi,\Phi,p] = \Pi[\chi,\Phi,p] + \Pi^{\text{Interface}}[\chi,\Phi,p]. \tag{2.76}$$

The necessary condition for electromechanical equilibrium is that the first variation of $\Pi^{\text{Bimaterial}}$ vanishes, yielding

$$\delta\Pi^{\text{Bimaterial}}[\boldsymbol{\chi},\Phi,p;\delta\boldsymbol{\chi},\delta\Phi,\delta p] = \delta\Pi[\boldsymbol{\chi},\Phi,p;\delta\boldsymbol{\chi},\delta\Phi,\delta p] + \delta\Pi^{\text{Interface}}[\boldsymbol{\chi},\Phi,p;\delta\boldsymbol{\chi},\delta\Phi,\delta p] = 0,$$

(2.77)

for all admissible variations $\delta\boldsymbol{\chi}$, $\delta\Phi$, δp consistent with the Dirichlet boundary conditions. The variation $\delta\Pi$ has been derived in Eq. (2.57) and $\delta\Pi^{\text{Interface}}$ can be written as

$$
\begin{aligned}
\delta\Pi^{\text{Interface}}[\boldsymbol{\chi},\Phi,p;\delta\boldsymbol{\chi},\delta\Phi,\delta p] = &\int_I \left[\beta^{\chi_I}\left[\!\left[\delta\chi_i N_J\right]\!\right]\left[\!\left[\chi_i N_J\right]\!\right] - \left[\!\left[\delta\chi_i N_J\right]\!\right]\left\{T_i N_J\right\}_\gamma - \left[\!\left[\chi_i N_J\right]\!\right]\left\{\delta T_i N_J\right\}_\gamma\right] \mathrm{d}\Gamma \\
&+ \int_I \left[\beta^{\partial^N\chi_I}\left[\!\left[\partial^N\delta\chi_i\right]\!\right]\left[\!\left[\partial^N\chi_i\right]\!\right] - \left[\!\left[\partial^N\delta\chi_i\right]\!\right]\left\{R_i\right\}_\gamma - \left[\!\left[\partial^N\chi_i\right]\!\right]\left\{\delta R_i\right\}_\gamma\right] \mathrm{d}\Gamma \\
&+ \int_I \left[-\beta^{\Phi_I}\left[\!\left[\delta\Phi N_I\right]\!\right]\left[\!\left[\Phi N_I\right]\!\right] + \left[\!\left[\delta\Phi N_I\right]\!\right]\left\{W N_I\right\}_\gamma + \left[\!\left[\Phi N_I\right]\!\right]\left\{\delta W N_I\right\}_\gamma\right] \mathrm{d}\Gamma \\
&+ \int_I \left[-\beta^{\partial^N\Phi_I}\left[\!\left[\partial^N\delta\Phi\right]\!\right]\left[\!\left[\partial^N\Phi\right]\!\right] - \left[\!\left[\partial^N\delta\Phi\right]\!\right]\left\{O\right\}_\gamma + \left[\!\left[\partial^N\Phi\right]\!\right]\left\{\delta O\right\}_\gamma\right] \mathrm{d}\Gamma \\
&+ \sum_{k=1}^{H}\int_{C^k}\left[\beta^{\chi_c}(\chi_i^1-\chi_i^2)(\delta\chi_i^1-\delta\chi_i^2) - (\delta\chi_i^1-\delta\chi_i^2)(J_i^1-J_i^2) - (\chi_i^1-\chi_i^2)(\delta J_i^1-\delta J_i^2)\right] \mathrm{d}s \\
&+ \sum_{k=1}^{H}\int_{C^k}\left[-\beta^{\Phi_c}(\Phi^1-\Phi^2)(\delta\Phi^1-\delta\Phi^2) + (\delta\Phi^1-\delta\Phi^2)(K^1-K^2) + (\Phi^1-\Phi^2)(\delta K^1-\delta K^2)\right] \mathrm{d}s,
\end{aligned}
\tag{2.78}
$$

where the variations of the Neumann terms δT_i, δR_i, δJ_i, δW, δO and δK expressed in terms of $\delta\boldsymbol{\chi}$, $\delta\Phi$, δp can be found in Appendix D.

2.4 Numerical approximation

C^1continuty of the basis functions is required to approximate fourth-order PDEs. B-splines are piecewise polynomial functions that meet the high-order continuity requirement. In this section, we brifely discuss about B-splines and their two-scale refinement property which is used in subdivision-stabilization technique to satisfy the numerical inf-sup condition (Dortdivanlioglu *et al.*, 2018, Dortdivanlioglu and Linder, 2019, Kadapa *et al.*, 2016, Rüberg and Cirak, 2012). We then introduce the numerical approximation used in this paper. Consider a uniform knot vector $\Xi = \{\xi_1, \xi_2, ..., \xi_{n+p+1}\}$ formed by a set of $n + p + 1$ non-decreasing evenly-spaced real numbers ξ_i called knots, where p is the polynomial order and n is the number of control points and basis functions used to form the B-spline curve. Each knot ξ_i is a coordinate in the parameter space and they partition the parameter space into elements, also known as knot spans. Using the knot vector Ξ, the uniform B-spline basis functions can be recursively

constructed for piecewise constants ($p = 0$) using

$$N_i^0(\xi) = \begin{cases} 1 & \xi_i \leq \xi < \xi_{i+1} \\ 0 & \text{otherwise.} \end{cases} \tag{2.79}$$

and for $p > 0$ using

$$N_i^p(\xi) = \frac{\xi - \xi_i}{\xi_{i+p} - \xi_i} N_i^{p-1}(\xi) + \frac{\xi_{i+p+1} - \xi}{\xi_{i+p+1} - \xi_{i+1}} N_{i+1}^{p-1}(\xi). \tag{2.80}$$

Note that each basis function $N_i^p(\xi)$ constructs a partition of unity, i.e., $\sum_{i=1}^{n} N_i^p(\xi) = 1$, and it is positive over a knot interval $\xi_i \leq \xi < \xi_{i+1}$. By taking a linear combination of the basis functions $N_i^p(\xi)$, a B-spline curve of the order p in $\mathbb{R}^d$ can be formed as

$$\mathbf{C}(\xi) = \sum_{i=1}^{n} N_i^p(\xi) B_i, \tag{2.81}$$

$\mathbf{B}$ being the set of n control points with $B_i \in \mathbb{R}^d$. Being analogous to the nodal coordinates in the standard finite element method, the control points have a distinctive feature that they are not interpolated by the B-spline basis functions when $p \geq 2$. Using open knot vectors, B-spline curves can be constructed which are interpolated at the ends. Open knot vectors can be constructed by increasing the multiplicity of the initial and the final knot values to $p + 1$, i.e. $\xi_1 = \xi_2 = ... = \xi_{p+1}$ and $\xi_{n+1} = \xi_{n+2} = ... = \xi_{n+p+1}$. A p^{th} order B-spline constructed by a uniform open knot vector shows C^{p-1} continuity over the whole domain except at the ends where C^{-1} continuity exists.

One of the remarkable features of the B-splines is their refinability, also referred to as the two-scale relation. Consider a non-decreasing uniform knot vector $\Xi = \{\xi_1, \xi_2, \xi_3, ...\} = \{0, 1, 2, ...\}$ forming basis functions $\boldsymbol{N}^p$. Finer basis functions $\tilde{\boldsymbol{N}}^p$ can be formed by using a new knot vector $\tilde{\Xi} = \{\tilde{\xi}_1, \tilde{\xi}_2, \tilde{\xi}_3, ...\} = \{0, 1/2, 1, ...\}$ constructed by bisecting the knot intervals in Ξ. It can be shown that the coarse basis functions $\boldsymbol{N}^p$ and the fine basis functions $\tilde{\boldsymbol{N}}^p$ have the following relation

$$\tilde{N}_i^p(\xi) = N_1^p(2\xi - i). \tag{2.82}$$

From Eq. 2.82, it can be noted the support size of the coarse basis functions $\boldsymbol{N}^p$ is twice that of the fine basis functions $\tilde{\boldsymbol{N}}^p$. More imporantly, each coarse basis function N_i^p can be expressed as a linear combination of $p+2$ fine basis functions $\tilde{N}_k^p$ as shown in Fig. 2.8, using the two-scale relation as

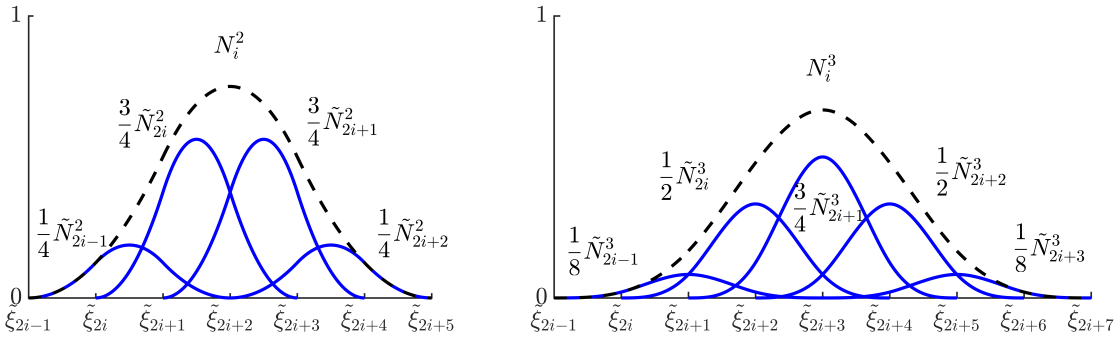

(a) Quadratic basis functions ($p = 2$) (b) Cubic basis functions ($p = 3$)

Figure 2.8: Two-scale relation for quadratic and cubic B-splines. The coarse basis functions are constructed by a linear combination of $p + 2$ fine basis functions. For $p = 2$ the coarse basis function is formed as $N_i^2 = \frac{1}{4}\tilde{N}_{2i-1}^2 + \frac{3}{4}\tilde{N}_{2i}^2 + \frac{3}{4}\tilde{N}_{2i+1}^2 + \frac{1}{4}\tilde{N}_{2i+2}^2$, and for $p = 3$ the coarse basis function is obtained as $N_i^3 = \frac{1}{8}\tilde{N}_{2i-1}^3 + \frac{1}{2}\tilde{N}_{2i}^3 + \frac{3}{4}\tilde{N}_{2i+1}^3 + \frac{1}{2}\tilde{N}_{2i+2}^3 + \frac{1}{8}\tilde{N}_{2i+3}^3$.

$$N_i^p(\xi) = \frac{1}{2^p}\sum_{k=0}^{p+1}\binom{p+1}{k}\tilde{N}_{2i+k-1}^p(\xi) \qquad \text{or in matrix notation} \qquad \boldsymbol{N}^p(\xi) = \boldsymbol{S}\tilde{\boldsymbol{N}}^p(\xi), \tag{2.83}$$

where $\boldsymbol{S}$ is known as the subdivision matrix formed by the elements $S_k^p = \frac{1}{2^p}\binom{p+1}{k}$. In case the B-spline basis functions are constructed with open knot vectors, the subdivision matrix is modified at the boundaries. Since the B-splines have a local support over the knot vector, only the p consecutive coarse basis functions at the boundaries are modified. For quadratic basis functions ($p = 2$), the two consecutive modified basis functions are obtained as $N_1^2 = \tilde{N}_1^2 + \frac{1}{2}\tilde{N}_2^2$ and $N_2^2 = \frac{1}{2}\tilde{N}_2^2 + \frac{3}{4}\tilde{N}_3^2 + \frac{1}{4}\tilde{N}_4^2$. For cubic basis functions ($p = 3$), the three consecutive modified basis functions are obtained as $N_1^3 = \tilde{N}_1^3 + \frac{1}{2}\tilde{N}_2^3$, $N_2^3 = \frac{1}{2}\tilde{N}_2^3 + \frac{3}{4}\tilde{N}_3^3 + \frac{3}{16}\tilde{N}_4^3$ and $N_3^3 = \frac{1}{4}\tilde{N}_3^3 + \frac{11}{16}\tilde{N}_4^3 + \frac{1}{2}\tilde{N}_5^3 + \frac{1}{8}\tilde{N}_6^3$. The modifications of the coefficients in the two-scale relation for B-splines formed with a uniform open knot vector are shown in Fig. 2.9. Surface B-spline functions can be obtained as a tensor product of two univariate B-spline functions.

For the numerical examples, we restrict ourselves to the setup of interest which is a film/substrate system composed of two rectangular geometries. Cartesian grid is used to discretize the geometries. Uniform open B-spline basis functions are adopted to approximate the state variables χ, Φ and p. The same approximation spaces are considered for χ and Φ, but a different one for Lagrange multiplier p. The B-spline space for p is obtained by coarsening the fine space of χ or Φ using the two-scale relation discussed earlier in this section. Therefore, the basis functions of all the state variables have the same polynomial degree. Dirichlet boundary conditions are strongly enforced, because the basis functions are interpolant at the boundaries of the domain in the reference configuration. The standard Gaussian quadrature

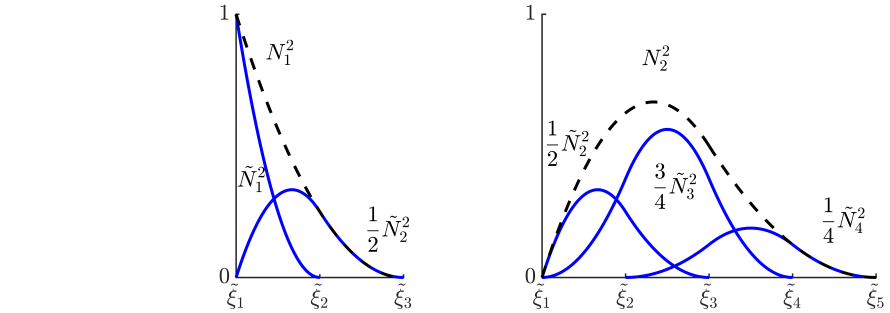

(a) The first basis function close to the boundary (p = 2)

(b) The second basis function close to the boundary (p = 2)

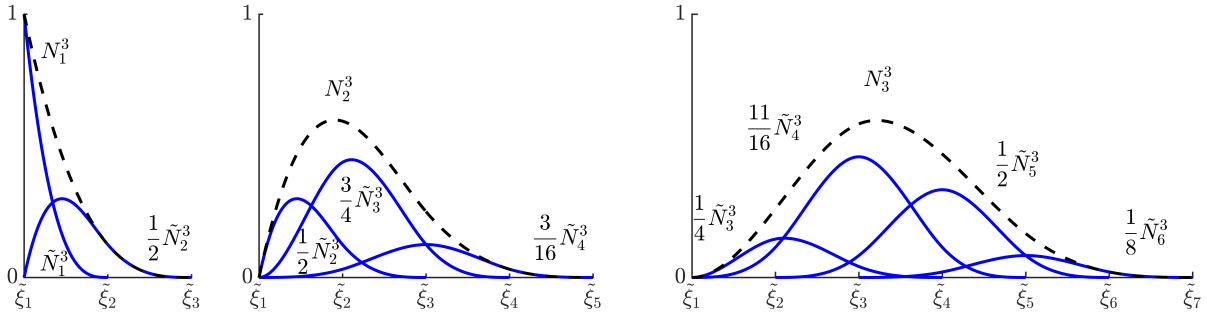

(c) The first basis function close to the boundary (p = 3)

(d) The second basis function close to the boundary (p = 3)

(e) The third basis function close to the boundary (p = 3)

Figure 2.9: The modifications to the two-scale relation for the p successive basis functions in the vicinity of the boundary.

rules are employed to approximate the domain and the boundary integrals. Discretizing the weak form of the problem Eq. (2.77), a nonlinear system of equations is obtained which is solved using Newton-Raphson method. In Newton-Raphson method, the first order Taylor expansion of the residual $\mathcal{R}^{\text{Bimaterial}}$ in Eq. (2.77) around the solution of the previous iteration $\{\boldsymbol{\chi}, \Phi, p\}^{(k-1)}$ must be vanished yielding an increment of the solution of the system at k-th iteration $\{\Delta\boldsymbol{\chi}, \Delta\Phi, \Delta p\}^{(k)}$ as

$$
\begin{aligned}
&\mathcal{R}^{\text{Bimaterial}}[\boldsymbol{\chi}^{(k)}, \Phi^{(k)}, p^{(k)}; \delta\boldsymbol{\chi}, \delta\Phi, \delta p] \approx \\
&+ \mathcal{R}^{\text{Bimaterial}}[\boldsymbol{\chi}^{(k-1)}, \Phi^{(k-1)}, p^{(k-1)}; \delta\boldsymbol{\chi}, \delta\Phi, \delta p] \\
&+ \frac{\partial \mathcal{R}^{\text{Bimaterial}}[\boldsymbol{\chi}^{(k-1)}, \Phi^{(k-1)}, p^{(k-1)}; \delta\boldsymbol{\chi}, \delta\Phi, \delta p]}{\partial \boldsymbol{\chi}} \Delta\boldsymbol{\chi}^{(k)} \\
&+ \frac{\partial \mathcal{R}^{\text{Bimaterial}}[\boldsymbol{\chi}^{(k-1)}, \Phi^{(k-1)}, p^{(k-1)}; \delta\boldsymbol{\chi}, \delta\Phi, \delta p]}{\partial \Phi} \Delta\Phi^{(k)} \\
&+ \frac{\partial \mathcal{R}^{\text{Bimaterial}}[\boldsymbol{\chi}^{(k-1)}, \Phi^{(k-1)}, p^{(k-1)}; \delta\boldsymbol{\chi}, \delta\Phi, \delta p]}{\partial p} \Delta p^{(k)} = 0.
\end{aligned}
\tag{2.84}
$$

Equivalently, Eq. (2.84) can be written as

$$\begin{bmatrix} \mathbf{H}_{\chi\chi} & \mathbf{H}_{\chi\Phi} & \mathbf{H}_{\chi p} \\ \mathbf{H}_{\Phi\chi} & \mathbf{H}_{\Phi\Phi} & \mathbf{0} \\ \mathbf{H}_{p\chi} & \mathbf{0} & \mathbf{0} \end{bmatrix}^{(k-1)} \cdot \begin{bmatrix} \Delta\boldsymbol{\chi} \\ \Delta\Phi \\ \Delta p \end{bmatrix}^{(k)} = -\begin{bmatrix} \mathbf{R}_{\chi} \\ \mathbf{R}_{\Phi} \\ \mathbf{R}_{p} \end{bmatrix}^{(k-1)}, \tag{2.85}$$

which reads find $\{\Delta\boldsymbol{\chi}, \Delta\Phi, \Delta p\}^{(k)}$ given $\{\boldsymbol{\chi}, \Phi, p\}^{(k-1)}$. The variation of the residual functional $\mathcal{R}^{\text{Bimaterial}}$ has been derived in Appendix D. We identify the instability points once the smallest eigenvalue in magnitude of the global stiffness matrix in (2.85) becomes zero (Dortdivanlioglu and Linder, 2019). We then slightly perturb the solution in the direction of the associated eigenvector to reach stable solution.

2.5 On-going and future work

The continuum model derived here can be extended to account for other surface effects, i.e. surface tension, surface chemistry, and absorption. The incorporation of surface tensions, in particular, can be of great importance when dealing with very soft materials in which the elastocappilarity effects play a significant role (Wang and Zhao, 2013). In very soft materials, chemical reactions on the surface can also induce surface instabilities (Li *et al.*, 2013). Therefore, the incorporation of these effects may be important. Besides, as the Neo-Hookean hyperelastic model is mainly considered a valid material model for finite deformation yet with small strains, different elastic material models such as Gent hyperelastic model can be substituted in our formulation which may solve the challenges that may arise when dealing with large strains, for example in the simulation of creasing. We will comment on the challenges of simulation of creasing in the next chapter.

2.6 Concluding remarks

In this chapter, we first shed light on the inherent surface effects of the flexoelectricity models in bulk. We showed that a reversible surface piezoelectric-like effect exists in the Lifshitz-invariant flexoelectric model, while the direct and converse models exhibit a one-way surface piezoelectric-like effect. Furthermore, we characterized the observed boundary layers in terms of the length scales of the model.

Then, we developed a continuum model for flexoelectricity in soft materials considering a symmetric contribution of direct and converse flexoelectricity (Lifshitz-invariant model) as well as material incompressibility. We developed the formulation of weak enforcement of interface conditions with Nitsche's method. Using open B-spline basis functions and employing the subdivision stabilization technique, the governing equations can be solved in a robust way.

Chapter 3

Surface instabilities in a flexoelectric film/ dielectric substrate

In this chapter, using the computational framework described in the previous chapter, we aim to capture the well-known surface instability patterns namely wrinkle, ridge, period-doubling, fold, and crease in a flexoelectric/dielectric bilayer. In an elastic bilayer, the instability patterns are controlled by modulus ratio and prestretch (Wang and Zhao, 2015). To capture the instability patterns, after validation of the implementation, we first study the effect of substrate shear modulus and prestretch on the flexoelectric/dielectric bilayer and explore the electromechanical response of each family of instability patterns. Then, focusing on wrinkling instability, we study the effect of the material's electrical and flexoelectric properties on the flexoelectricity-induced electric response, to gain a better understanding of these parameters.

3.1 Setup

We consider a flexoelectric film with a length L and a dielectric substrate with a length L_0 in the undeformed state (Fig. 3.1a). Plane strain prestretch $\lambda_0 = L/L_0$ is applied to the substrate elongating it to a length L. The prestretched substrate is then bonded to a stress-free film (Fig. 3.1b). In the bonded state, the film and the substrate have thickness h_f and h_s, respectively. The bonded state is the reference configuration in our numerical examples. The bilayer is then compressed to a length l under plane strain condition, and the overall compressive strain can be defined as $\varepsilon = (L - l)/L$ (Fig. 3.1c). Details on how we deal with prestretch can be found in Appendix G.

In the examples shown in this chapter, we consider $h_f = 1\mu m$ and $(h_s + h_f)/h_f = 40$. We simulate displacement-controlled compression of the bilayer. The vertical displacement and shear traction on the bottom of the substrate are set to zero. On the left and right faces of the film and substrate, we set the shear traction to zero, while imposing a displacement to generate the overall compressive strain ε. The top layer of the film is traction-free. Lower

face of the substrate is connected to the ground, i.e. the electric potential is fixed to zero. We consider two cases for the electric boundary condition of the top of the film, either we connect it to the ground (closed-circuit), or we consider charge free boundary condition (open circuit). Other outer faces are considered to be charge free. On the interface, we assume the film and the substrate are perfectly bonded mechanically and electrically, therefore no delamination is allowed. The electric boundary conditions are shown in Fig. 3.2

The following material parameters are considered in the simulations shown in 3.3-3.7.

For the film we consider:

$$G_f = 575\text{MPa}, \quad \epsilon = 9.2\text{nJ/V}^2\text{m}, \quad \mu_{\text{L}} = 100\text{nJ/Vm}, \quad \mu_{\text{T}} = 50\text{nJ/Vm}, \quad \ell_2 = 0.5\mu\text{m}, \\ \mu_{\text{S}} = \ell_1 = 0, \tag{3.1}$$

G_f being the shear modulus of the film.

For the substrate, a set of material parameters are considered as:

$$G_s = 0.575 - 1150\text{MPa}, \quad \epsilon = 9.2\text{nJ/V}^2\text{m}, \quad \ell_2 = 10\mu\text{m}, \quad \mu_{\text{L}} = \mu_{\text{T}} = \mu_{\text{S}} = \ell_1 = 0, \tag{3.2}$$

G_s being the shear modulus of the substrate. Note that the shear moduli described above are ground state shear moduli associated to the state shown in Fig. 3.1a. Worth mentioning that the shear moduli ranges considered here are in the range between the shear moduli of PDMS and PVDF. The electric permittivity is in the same order as polymer-based dielectrics (Zha *et al.*, 2021). The magnitude of flexoelectric coefficients was chosen as $\boldsymbol{\mu} = (\epsilon - \epsilon_0)f$, where ϵ_0 is the vacuum permittivity and f is the flexocoupling coefficient. We consider $f \approx 12$. The values of ℓ_1 are set to 0. This allows us to be able to compare our results (transition strains) with the results available in the literature for purely elastic bilayers. The values of ℓ_2 are chosen such that for the considered range of material parameters and the mesh sizes, we obtain stable results.

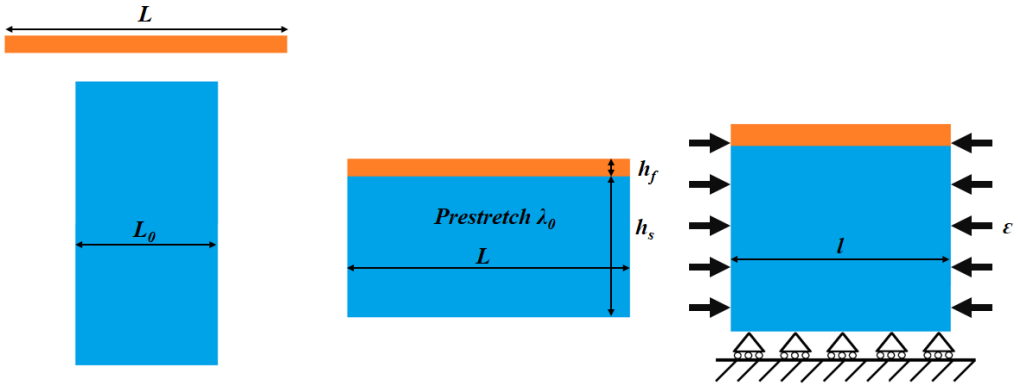

(a) Undeformed state (b) Bonded state (c) Deformed state

Figure 3.1: A film/substrate system in different states. (a) In the undeformed state, the film has a length L, while the substrate has a length L_0 (b) In the bonded state, the substrate is prestretched to length L and bonded with a stress-free film where $\lambda_0 = L/L_0$ is the prestretch. (c) In the deformed state, both the film and the substrate are compressed together to length l, where the compressive strain is $\varepsilon = (L - l)/L$.

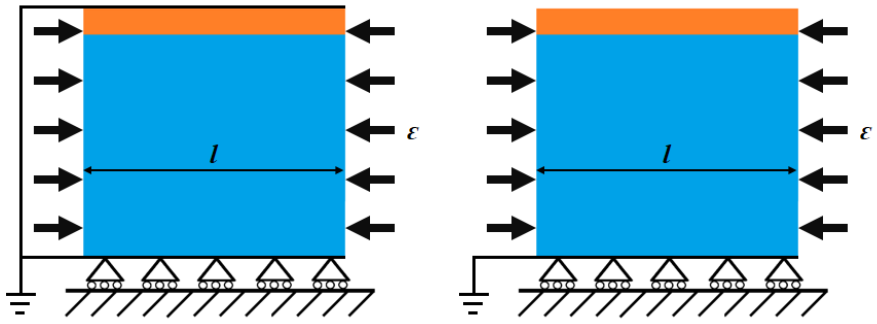

(a) Closed circuit. (b) Open circuit.

Figure 3.2: Electric boundary conditions of the bilayer.

3.2 Validation

In this section, we first partially validate our implementation by comparing the critical wrinkling strains in an elastic bilayer with the results available in the literature. We then comment

on the other tests that were performed to check the validity of the implementation. We consider the film/substrate system shown in Fig. 3.1, in which the incompressible substrate in plane strain conditions has undergone a prestretch of $(\lambda_0, 1/\lambda_0)$ prior to attaching to the film. The compressive strain in the film at the onset of wrinkling can be predicted by a simple formula (Cao and Hutchinson, 2012b):

$$\varepsilon_w = \frac{1}{4}(\Lambda\frac{3G_s}{G_f})^{2/3}. \tag{3.3}$$

where G_s and G_f are the shear modulus of substrate and film, respectively and $\Lambda = \frac{1}{2}(1 + \lambda_0^2)$. As discussed in (Cao and Hutchinson, 2012b), this formula is expected to predict the wrinkling critical strains of bilayers with a good accuracy when the wrinkling critical strain is small. Here, the only nonzero material parameters are G_f and G_s which are considered from Eq. 3.1 and Eq. 3.2, respectively. We consider $G_f/G_s = 5 - 1000$, and $\lambda_0 = \{1, 2\}$. For validation purposes, we compare in Fig. 3.3 the compressive strain in the film at the onset of wrinkling computed from the simulations to the theoretical results of Eq. (3.3). As shown, numerical and theoretical results match perfectly for large G_f/G_s for which the critical wrinkling strain is small. The figure shows that without prestretch, Eq. (3.3) can predict the wrinkle critical strain with a good accuracy even for small moduli ratios. Furthermore, Cao and Hutchinson (2012b) obtained the wrinkle critical strains $\varepsilon_w \approx \{0.166, 0.171\}$ for $\lambda_0 = \{1, 2\}$, respectively, and $G_f/G_s = 5$. This agrees perfectly with our calculated wrinkle critical strains $\varepsilon_w = \{0.166, 0.1715\}$.

Apart from the validation of the elastic case, we performed gradient checking to make sure that the implementation of the residual and the hessian of the electromechanical enthalpy is correct. Besides, we checked that by applying small loadings in the nonlinear model, we retrieve the solution obtained from the linear model. Furthermore, mesh convergence of the results shown in 3.4-3.7 has been performed.

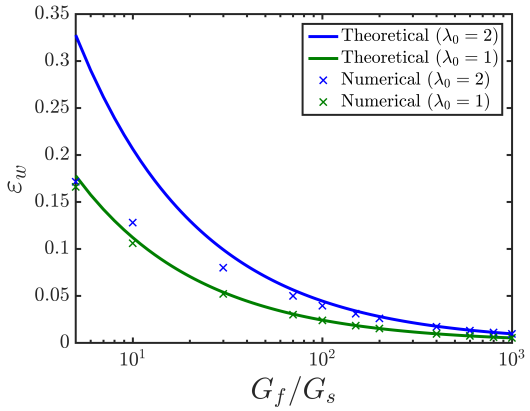

Figure 3.3: Compressive strain in film at the onset of wrinkling.

3.3 Wrinkling

We consider $L = 160\mu m$, $G_f/G_s = \{100, 200, 400, 800\}$, $\lambda_0 = \{1, 1.5, 2\}$. Both closed circuit and open circuit boundary conditions have been considered. The number of finest elements of the film (elements to discretize displacement and electric potential fields) is considered to be $\{160, 8\}$ for width and thickness, respectively, while that of the substrate is $\{160, 40\}$. The bilayer is loaded to an overall compressive strain $\varepsilon = 0.05$ so that wrinkle is the only instability pattern obtained in this set of simulations.

For the case of closed circuit, Fig. 3.4a compares the net vertical electric field across the film thickness $\bar{E}_Y$, on a wrinkle peak for the case $\lambda_0 = 1$. The net vertical electric field across the film is defined as $\bar{E}_Y = -(\Phi^t_{film} - \Phi^b_{film})/h_f$, where Φ^t_{film} and Φ^b_{film} are the electric potentials of the points with the same X-coordinate on top and bottom of the film, respectively. Interestingly, it can be seen that before the onset of wrinkle instability, the $\bar{E}_Y$ increases linearly. While this linear increase of $\bar{E}_Y$ may be surprising, as before the start of wrinkling, the system is flat and thus no strain gradient is generated, the response is related to converse flexoelectricity term in Eq. (2.51) which couples uniform strain with electric field gradient. As a result of this, compression of a flexoelectric thin film induces electric field gradients near its surfaces, as discussed in detail in Section 2.2.1.2. Since there is a lack of symmetry in the boundary conditions of the film (the top having an electrode with zero potential and the bottom having a substrate with interface continuities), under compression, a mean electric field in the thickness direction of the film is induced. Besides, this behavior is similar to the behavior of a closed

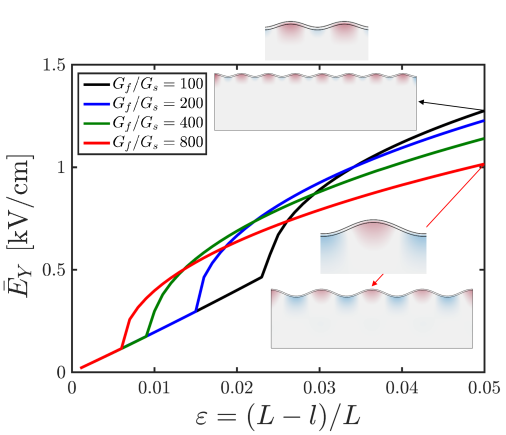

(a) Net vertical electric field $\bar{E}_Y$ of the wrinkle peak for the case $\lambda_0 = 1$ and different modulus ratios G_f/G_s.

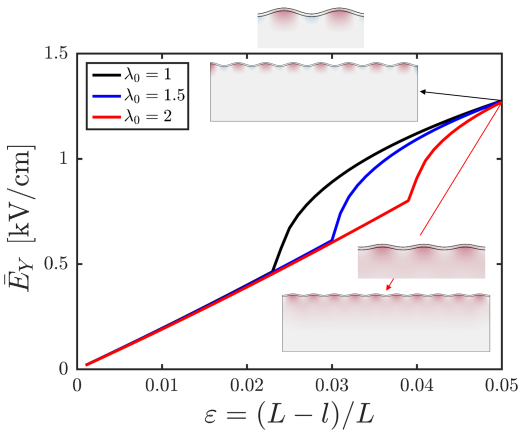

(b) Net vertical electric field $\bar{E}_Y$ of the wrinkle peak for the case $G_f/G_s = 100$ and different substrate prestretches λ_0.

Figure 3.4: Effect of modulus ratio and substrate prestretch on the electric field generated on a wrinkle peak in closed circuit.

circuit electret under homogeneous deformation which further reveals the similarities between electrets and flexoelectric materials (Wen *et al.*, 2019). For a given prestretch, increasing the modulus ratio leads to a decrease in the wrinkle critical strain ε_w and wrinkle wavenumber. Furthermore, Fig. 3.4a shows that the rate of the increase of $\bar{E}_Y$ on a wrinkle peak decreases as the modulus ratio increases. Fig. 3.4b shows that increasing prestretch has a similar effect to decreasing modulus ratio (Fig. 3.4a) on ε_w, $\bar{E}_Y$ generated on the wrinkle peak as well as wrinkle wavenumber. This is because prestretch causes an anisotropic stiffening of the substrate, as discussed by Cao and Hutchinson (2012b).

Fig. 3.5 summarizes the results of the open circuit case. Comparing the insets in Figs. 3.5 and 3.4, it is clear that the change of the electrical boundary conditions did not noticeably change the deformations, i.e. the wavenumbers remained unchanged. Besides, this figure shows that the rate of the increase of the absolute value of Φ^t_{film} on a wrinkle peak increases by decreasing modulus ratio and increasing prestretch.

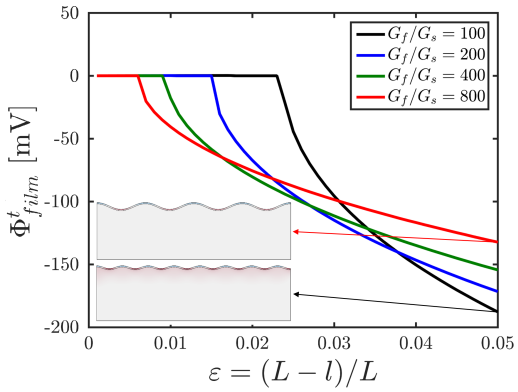

(a) Electric potential of the top of the film Φ^t_{film} on a wrinkle peak for the case $\lambda_0 = 1$ and different modulus ratios G_f/G_s.

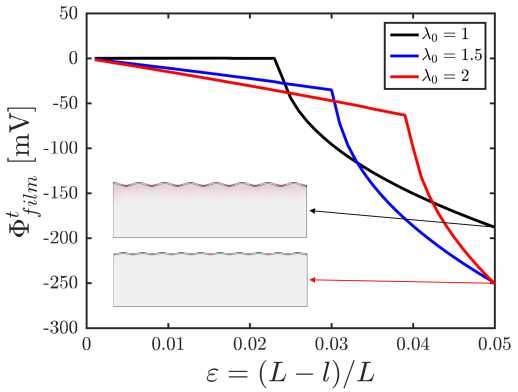

(b) Electric potential of the top of the film Φ^t_{film} on a wrinkle peak for the case $G_f/G_s = 100$ and different substrate prestretches λ_0.

Figure 3.5: Effect of modulus ratio and substrate prestretch on electric potential Φ^t_{film} generated on a wrinkle peak in open circuit case.

3.4 Wrinkle/ridge transition

We study next the transition between wrinkle and ridge instability patterns in a flexoelectric/dielectric bilayer. In this example, we consider $L = 160\mu m$, $G_f/G_s = 1000$, $\lambda_0 = 2$, and closed circuit boundary conditions. The number of finest elements of the film (elements to discretize displacement and electric potential fields) is considered to be $\{N_x, 8\}$ for width and thickness, respectively, while that of the substrate is $\{N_x, N_x/4\}$. The presented results are obtained with to $N_x = 160$.

Fig. 3.6 shows the evolution of instability patterns in a film/substrate system subjected to

an overall compressive strain ε and the resulting electric potential distribution. From the figure, it can be observed that as we compress the film/substrate system, wrinkle instability pattern appears (Figs. 3.6a) followed by a transition to localized ridge pattern (Fig. 3.6b). Increasing the overall compressive strain ε results in an increase in the height to thickness aspect ratio of the ridge (Figs. 3.6c).

To quantify the transition between wrinkle and localized ridge patterns, we incrementally load the film/substrate system to compressive strain $\varepsilon = 0.04$, and then incrementally unloading it to the bonded state. Fig. 3.7a shows the normalized relative vertical displacement of the ridge peak $\bar{u}_Y$ for the stable equilibrium states. The normalized relative vertical displacement can be defined as $\bar{u}_Y = (u_Y - u_Y^0)/h_f$, where u_Y is the vertical displacement of a point on the top of the film, u_Y^0 is the vertical displacement of the same system in homogeneous deformation state. From the figure, we identify three critical compressive strains namely wrinkle critical strain $\varepsilon_w = 0.00932 \pm 0.00004$, wrinkle to ridge transition strain $\varepsilon_{w\to r} = 0.0300 \pm 0.0004$, and ridge to wrinkle transition strain $\varepsilon_{r\to w} = 0.0244 \pm 0.0004$. When $\varepsilon \leq \varepsilon_w$, the film is flat. When $\varepsilon_w < \varepsilon < \varepsilon_{r\to w}$, wrinkle state appears and it is the only stable equilibrium state. When $\varepsilon_{r\to w} \leq \varepsilon \leq \varepsilon_{w\to r}$, wrinkle and ridge states are both the equilibrium states, formation of each of which depends on the prior compression history. When $\varepsilon_{w\to r} < \varepsilon$, ridge is the only stable equilibrium state. It is worthwhile to note that the mentioned transitions in an elastic continuum have been studied by Jin *et al.* (2015). In the electromechanical problem, these transitions can also occur with electrically loading the system. In Section 4.1, we provide examples of such electrically activated transitions. Fig. 3.7b shows the net vertical electric field across the film thickness on the ridge peak, for the different states described above. The transition between wrinkle and ridge state is abrupt causing a sharp change in the displacement and the resulting vertical electric field $\bar{E}_Y$ on the ridge peak. This figure shows that in ridge state, the net vertical electric field $\bar{E}_Y$ increases faster than that in the wrinkle state. This is due to the fact that the curvature of the ridge peak increases faster than that of a wrinkle peak as a result of deformation localization. This causes a faster rate of increase of the strain gradients

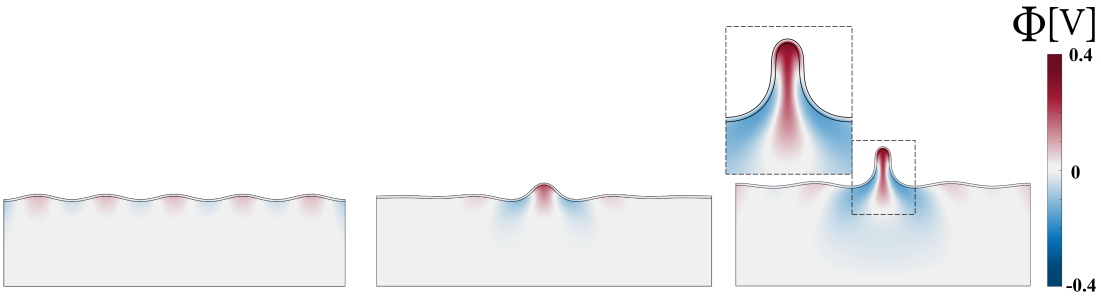

(a) $\varepsilon = 0.024$ (b) $\varepsilon = 0.04$ (c) $\varepsilon = 0.16$

Figure 3.6: A flexoelectric/dielectric bilayer with $G_f/G_s = 1000$, and $\lambda_0 = 2$ subjected to different compressive strains ε and the distribution of the electric potential [V].

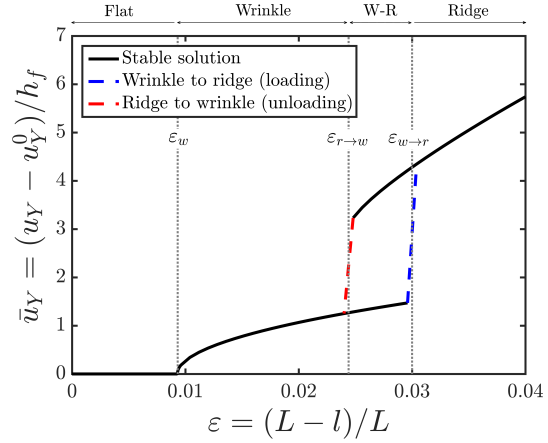

(a) Normalized relative vertical displacement of the ridge peak.

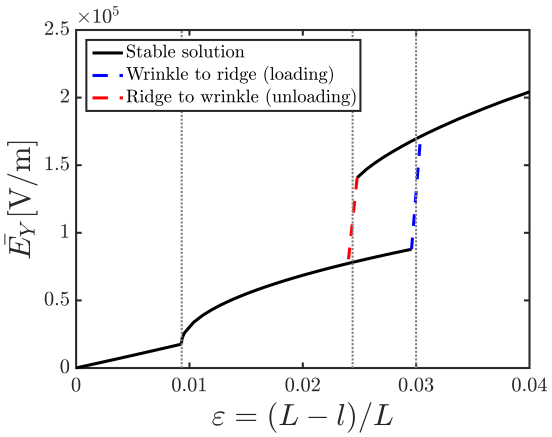

(b) Net vertical electric field $\bar{E}_Y$ of the ridge peak.

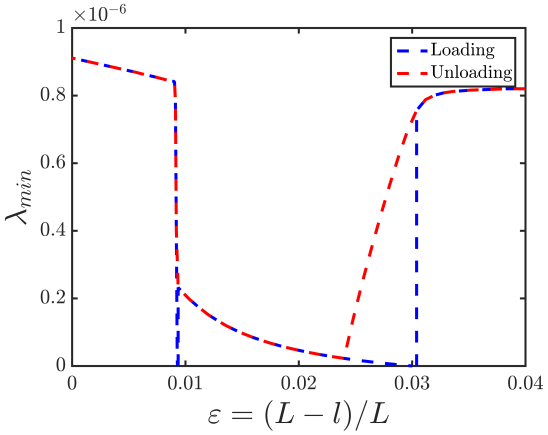

(c) Minimum eigenvalue in magnitude of the system.

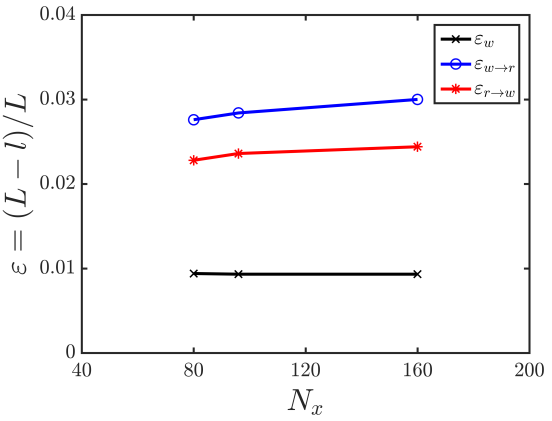

(d) Convergence of ε_w, $\varepsilon_{w\to r}$ and $\varepsilon_{r\to w}$ compressive strains with respect to mesh size.

Figure 3.7: Wrinkle-ridge transition in a flexoelectric/dielectric bilayer with $G_f/G_s = 1000$ and $\lambda_0 = 2$.

and thus the electric field generated due to direct flexoelectricity. The smallest eigenvalue in magnitude of the global stiffness matrix is depicted in Fig. 3.7c as a function of ε, which shows that tracking the changes in the signature of the global stiffness matrix is a powerful method for identifying instability points in an indeterminate system. To check the convergence of the critical compressive strains ε_w, $\varepsilon_{r\to w}$ and $\varepsilon_{w\to r}$, we simulated the same problem with a different number of elements. Fig. 3.7d shows the convergence of the critical compressive strains by refining the mesh size.

3.5 Period-doubling bifurcation

We show how period-doubling bifurcation in a flexoelectric/dielectric bilayer affects the electrical response of the system. We consider $L = 160\mu m$, $G_f/G_s = 100$, $\lambda_0 = 1$, and closed circuit boundary conditions. The number of finest elements of the film (elements to discretize displacement and electric potential fields) is considered to be $\{N_x, 8\}$ for width and thickness, respectively, while that of the substrate is $\{N_x, N_x/4\}$. The presented results are obtained with $N_x = 200$. Fig. 3.8 shows the instability patterns in the mentioned film/substrate system subjected to an overall compressive strain ε and the resulting electric potential distribution. As we compress the system, wrinkle instability pattern is formed followed by period-doubling bifurcation. The period-doubling bifurcation can be tracked by tracing the vertical displacements of two neighboring wrinkle valleys, where following the period-doubling bifurcation strain ε_{PD}, one of the valleys goes deeper to the substrate, while the other takes a reverse path.

Fig. 3.9a shows the normalized relative vertical displacement $\bar{u}_Y$ of two neighboring wrinkle valleys (points A and B depicted in Figs. 3.8a and 3.8b). From this figure, wrinkle critical strain $\varepsilon_w = 0.02325 \pm 0.0015$ and period-doubling bifurcation strain $\varepsilon_{PD} = 0.18675 \pm 0.0015$ can be identified. Fig. 3.9b shows how period-doubling bifurcation affects the net vertical electric field $\bar{E}_Y$ generated on two neighboring wrinkle valleys. On point A, the magnitude of $\bar{E}_Y$ decreases since the curvature decreases, whereas, on point B, the magnitude of $\bar{E}_Y$ increases due to a rise in the curvature. Fig.3.9c shows the behavior of the smallest eigenvalue in magnitude of the global stiffness matrix where a sharp change of the eigenvalue in the wrinkle and period-doubling critical strains is evident. The convergence of the critical compressive strains ε_w and ε_{PD} for a different number of elements is shown in Fig. 3.9d.

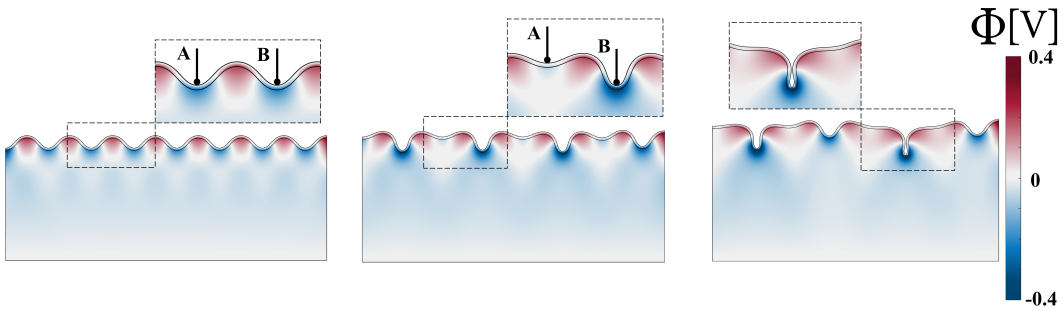

(a) $\varepsilon = 0.18$ (b) $\varepsilon = 0.225$ (c) $\varepsilon = 0.27$

Figure 3.8: A flexoelectric/dielectric bilayer with $G_f/G_s = 100$, and $\lambda_0 = 1$ subjected to different compressive strains ε and the distribution of the electric potential [V].

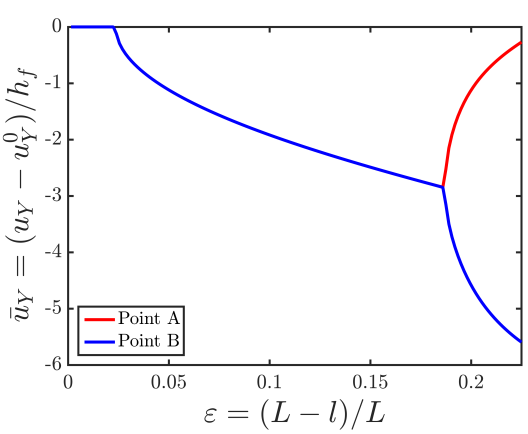

(a) Normalized relative vertical displacement $\bar{u}_Y$ of two neighboring wrinkle valleys.

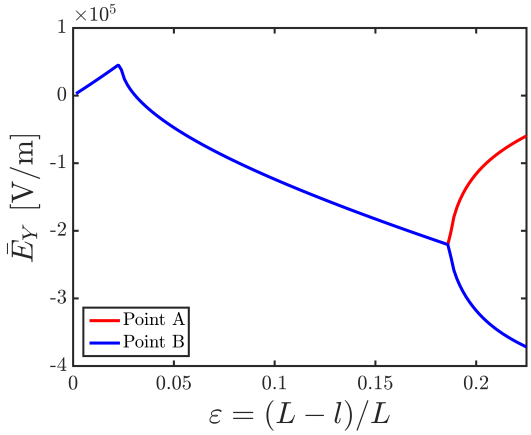

(b) Net vertical electric field $\bar{E}_Y$ of two neighboring wrinkle valleys.

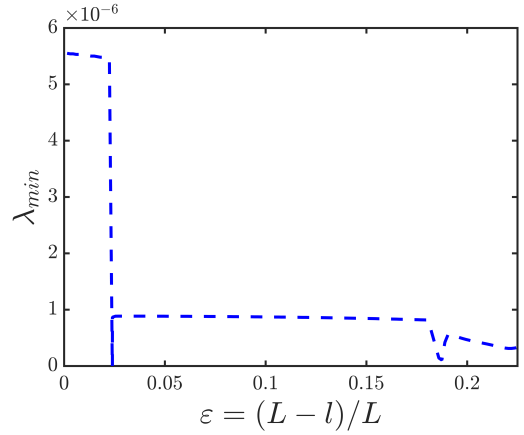

(c) Minimum eigenvalue in magnitude of the system.

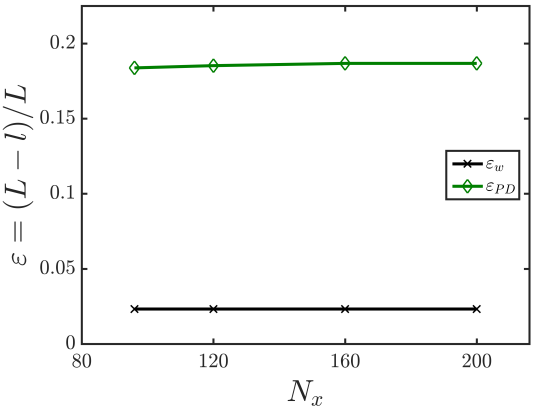

(d) Convergence of ε_w and ε_{PD} compressive strains with respect to mesh size.

Figure 3.9: Period-doubling bifurcation in a flexoelectric/dielectric bilayer with $G_f/G_s = 100$, and $\lambda_0 = 1$.

3.6 Folding

This example is devoted to the formation of folds in a flexoelectric/dielectric bilayer. We consider $L = 36\mu m$, $G_f/G_s = 8$, $\lambda_0 = 1$, and closed circuit boundary conditions. The number of finest elements of the film (elements to discretize displacement and electric potential fields) is considered to be $\{N_x, 8\}$ for width and thickness, respectively, while that of the substrate is $\{N_x, \sim (10N_x/9)\}$. The presented results are obtained with $N_x = 90$. Fig. 3.10 shows the instability patterns in the mentioned film/substrate system subjected to an overall compressive strain ε and the resulting electric potential distribution. Compressing the system results in formation of wrinkles as the primary instability pattern (Fig. 3.10a). After that, a localization process occurs causing the folds to emerge in the system (Fig. 3.10b).

Fig. 3.11a shows the normalized relative vertical displacement $\bar{u}_Y$ of the fold tip. From this figure, the wrinkle critical strain $\varepsilon_w = 0.1225 \pm 0.00833$ and the fold critical strain $\varepsilon_f = 0.16028 \pm 0.000278$ can be identified. Our calculated wrinkle and fold critical strains for the flexoelectric/dielectric bilayer agree well with the critical strains reported in (Cao and Hutchinson, 2012b) ($\varepsilon_w \approx 0.1226$ and $\varepsilon_f \approx 0.1651$) for elastic bilayer of Neo-Hookean materials. Fig. 3.11b depicts the net vertical electric field on the fold tip $\bar{E}_Y$ across the film thickness which shows a sudden change in the $\bar{E}_Y$ due to the localization process causing folds to form. The behavior of the smallest eigenvalue in magnitude of the global stiffness matrix has been shown in Fig.3.11c where a sharp change of the eigenvalue in the wrinkle and fold critical strains can be seen. The convergence of the critical compressive strains ε_w and ε_f for different number of elements is shown in Fig. 3.11d.

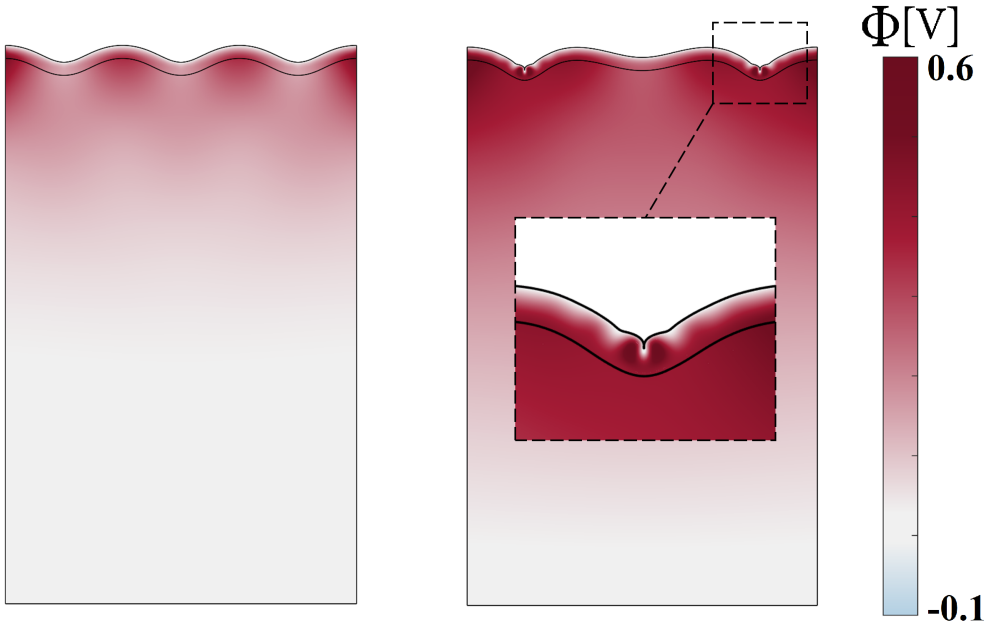

(a) $\varepsilon = 0.1589$ (b) $\varepsilon = 0.1606$

Figure 3.10: Distribution of electric potential Φ on a flexoelectric/dielectric bilayer with $G_f/G_s = 8$, and $\lambda_0 = 1$ subjected to two different compressive strains ε.

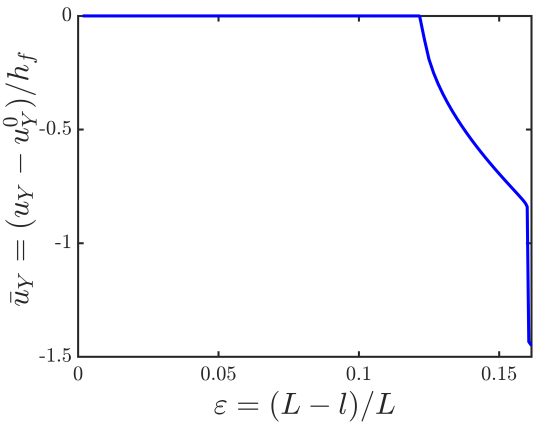

(a) Normalized relative vertical displacement $\bar{u}_Y$ of the fold tip.

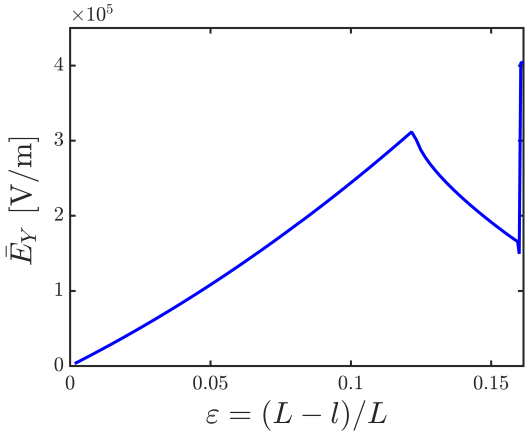

(b) Net vertical electric field $\bar{E}_Y$ of fold tip.

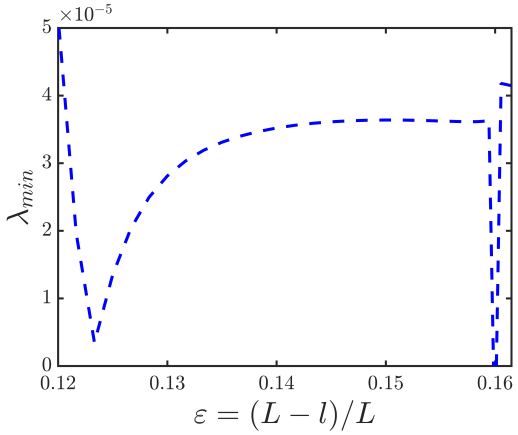

(c) Minimum eigenvalue in magnitude of the system.

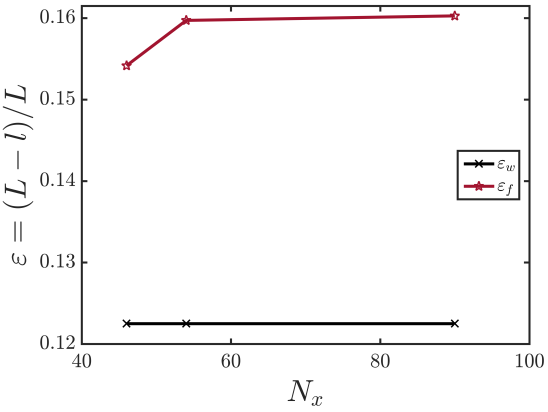

(d) Convergence of ε_w and ε_f compressive strains with respect to mesh size.

Figure 3.11: Wrinkle to fold transition in a flexoelectric/dielectric bilayer with $G_f/G_s = 8$, and $\lambda_0 = 1$.

3.7 Creasing

In this example, we study the emergence of creases in a flexoelectric/dielectric bilayer. We consider $L = 20\mu m$, $G_f/G_s = 0.5$, $\lambda_0 = 1$, and closed circuit boundary conditions. The number of finest elements (elements to discretize displacement and electric potential fields) is considered to be $\{N_x, 8\}$ for width and thickness, respectively, while those of the substrate are $\{N_x, N_x/2\}$. As we compress the system, above a critical overall compressive strain ε_{sw}, surface of film starts to wrinkle (Fig. 3.12a). Note that this surface wrinkling is different than the wrinkling of the film/substrate system described in the previous examples in which both film and the substrate wrinkle together. By increasing the overall compressive strain, the surface wrinkles collapse to form creases (Figs. 3.12b, 3.12c). Our simulations show that at a critical overall

compressive strain $\varepsilon_{sw} = 0.2325 \pm 0.00083$, surface of film starts to wrinkle. It is important to note that both surface wrinkle and crease have an unusual feature that their wavelength is undetermined (Cao and Hutchinson, 2012a). In our simulations, although we achieved the convergence of ε_{sw}, we observed a dependence of the wavelength on the mesh size.

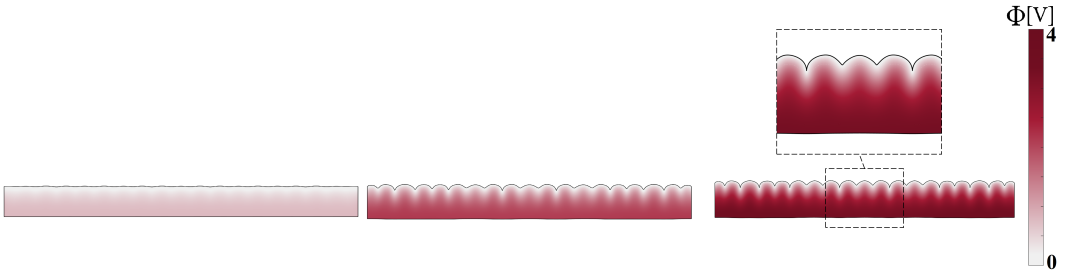

(a) $\varepsilon = 0.235$ (b) $\varepsilon = 0.3$ (c) $\varepsilon = 0.35$

Figure 3.12: Creasing instability in a flexoelectric/dielectric bilayer with $G_f/G_s = 0.5$, and $\lambda_0 = 1$ subjected to different compressive strains ε and the distribution of the electric potential [V]. In this figure, only the film is shown.

3.8 Effect of material's electrical and flexoelectric properties on the electric response in wrinkling

In this section, with the final goal of optimizing the electromechanical response of the instability-based flexoelectric devices, we study the effect of the material properties (electrical properties and flexoelectric coefficients) on the flexoelectricity-induced electric response. For this, focusing on wrinkling instability, we systematically study the effect of electrical properties of the film or the substrate on the net vertical electric field generated on a wrinkle peak.

In all the examples, the setup and boundary conditions are the same as Section 3.1. Closed circuit boundary condition is considered. We consider $h_f = 1\mu m$ and $(h_s + h_f)/h_f = 40$, and $L = 160\mu m$. The number of finest elements of the film (elements to discretize displacement and electric potential fields) is considered to be $\{160, 8\}$ for width and thickness, respectively, while that of the substrate is $\{160, 40\}$. The material properties are chosen such that the wrinkle pattern is obtained. It is worthwhile to mention that in all the cases below, the changes in the material properties did not noticeably change the deformation fields. In other words, the wavelength of the wrinkles remained unchanged. Therefore, the cross effects due to changes in the deformation field have been excluded from the results provided in this section.

3.8.1 Effect of film electric permittivity on the net electric vertical field generated on a wrinkle peak

In the first example, the effect of the electric permittivity of the film on the generated net vertical electric field on a wrinkle peak has been studied. All the material properties are kept

constant except the electric permittivity of the film. The following material properties have been considered for the film:

$$G_f = 575MPa, \qquad \epsilon_f = \{9.2, 92\}nJ/V^2m, \qquad \mu_{\mathrm{L}} = 100nJ/Vm, \qquad \mu_{\mathrm{T}} = 50nJ/Vm,$$
$$\ell_2 = 0.5\mu m, \qquad \mu_{\mathrm{S}} = \ell_1 = 0, \tag{3.4}$$

G_f being the shear modulus of the film, and ϵ_f is the film electric permittivity. For the substrate, the following material properties are considered:

$$G_s = 5.75MPa, \qquad \epsilon_s = 9.2nJ/V^2m, \qquad \ell_2 = 1\mu m, \qquad \mu_{\mathrm{L}} = \mu_{\mathrm{T}} = \mu_{\mathrm{S}} = \ell_1 = 0. \tag{3.5}$$

G_s being the shear modulus of the substrate, and ϵ_s is the substrate electric permittivity. No prestretch in the substrate has been considered ($\lambda_0 = 1$). It should be noted that physically speaking, the flexoelectric coefficients linearly depend on electric permittivity. However, in this section, to gain intuition about the sole effect of film electric permittivity, we neglect this dependence. Fig. 3.13 shows that decreasing the electric permittivity results in an increase in the net vertical electric field. This is because the lower the electric permittivity is the more polarizable the material becomes. Therefore, fixing the other material properties and for the same deformation, the electric field is inversely proportional to the electric permittivity of the film.

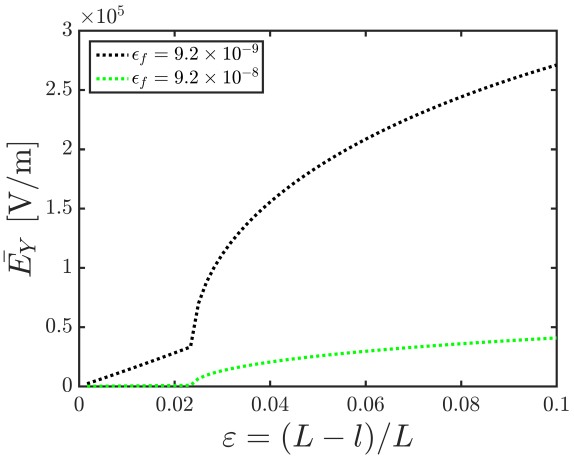

Figure 3.13: Effect of film electric permittivity on the net vertical electric field generated on a wrinkle peak.

3.8.2 Effect of substrate electric permittivity on the net vertical electric field generated on a wrinkle peak.

This example studies the effect of the electric permittivity of the substrate on the induced net vertical electric field generated on a wrinkle peak. All the material properties are kept constant except the substrate electric permittivity. The following material properties have been considered for the film:

$$G_f = 575MPa, \qquad \epsilon_f = 9.2nJ/V^2m, \qquad \mu_{\mathrm{L}} = 100nJ/Vm, \qquad \mu_{\mathrm{T}} = 50nJ/Vm,$$
$$\ell_2 = 0.5\mu m, \qquad \mu_{\mathrm{S}} = \ell_1 = 0, \tag{3.6}$$

G_f being the shear modulus of the film, and ϵ_f is the film electric permittivity. For the substrate, a set of material parameters are considered:

$$G_s = 5.75MPa, \quad \epsilon_s = \{0.92, 9.2, 92\}nJ/V^2m, \quad \ell_2 = 1\mu m, \quad \mu_{\mathrm{L}} = \mu_{\mathrm{T}} = \mu_{\mathrm{S}} = \ell_1 = 0. \tag{3.7}$$

G_s being the shear modulus of the substrate, and ϵ_s is the substrate electric permittivity. No prestretch in the substrate has been considered ($\lambda_0 = 1$). Fig. 3.14 shows that similar to the

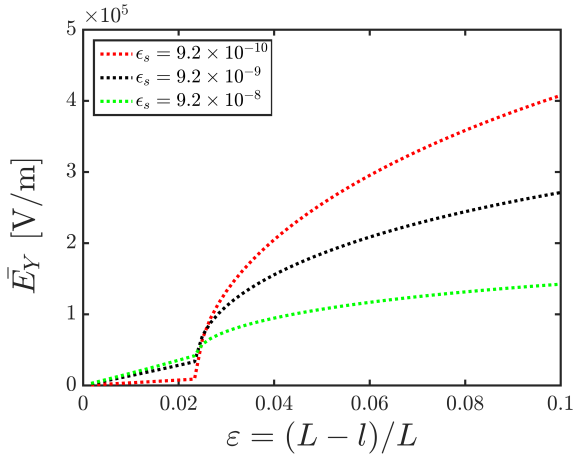

Figure 3.14: Effect of substrate electric permittivity on the net vertical electric field generated on a wrinkle peak.

film, increasing the electric permittivity of the substrate results in a decrease in the net vertical electric field generated on a wrinkle peak. It is worthwhile to note that the electric permittivity of the conductors is infinite. Therefore, increasing the electric permittivity of the substrate to infinity is equivalent to applying electrode boundary conditions on the bottom of the film.

3.8.3 Effect of film flexoelectric coefficients on the net vertical electric field generated on a wrinkle peak.

In this example, the effect of film flexoelectric coefficients on the net vertical electric field generated on a wrinkle peak is studied. All the material properties are kept constant except the flexoelectric coefficients μ_L, μ_T, and μ_S. A combination of these coefficients has been considered to better understand their effect on the generated electric response in wrinkling. The following material properties have been considered for the film:

$$G_f = 575MPa, \quad \epsilon = 9.2nJ/V^2m, \quad \mu_{\mathrm{L}} = \{0, 100\}nJ/Vm, \quad \mu_{\mathrm{T}} = \{0, 50, 100\}nJ/Vm,$$
$$\mu_{\mathrm{S}} = \{0, 100\}, \qquad \ell_2 = 0.5\mu m, \qquad \ell_1 = 0, \quad (3.8)$$

G_f being the shear modulus of the film. For the substrate, the following material parameters are considered:

$$G_s = 5.75MPa, \qquad \epsilon = 9.2nJ/V^2m, \qquad \ell_2 = 1\mu m, \qquad \mu_{\mathrm{L}} = \mu_{\mathrm{T}} = \mu_{\mathrm{S}} = \ell_1 = 0. \qquad (3.9)$$

G_s being the shear modulus of the substrate. No prestretch in the substrate has been considered ($\lambda_0 = 1$). Fig. 3.15 shows that μ_L and μ_T induce electric field of approximately the same

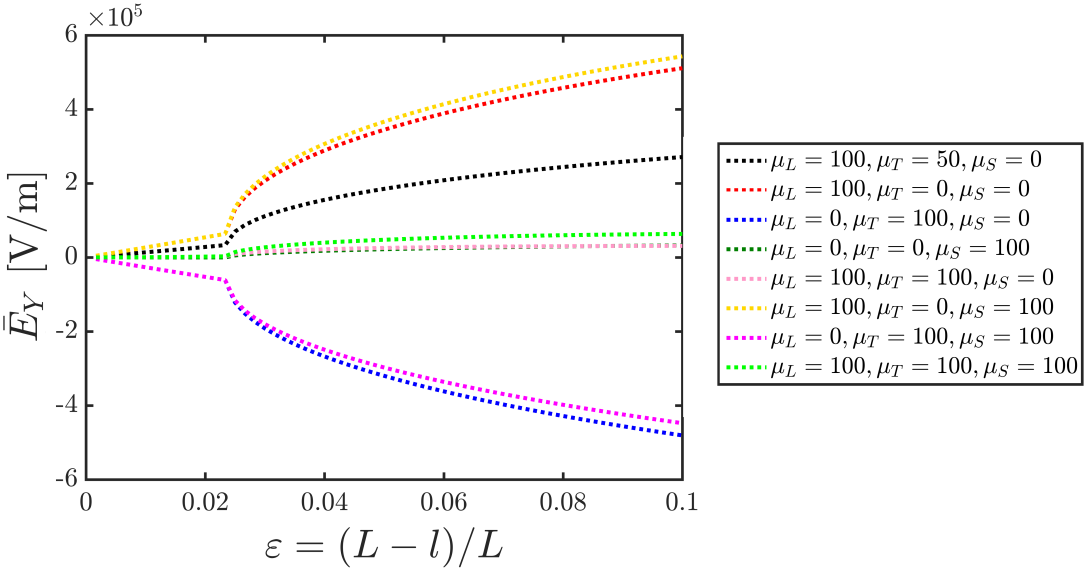

Figure 3.15: Effect of film flexoelectric coefficients on the net vertical electric field generated on a wrinkle peak.

magnitude but with a different sign, in the flat and wrinkle states. Also, the contribution of μ_S in the generated electric field on a winkle peak in this example is small. Besides, as the coupling is linear, for the same deformation, the electric response of any combination of

flexoelectric coefficients can be obtained by superposing their response. So, considering an isotropic flexoelectric tensor, i.e. $\mu_S = (\mu_L - \mu_T)/2$, the optimal choice is $\mu_L = -\mu_T = \mu_S$.

3.8.4 Effect of film l_2 on the net vertical electric field generated on a wrinkle peak.

In this example, we study the effect of gradient dielectricity length scale l_2 on the net vertical electric field generated on a wrinkle peak. All the material properties are kept constant except the film l_2. The following material properties have been considered for the film:

$$G_f = 575MPa, \qquad \epsilon = 9.2nJ/V^2m, \quad \mu_{\mathrm{L}} = 100nJ/Vm, \quad \mu_{\mathrm{T}} = 50nJ/Vm,$$
$$\ell_2\mathrm{film} = \{0.125, 0.25, 0.5\}\mu m, \qquad \mu_{\mathrm{S}} = \ell_1 = 0, \tag{3.10}$$

G_f being the shear modulus of the film. For the substrate, the following material parameters are considered:

$$G_s = 5.75MPa, \quad \epsilon = 9.2nJ/V^2m, \quad \ell_2\mathrm{substrate} = 1\mu m, \quad \mu_{\mathrm{L}} = \mu_{\mathrm{T}} = \mu_{\mathrm{S}} = \ell_1 = 0. \tag{3.11}$$

G_s being the shear modulus of the substrate. No prestretch in the substrate has been considered ($\lambda_0 = 1$). Fig. 3.16 shows that the flexoelectric-induced electric field is inversely proportional

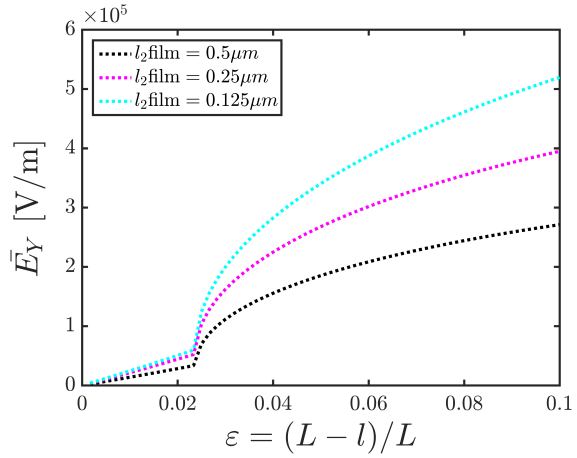

Figure 3.16: Effect of film l_2 on the net vertical electric field generated on a wrinkle peak.

to the film l_2. This is because, in the electromechanical enthalpy, the gradient dielectricity term penalizes high gradients of the electric field consequently regularizing the electric field. Increasing l_2 enhances the contribution of this term which results in a decrease in the electric field. From this figure, it can be noted that to obtain accurate quantitative simulation results, l_2 should be physically characterized, as the solutions are considerably sensitive to this parameter.

3.8.5 Effect of substrate l_2 on the net vertical electric field generated on a wrinkle peak.

In this example, we study the effect of substrate l_2 on the net vertical electric field generated on a wrinkle peak. All the material properties are kept constant except the substrate l_2. The following material properties have been considered for the film:

$$G_f = 575MPa, \quad \epsilon = 9.2nJ/V^2m, \quad \mu_{\mathrm{L}} = 100nJ/Vm, \quad \mu_{\mathrm{T}} = 50nJ/Vm, \quad \ell_2\mathrm{film} = 0.5\mu m, \quad \mu_{\mathrm{S}} = \ell_1 = 0, \tag{3.12}$$

G_f being the shear modulus of the film. For the substrate, the following material parameters are considered:

$$G_s = 5.75MPa, \quad \epsilon = 9.2nJ/V^2m, \quad \ell_2\mathrm{substrate} = \{1, 2, 4\}\mu m, \quad \mu_{\mathrm{L}} = \mu_{\mathrm{T}} = \mu_{\mathrm{S}} = \ell_1 = 0. \tag{3.13}$$

G_s being the shear modulus of the substrate. No prestretch in the substrate has been considered ($\lambda_0 = 1$). Fig. 3.17 shows that increasing substrate l_2 causes a decrease in the electric field

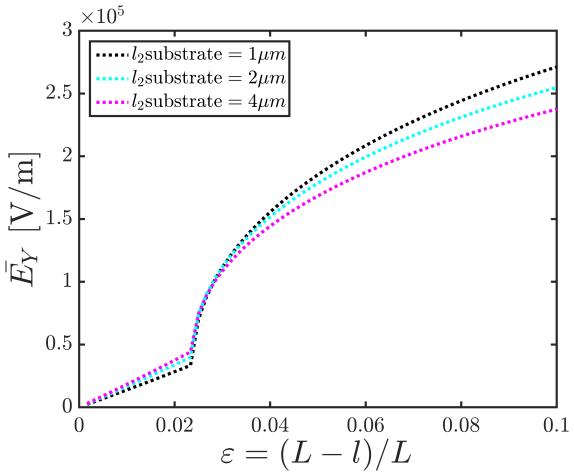

Figure 3.17: Effect of substrate l_2 on the net vertical electric field generated on a wrinkle peak.

generated on a winkle peak. However, the effect is modest compared to that of the film shown in 3.16.

3.9 Enhancing the electromechanical response using the concept of electrets

As discussed in Section 1.2.1, depositing permanent electrical charges on the interface of bilayers and forming electrets is an effective way to enhance the apparent flexoelectric response (Wen *et al.*, 2019). In this section, we test this idea in our setup. The boundary conditions and the setup are the same as Section 3.1 except on the interface on which we introduce a surface charge density of $\{0, 0.25\}[C/m^2]$. Closed circuit boundary condition is considered. The boundary conditions are shown in Fig. 3.18. We consider $h_f = 1\mu m$ and $(h_s + h_f)/h_f = 40$, and $L = 160\mu m$. The material properties are chosen such that the wrinkle pattern is obtained.

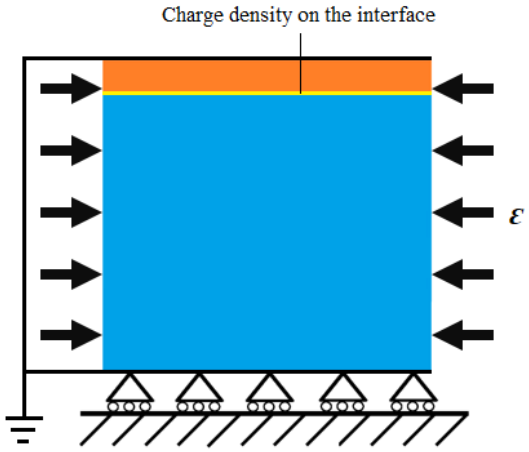

Figure 3.18: Boundary conditions for the bilayer with a layer of electrical charges on the interface.

The following material properties have been considered for the film:

$$G_f = 575MPa, \quad \epsilon = 9.2nJ/V^2m, \quad \mu_L = \{0, 100\}nJ/Vm, \quad \mu_T = \{0, 50\}nJ/Vm, \quad \ell_2 = 0.5\mu m, \quad \mu_S = \ell_1 = 0, \tag{3.14}$$

G_f being the shear modulus of the film.

For the substrate, the following material parameters are considered:

$$G_s = 9.583MPa, \quad \epsilon = 9.2nJ/V^2m, \quad \ell_2 = 0.1\mu m, \quad \mu_L = \mu_T = \mu_S = \ell_1 = 0. \tag{3.15}$$

G_s being the shear modulus of the substrate. No prestretch in the substrate has been considered ($\lambda_0 = 1$).

As can be seen in Fig. 3.19, the introduction of permanent electrical charges on the interface significantly improves the electric response of this system. This idea therefore can be very useful in improving the electromechanical performance of potential devices.

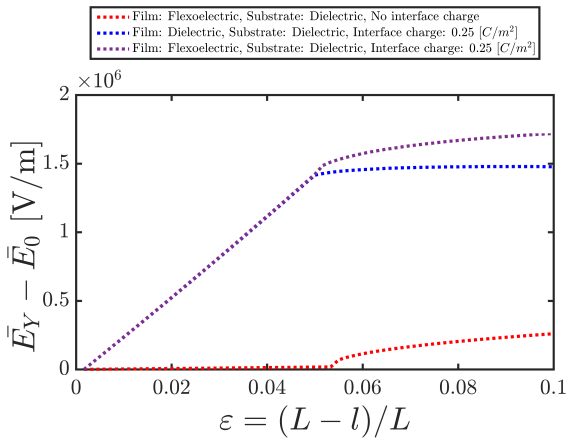

Figure 3.19: Net vertical electric field generated on a wrinkle peak minus the initial vertical electric field as a function of overall compressive strain ε: Effect of charge density on the interface.

3.9.1 Electret with no flexoelectricity: Effect of l_2 on the net vertical electric field generated on a wrinkle peak.

One important question from the last example is in electrets, how sensitive are the results of the electric response to l_2? To shed light on this issue, for this example, we neglect flexoelectricity in the film. The charge density on the interface is equal to 0.5 $[C/m^2]$.

The following material properties have been considered for the film:

$$G_f = 575MPa, \quad \epsilon = 9.2nJ/V^2m, \quad \ell_2\text{film} = 0.5\mu m, \quad \mu_L = \mu_T = \mu_S = \ell_1 = 0, \tag{3.16}$$

G_f being the shear modulus of the film.

For the substrate, a set of material parameters are considered:

$$G_s = 5.75MPa, \quad \epsilon = 9.2nJ/V^2m, \quad \ell_2\text{substrate} = \{0, 0.1, 0.4, 1.6\}\mu m, \quad \mu_L = \mu_T = \mu_S = \ell_1 = 0, \tag{3.17}$$

G_s being the shear modulus of the substrate. No prestretch in the substrate has been considered ($\lambda_0 = 1$). Fig. 3.20 shows that in electrets, the electric field generated on a wrinkle peak is highly sensitive to the ratio between l_2 of the film and the substrate. From this figure, one may conclude that in electrets, this ratio needs to be as low as possible, since the response obtained from the higher ratios does not seem to be physical. Note that, for electret without flexoelectricity, there is no need to solve the high-order electric problems. Therefore one could set the l_2 of the film and the substrate to be equal to zero.

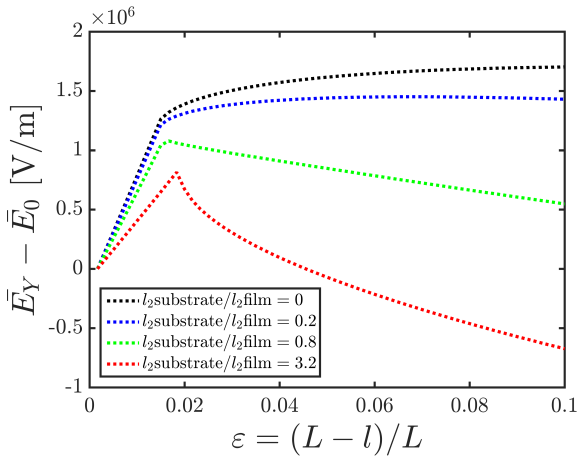

Figure 3.20: Effect of l_2 ratio on the net vertical electric field generated on a wrinkle peak.

3.10 Ongoing and future work

3.10.1 Phase diagrams in electromechanical bilayers

As shown in this chapter, the well-known mechanical surface instabilities can be captured with our model. This means that this computational model can be used as an infrastructure for constructing phase diagrams in electromechanical bilayers. One interesting avenue for further investigation is to explore how the combination of electrical and mechanical loadings can change the phase diagrams. Also, it is important to know how flexoelectricity may affect the phase diagrams. Also, constructing phase diagrams in dielectric/dielectric bilayers with a layer of electrical charges on the interface may be interesting, since electrets have been shown to be an effective way to enhance the flexoelectric-like response of the system (Wen *et al.*, 2019).

As the first step towards this goal, let us take one step back and construct a phase diagram for the elastic/elastic film/substrate system. To construct this phase diagram, we followed a similar approach as (Wang and Zhao, 2015). Fig. 3.21 shows the phase diagram of a perfectly bound elastic/elastic bilayer by changing the modulus ratio and strain mismatch. This phase diagram is similar to the results of (Wang and Zhao, 2015) (Fig. 1.6).

Now, let us study a dielectric-dielectric bilayer having surface charges on the interface. In this section, the following material properties have been considered for the film:

$$G_f = 575MPa, \qquad \epsilon = 9.2nJ/V^2m, \qquad \mu_L = \mu_T = \mu_S = \ell_1 = \ell_2 = 0, \tag{3.18}$$

G_f being the shear modulus of the film.

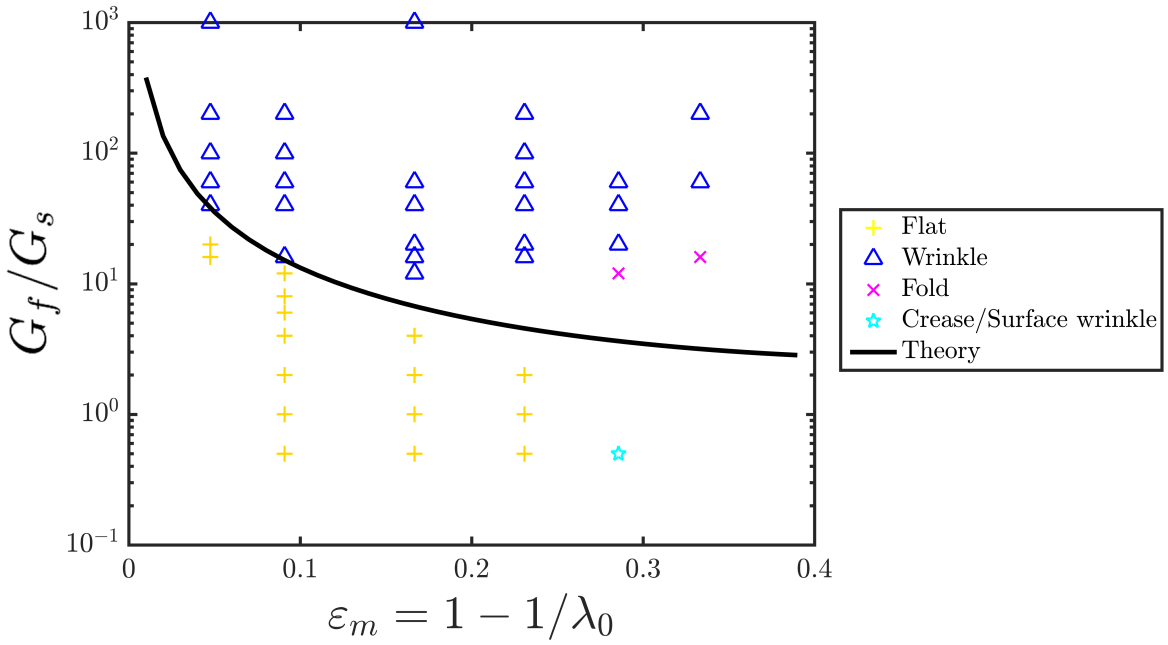

Figure 3.21: Phase diagram of elastic-elastic film/substrate system.

For the substrate, a set of material parameters are considered as:

$$G_s = 0.575 - 575MPa, \qquad \epsilon = 9.2nJ/V^2m, \qquad \mu_L = \mu_T = \mu_S = \ell_1 = \ell_2 = 0, \tag{3.19}$$

G_s being the shear modulus of the substrate. No substrate prestretch ($\lambda_0 = 1$) has been considered. The X displacement on the vertical surfaces of the system and the Y displacement on the lower surface of the substrate are set to zero. The upper surface of the film and the lower surface of the substrate have been grounded. We increase the surface charge on the interface. The boundary conditions are shown in Fig. 3.18. Neglecting the possibility of electric breakdown, the system starts to wrinkle at a critical charge density. Fig. 3.22 shows an example of electrically induced wrinkles in a system with a modulus ratio of 200.

The onset of wrinkling is shown in Fig. 3.23. This figure shows that increasing the modulus ratio results in a decrease in the interface's critical wrinkling charge density. So, considering charge density or the initial electric field across film thickness adds a third dimension to the phase diagrams. It may be interesting to construct a 3D phase diagram with modulus ratio, strain mismatch, and interface charge density, to understand how instability patterns change in electrets. Another question that requires further study is what parameters determine the wavelength of the wrinkles in the electrically-induced instability. To explore this, analytical approaches can complement our simulations.

Beyond the setup studied here, it would also be interesting to understand the effect of

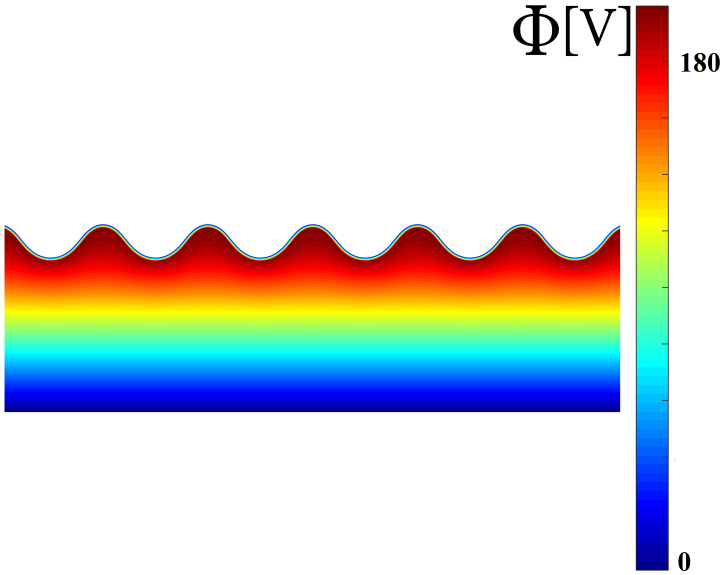

Figure 3.22: A sample of electrically induced wrinkles in a system with a modulus ratio of 200. The colormap shows the distribution of electric potential [V].

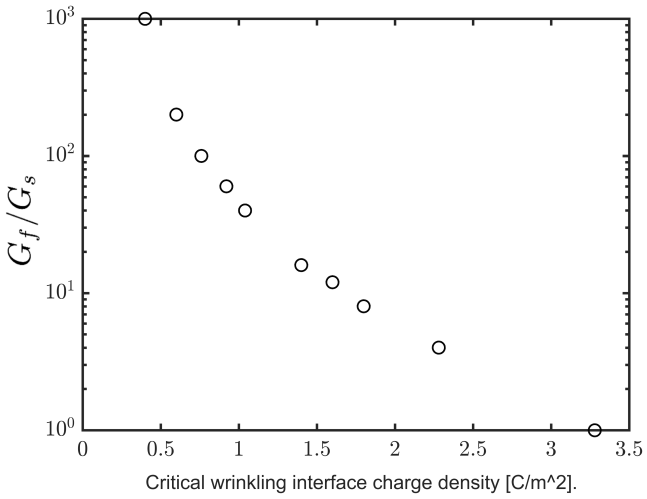

Figure 3.23: Onset of wrinkling in electrets.

the interface conditions, including delamination. Of particular interest are the high-order conditions, which similarly to the free boundary high-order conditions, still lack a clear physical interpretation.

3.11 Concluding remarks

In this chapter, studying the effect of modulus ratio and the substrate prestretch, we captured the well-known mechanical instability patterns of wrinkle, period-double, ridge, fold, and crease in a flexoelectric/dielectric bilayer. We explored the transition between the instability patterns and investigated the flexoelectricity-induced electrical response of each family of instability patterns. The present exploration has allowed us to understand the effect of material parameters. As shown, no effect of flexoelectricity on the onset of wrinkling and folding instabilities is apparent in the present settings. In principle, no direct bulk flexoelectric effect would be expected in the uniform deformation state studied here. Nevertheless, as explained in detail in Section 2.2, boundary layers in the vertical electric field and in the vertical strain components develop under homogeneous macroscopic deformations as a result of surface-induced symmetry breaking and surface relaxation. These boundary and interface layers manifest here in the emergence of a linear electric response upon uniform horizontal compression of the film/substrate system before buckling. These flexoelectric responses however do not seem to significantly affect the critical wrinkling and folding strains in the present simulations. Further exploration with enhanced flexoelectric properties would be necessary to reveal these effects before the onset of the surface instabilities. At the onset of instabilities, large strain gradients develop within the film that causes the observed flexoelectric response. These large strain gradients penetrate well into the substrate, which is assumed here to be a non flexoelectric dielectric. The overall electric response would be significantly enhanced in a flexoelectric film on a flexoelectric substrate system. The observations and insights obtained from these exploratory studies motivate the proof-of-concept devices proposed in the next chapter.

Chapter 4

Towards flexoelectric-based electromechanical devices

In this section, in light of the insights gained from the exploration presented in Chapter 3, we propose here several device concepts exploiting surface instabilities patterns and the flexoelectric effect.

4.1 Electrically activated pattern change in dielectrics

In Sections 3.4-3.7, we studied the instability patterns in a thin flexoelectric film on a dielectric substrate prestretched incompressible system in closed circuit. Depending on the elastic moduli ratio between the film and the substrate, and the level of prestretch, we have identified the critical horizontal compressive strain for the different instability patterns. We have shown that, for the parameter range under consideration, these critical loads are not significantly affected by flexoelectricity in these settings, see discussion in Section 3.11. Once instability occurs, however, flexoelectricity is the driving mechanism for the overall electric response as shown in Section 3.8.3. In particular, depending on the combination of the three independent parameters in the cubic flexoelectric tensor, the sign of the net electric field at the wrinkle peak can be reversed. Some of the observed patterns in the previous section present a clear up-down symmetry. Intuitively, an external bias could then favor some patterns over others, thus providing a means to control surface instabilities pattern formation. We explore this concept next. The setup considered in this example is similar to Section 3.1, except for the electrical boundary conditions and the specimen size. We consider $h_f = 100\text{nm}$ and $(h_f + h_s)/h_f = 40$. The loading and boundary conditions are depicted in Fig. 4.1. The bottom of the substrate and the interface are grounded. Also, from the start to the end of mechanical loading, the top of the film is grounded. However, once the mechanical loading is finished, we incrementally apply a voltage to the top of the film. The other faces are considered to be charge free. The material properties are chosen such that a mechanically bi-stable state exists (see section 3.4).

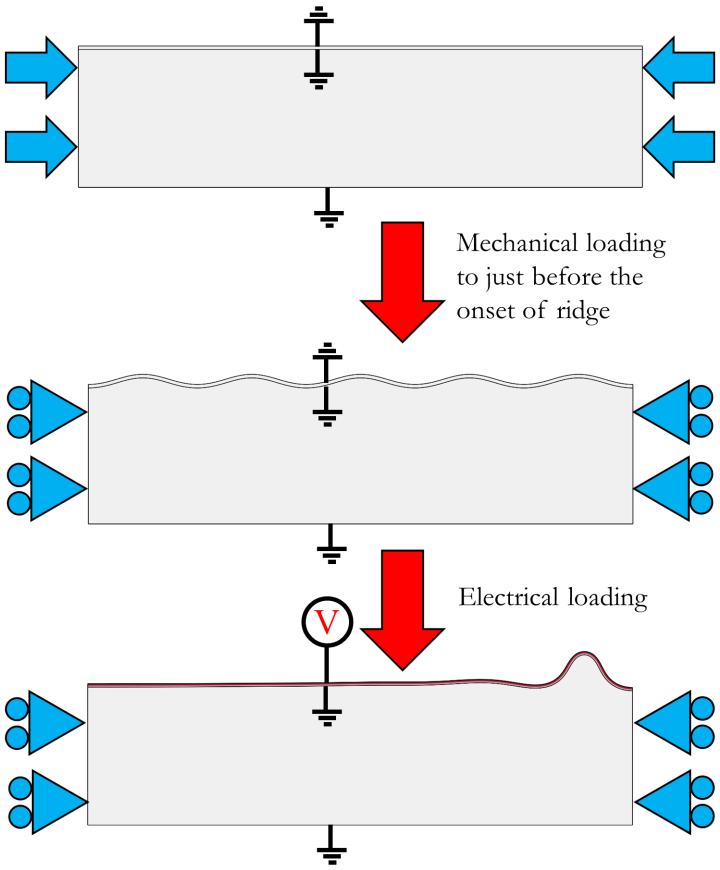

Figure 4.1: Schematic of the loading procedure.

The material considered for film in this example is PVDF for which the following material properties are considered:

$$G_f = 575\text{MPa}, \quad \epsilon = 0.1151\text{nJ/V}^2\text{m}, \quad \mu_{\text{L}} = 2\mu_{\text{T}} = 4\mu_{\text{S}} = 2.3\text{nJ/Vm}, \quad \ell_2 = 50\text{nm}, \quad \ell_1 = 0. \tag{4.1}$$

Note that although PVDF is piezoelectric, its piezoelectricity has been neglected. For the substrate, we consider PDMS with the following material properties:

$$G_s = 0.575\text{MPa}, \quad \epsilon = 0.028067\text{nJ/V}^2\text{m}, \quad \ell_2 = 0.5\mu\text{m}, \quad \mu_{\text{L}} = \mu_{\text{T}} = \mu_{\text{S}} = \ell_1 = 0, \tag{4.2}$$

$\lambda_0 = 2$ is considered. The mesh size is similar to Section 3.4. We mechanically load the system to overall compressive strain $\varepsilon = 0.0293$, just before the onset of the ridge instability pattern.

It is worthwhile noting that the mechanical deformation seen in this example (not shown) was similar to Fig. 3.7a. This is because this figure is mainly governed by modulus ratio and substrate prestretch when the flexoelectric length scale is much smaller than the film thickness. This means that flexoelectricity cannot affect deformations unless the flexoelectricity length scale is comparable to the specimen size. After finishing the mechanical loading, we start incrementally applying a voltage on the thin film. Both positive and negative voltages are considered. At a critical electric field, the wrinkle instability pattern becomes unstable and the ridge state appears as the only stable state in the system (Fig. 4.2). This transition which is mainly due to electrostriction is not reversible, i.e. we cannot go back to the wrinkle state by decreasing the applied voltage. Our simulation shows that there is a slight asymmetry (< 3%) in the critical transition electric field. This asymmetry is due to flexoelectricity because the flexoelectricity-induced electric field can accommodate or act against the transition depending on the sign of the external bias. Also, we observe a very slight asymmetry in the normalized vertical displacement of the ridge peak (< 0.2%) due to the application of positive and negative bias.

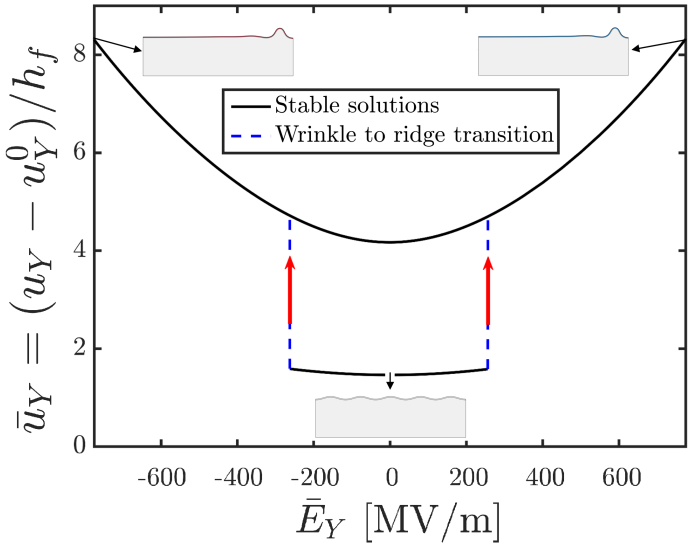

Figure 4.2: Electrically activated wrinkle to ridge transition. u_Y^0 has been computed from the maximum mechanical strain applied ($\varepsilon = 0.0293$).

To better reveal the role of flexoelectricity, we simulate the same system with softer materials (reducing the shear moduli of the film and the substrate by a factor of 10). This way the relative importance of flexoelectricity is increased without the need to use larger flexoelectric coefficients, thus revealing its role more clearly. In this example, we mechanically load the system to overall compressive strain $\varepsilon = 0.028$, just before the onset of the ridge

instability pattern. It is worth noting that, similarly to the previous example, up to the end of the mechanical loading, the mechanical deformation seen in this example is similar to Fig. 3.7a, however, the wrinkle-to-ridge transition happens slightly sooner than in Fig. 3.7a. From this point, we electrically load the bilayer, similar to the previous example. Fig. 4.3 shows the results for this case. Compared to the previous example, there is a bigger asymmetry (< 6%) in the critical transition electric field as well as an asymmetry in the normalized vertical displacement of the ridge peak (< 0.5%) due to the application of positive and negative bias.

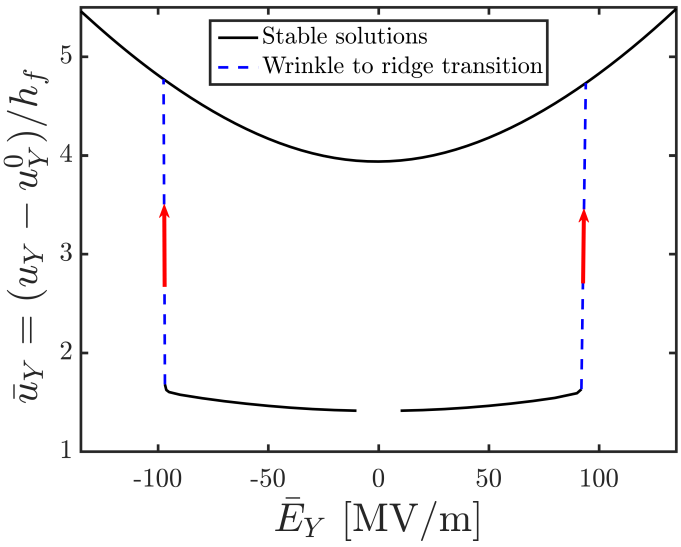

Figure 4.3: Electrically activated wrinkle to ridge transition for a soft bilayer. u_Y^0 has been computed from the maximum mechanical strain applied (ε = 0.028).

4.2 Lateral compression sensor

As shown in Fig. 3.5, the absolute value of electric potential on wrinkled peak increases with the increase of overall compressive strain. Therefore, in this system, there is an overall potential difference between the outermost part of the wrinkle (wrinkle peak) and the bottom of the substrate. Here, we propose a novel design for an effectively piezoelectric lateral compression sensor, made from non-piezoelectric materials, that allows us to collect this flexoelectrically-generated potential difference, see Fig. 4.4, thus showing an effective h_{31} piezoelectric property, which is often used in energy harvesting applications (Priya *et al.*, 2008). h_{31} is the slope of the generated lateral electric field due to axial strain (Ikeda, 1996). Such a device presents some advantages over other proposed flexoelectricity-exploiting devices, see Section 1.2, such as easy fabrication of large-area apparent piezoelectrics. Such a device would be particularly useful for flexophotovoltaic applications (Yang *et al.*, 2018). So, we consider a similar system to Fig.

3.5 with the same boundary conditions and we study the effect of electric permittivity in the substrate. We consider $h_f = 100\text{nm}$ and $(h_f + h_s)/h_f = 40$. We account also for flexoelectricity in the substrate since we expect large gradients to develop in the substrate as well, see Fig. 3.5, and thus the flexoelectric response of the substrate should significantly contribute to the overall electric response.

The material considered for the film in this example is PVDF with the following material properties:

$$G_f = 575\text{MPa}, \quad \epsilon = 0.1151\text{nJ/V}^2\text{m}, \quad \mu_\text{L} = 2\mu_\text{T} = 4\mu_\text{S} = 2.3\text{nJ/Vm}, \quad \ell_2 = 50\text{nm}, \quad \ell_1 = 0. \tag{4.3}$$

We consider a substrate with the following material properties:

$$\begin{aligned} &G_s = 718.75\text{kPa}, \quad \epsilon = \epsilon_s^r \epsilon_0 = 0.028067\text{nJ/V}^2\text{m}, \quad \mu_\text{L} = 2\mu_\text{T} = 4\mu_\text{S} = f(\epsilon - \epsilon_0)\text{nJ/Vm}, \\ &\ell_2 = 0.5\mu\text{m}, \qquad\qquad \ell_1 = 0, \end{aligned} \tag{4.4}$$

where $\epsilon_0 = 8.854 \times 10^{-12} JV^2/m$ is the vacuum permittivity, and f is the flexocoupling coefficient. No prestretch is considered ($\lambda_0 = 1$). Fig 4.5 shows the electric potential of a wrinkle peak, as a function of applied compressive strain, for two different flexocoupling values. A large contribution of substrate flexoelectricity becomes apparent. Also, from this figure, it is clear that increasing electric permittivity of the substrate improves the rate of the increase of the absolute value of the electric potential, at constant flexocoupling. In the range of compressive strains $[0.02 - 0.05]$ where the increase of the potential is almost linear, considering thickness of the specimen being $h_f + h_s = 4\mu\text{m}$, we can obtain $h_{31} = -[\Phi^t_{film}(0.05) - \Phi^t_{film}(0.02)]/[(0.05 - 0.02) \times 4 \times 10^{-6}]$. For the yellow curve, we obtain $h_{31} = 0.014GV/m$. To compute the g piezoelectric coefficient , which relates the resulting potential difference to applied force (Ikeda, 1996), the

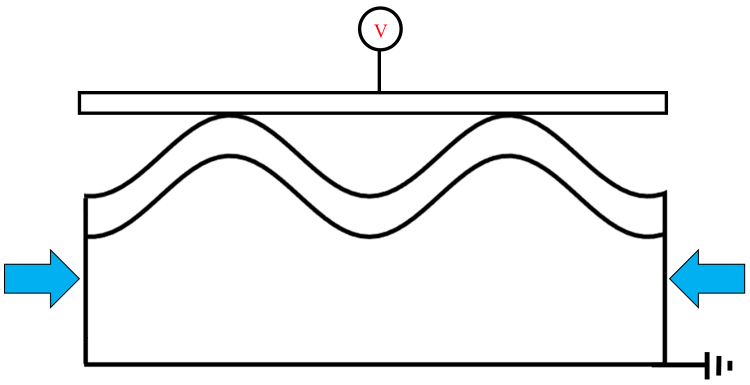

Figure 4.4: Lateral compression sensor.

effective stiffness of the system is required. Neglecting the stiffening effects of flexoelectricity, we can approximately compute the effective elasticity modulus of the composite in its ground state by $E_{eff} = (E_f h_f + E_s h_s)/(h_f + h_s)$, where E_f and E_s are the elasticity modulus of film and substrate. Note that the effective stiffness computed with this approach in this system may be on the conservative side since after wrinkling the system is more compliant than the ground state. With this, we obtain $g_{31} = h_{31}/E_{eff} = 309.2\text{mV}\,m/N$. This is already comparable to PVDF ($g_{33} = -339\text{mV}\,m/N$).

The performance of this system can be optimized by changing the modulus ratio, substrate prestretch, as well as the electrical properties of the substrate. Besides, using the concept of electrets and introducing electric charges on the interface should significantly enhance the performance of the mentioned device.

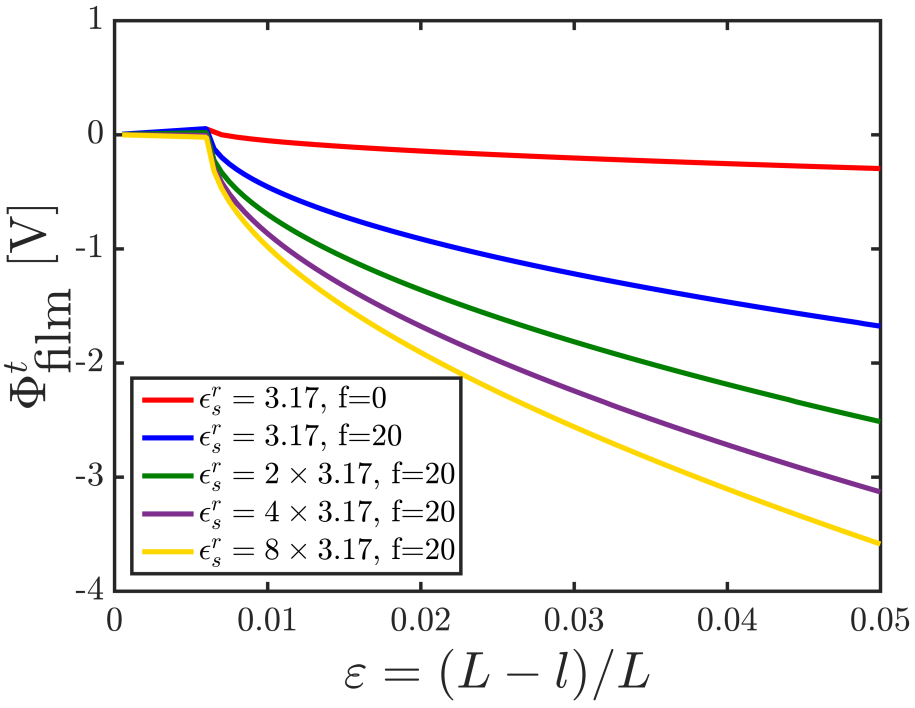

Figure 4.5: Effect of dielectric permittivity of the substrate.

4.3 Conceptual design of flexoelectric-based self-powered supercapacitive pressure sensors

Being a property of all dielectric materials, flexoelectricity opens new doors for the design of biocompatible (non-toxic) smart electromechanical devices. One of the exciting relevant

lines of research has been to develop flexible electronic skin (e-skin). The capacity to perceive and differentiate between multiple spatiotemporal tactile stimuli, such as static and dynamic pressure, temperature, and vibration, is a crucial requirement for using the e-skins for human skin-like tactile sensor applications. Recently, significant progress has been made in the design of multifunctional e-skins (Chortos *et al.*, 2016, Hammock *et al.*, 2013, Ji *et al.*, 2019, Park *et al.*, 2015, Qiu *et al.*, 2018, Sun *et al.*, 2014, Yang *et al.*, 2019c). As an important part of e-skins, various researchers have focused on the development of soft pressure and tactile sensors (Amoli *et al.*, 2020, Chen *et al.*, 2014, Cho *et al.*, 2017, Joo *et al.*, 2015, Li *et al.*, 2016, Mannsfeld *et al.*, 2010, Nie *et al.*, 2015, Peng *et al.*, 2020, Ruth *et al.*, 2020, Wang *et al.*, 2019b, Yang *et al.*, 2019a,b, Yin *et al.*, 2019, Zou *et al.*, 2020a,b). Ridges (Zou *et al.*, 2020b), pyramids (Cho *et al.*, 2017), pillars (Yang *et al.*, 2019a), domes (Park *et al.*, 2015), wrinkles (Chen *et al.*, 2014), etc. have been proposed to increase the sensitivity of the pressure sensors. In this section, informed by diverse literature on tactile and pressure sensors, we seek to conceptually design a flexoelectric-based pressure sensor.

The surface instabilities in bilayers result in a local symmetry breaking in the system. If the film is flexoelectric, the local symmetry breaking causes a local charge separation. The local vertical electric fields on different points of the film can be a meaningful indicator of this. However, one important question is how to effectively extract the generated electrical response to design a flexoelectric-based pressure sensor. In the previous section, we provided a design concept for a lateral compression sensor, with h_{31} and g_{31} apparent piezoelectric properties. Here, we restrict ourselves to capacitive or supercapacitive sensing mechanisms. In the capacitive sensing mechanism, the capacitance of the sensor changes due to external stimuli. This results in the generation of an electric signal. The capacitance of a parallel plate capacitor can be computed by a simple formula $C = \epsilon A/d$, where ϵ is the permittivity of the material between the two plates, A is the area of the smallest of the two plates, and d is the distance between two plates. Therefore, by changing the distance between the two plates of the capacitor, as well as the effective area of the capacitor, one can change its capacitance.

With this background, let us now explain the conceptual design of a pressure sensor. This design is partially informed by several research papers in the literature and in particular (Sun *et al.*, 2014, Zhang *et al.*, 2020b). The conceptual design of this system is shown in Fig. 4.6. The first step is to build a properly patterned bilayer. This can be done by stretching the substrate, bonding the thin dielectric film on the substrate, and releasing it. Wrinkles may form in this system. The top of the film needs to be grounded, therefore, using a deformable electrode such as ionic conductors (Keplinger *et al.*, 2013) on top of the film and connecting it to the ground can be an effective way of grounding the top of the dielectric film. Due to flexoelectricity, charge separation takes place on the wrinkle peaks and valleys. In other words, mechanical deformation results in charge separation in the vertical direction on the wrinkled film. Therefore, on the peaks and valleys, charges of the different signs will concentrate. Now, one can place another conductor on top of this system and connect it to the ground. On the interface between the ionic conductor and the other conductor, electric double layers (EDL)

will form, i.e. charges of opposite signs on the two electrodes will be attracted to each other. Since the distance between the charges is on the nanometer scale, the EDL is equivalent to a capacitor of very high capacitance, i.e. supercapacitor. Now, applying a force on the surface of the conductor, the capacitance of the EDL will change due to a change in the distance and the effective area of the two plates of the EDL. This results in an electrical signal.

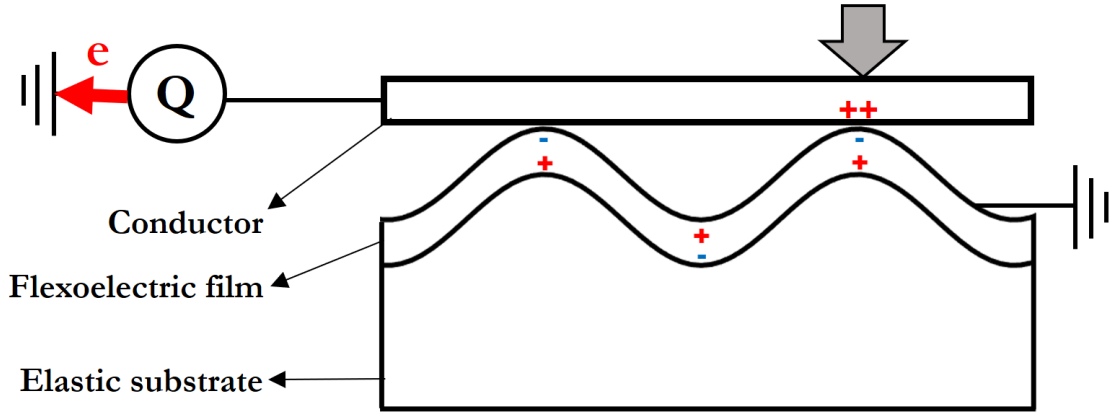

Figure 4.6: Conceptual design of flexoelectric-based self-powered supercapacitive pressure sensor.

It is worthwhile to note that without flexoelectricity, this system could also work if a small external voltage is applied to form the EDLs. Therefore, the contribution of flexoelectricity here is to make this system self-powered. This system can also be regarded as an energy harvester. It is important to note that although we explained this design for wrinkles, other instability patterns can also be employed in the design and they may have advantages over wrinkles.

4.4 Conclusion

In this chapter, we explored three potential applications for instability-based devices. We first studied the possibility of electrically activating the pattern change in dielectric bilayers commenting on the role of flexoelectricity to cause an asymmetrical response with positive and negative external bias. We then presented the design of a lateral compression sensor and a pressure sensor.

Chapter 5

Effect of flexoelectricity on stress singularities

On a crack tip, sharp notch, fold, crease, etc. stress singularities exist which provide the largest local strain gradients. In this chapter, we focus on the manifestations of flexoelectricity in stress singularities, and in particular, we will show that flexoelectricity can result in a delay in the formation of folds in bilayers. Furthermore, we will explore the notch strengthening effect and flaw-insensitive fracture and will show that flexoelectricity can contribute to these phenomena.

5.1 Effect of flexoelectricity on the formation of folds in bilayers

This section has been devoted to studying the effect of flexoelectricity and strain gradient elasticity on the fold instability in a flexoelectric/dielectric bilayer. First, we study the effect of flexoelectric coefficients as well as the strain gradient elasticity length scale l_1 on the local electromechanical response. Then we show that flexoelectricity may result in a delayed fold formation in flexoelectric/dielectric bilayers.

In all the examples provided in this section, the setup and boundary conditions are the same as those in Section 3.1. Closed circuit boundary condition is considered. The material properties and the prestretch in the substrate have been chosen such that folding develops.

5.1.1 Effect of film flexoelectric coefficients on the mean vertical electric field generated on a fold tip

The effect of film flexoelectricity coefficients on the net vertical electric field on a fold tip is studied. We consider $h_f = 1\mu m$, $(h_s + h_f)/h_f = 40$, and $L = 60\mu$m. The number of finest elements of the film (elements to discretize displacement and electric potential fields) is considered to be

$\{96, 8\}$ for width and thickness, respectively, while that of the substrate is $\{96, 64\}$, for width and thickness, respectively. The following material properties have been considered for the film:

$$G_f = 575MPa, \quad \epsilon = 9.2nJ/V^2m, \quad \mu_{\mathrm{L}} = \{0, 100\}nJ/Vm, \quad \mu_{\mathrm{T}} = \{0, 50, 100\}nJ/Vm,$$
$$\mu_{\mathrm{S}} = \{0, 100\}, \quad \ell_2 = 0.5\mu m, \quad \ell_1 = 0, \tag{5.1}$$

G_f being the shear modulus of the film.

For the substrate, the material parameters are:

$$G_s = 47.917MPa, \quad \epsilon = 9.2nJ/V^2m, \quad \ell_2 = 1\mu m, \quad \mu_{\mathrm{L}} = \mu_{\mathrm{T}} = \mu_{\mathrm{S}} = \ell_1 = 0, \tag{5.2}$$

G_s being the shear modulus of the substrate. A substrate prestretch $\lambda_0 = 1.4$ has been considered.

Fig. 5.1 shows the net vertical electric field on a fold tip for different combinations of flexoelectric coefficients, as lateral compression increases and through the flat/wrinkle and wrinkle/fold transitions. It can be seen in Fig. 5.1a that μ_{L} and μ_{T} result in the generation of electric field of opposite sign in wrinkling state, but not in the fold state. Besides, μ_{S} does not generate a noticeable $\bar{E}_Y$ in the flat state, while it causes the generation of the $\bar{E}_Y$ of the opposite sign compared to μ_{T} in the wrinkle and fold states. It is worthwhile to note that in all the examples shown in this section, the deformation field did not considerably change with the change of the flexoelectric coefficients (see Fig. 5.2 for example). Therefore, for the chosen material properties, the coupling is inclined to be one-way. To better understand the reasons behind these trends, one can plot the components of strain gradient in the different states bearing in mind that $\widetilde{\mathfrak{E}}_{XXY}$ is coupled with E_Y through μ_{T}, $\widetilde{\mathfrak{E}}_{YYY}$ is coupled with E_Y through μ_{L}, and $\widetilde{\mathfrak{E}}_{XYX}$ and $\widetilde{\mathfrak{E}}_{YXX}$ are coupled with E_Y through μ_{S} (Fig. 5.3). As an example, it can be seen that the difference in the component $\widetilde{\mathfrak{E}}_{XXY}$ between fold and wrinkle states (slope of strain gradient - overall compression) at the fold tip position is negative, similar to that of $\widetilde{\mathfrak{E}}_{YYY}$. However, in the wrinkling state, the slope of strain gradient - overall compression curve (not shown) is positive for $\widetilde{\mathfrak{E}}_{YYY}$, and negative for $\widetilde{\mathfrak{E}}_{XXY}$. These types of arguments (reducing the complexity of the model and focusing on the most relevant features) can be very useful to interpret the results of complex simulations with multiple cross effects.

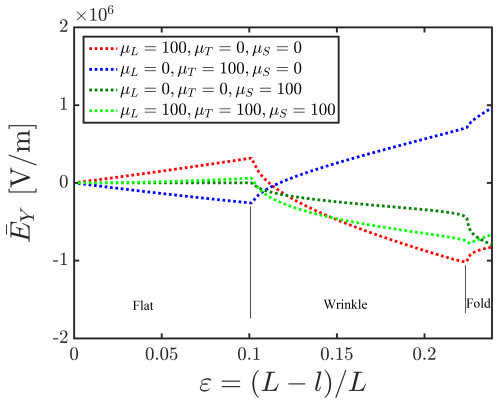

(a) Effect of film flexoelectric coefficients on the net electric field.

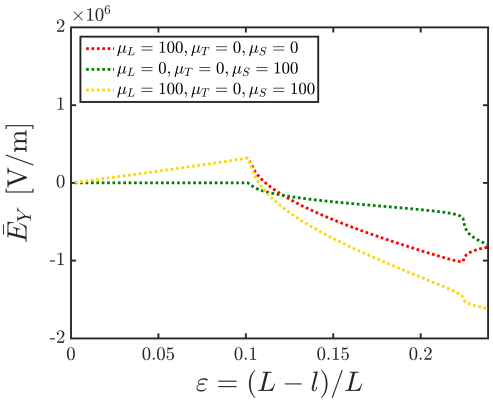

(b) Effect of film flexoelectric coefficients on the net electric field.

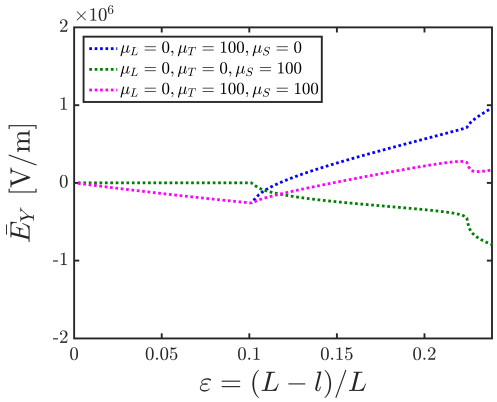

(c) Effect of film flexoelectric coefficients on the net electric field.

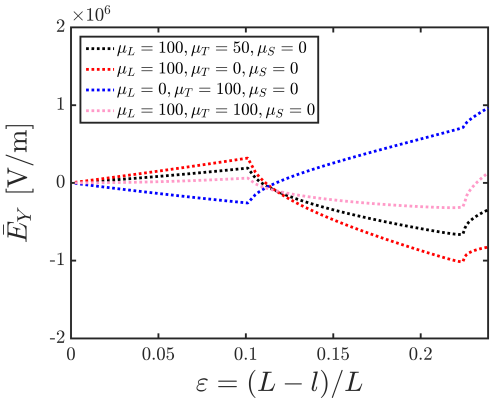

(d) Effect of film flexoelectric coefficients on the net electric field.

Figure 5.1: Folding in a flexoelectric/dielectric film/substrate system. Effect of film flexoelectric coefficients on the net vertical electric field generated on a wrinkle valley (fold tip). For visualization purposes, the plots have been separated into 4 figures for easier comparison.

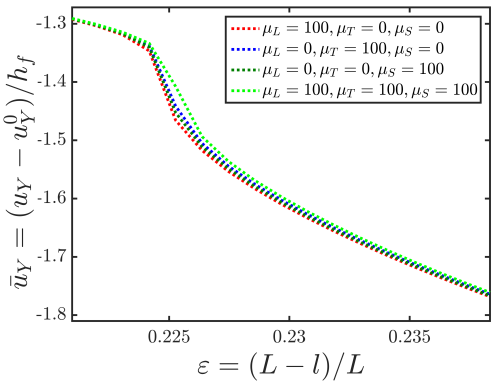

Figure 5.2: Normalized relative displacement of the fold tip (wrinkle valley) around the wrinkle-to-fold transition strain for different flexoelectric coefficients.

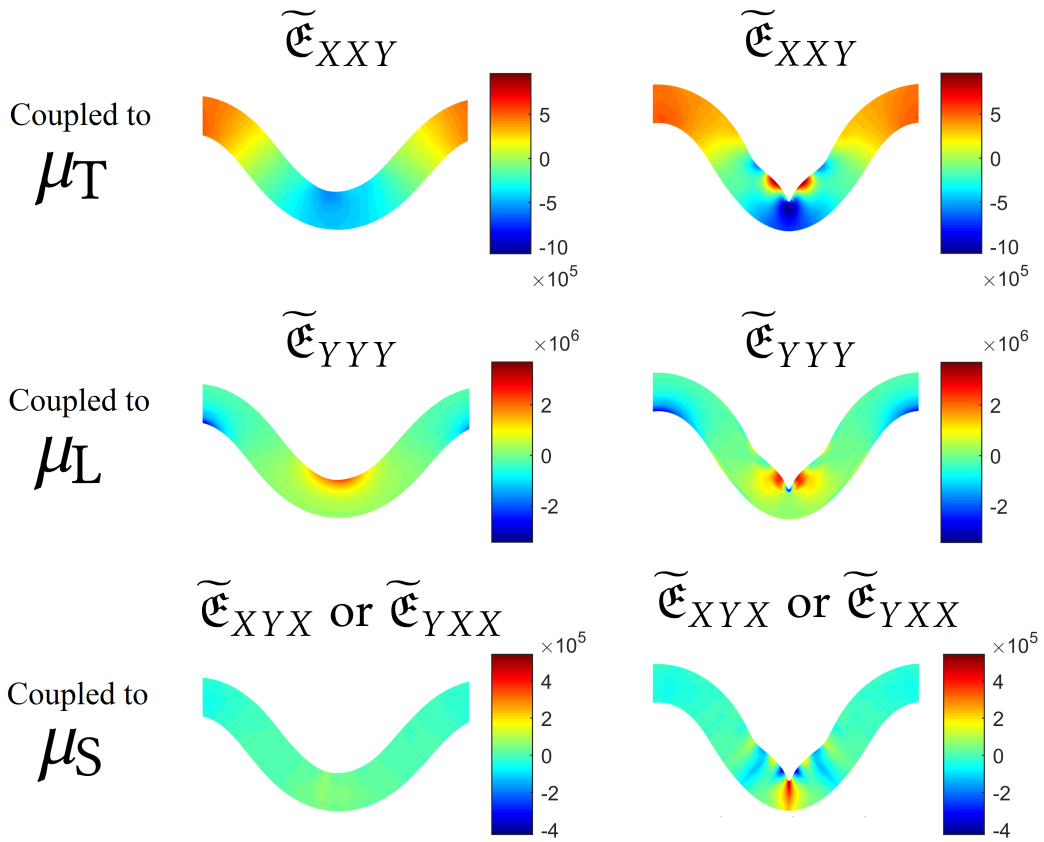

Figure 5.3: Relevant strain gradient components before (left) and after (right) the wrinkle/fold transition.

5.1.2 Effect of film l_1 on the generated mean vertical electric field and fold formation

We study the effect of film's strain gradient elasticity length scale, l_1, on the electromechanical response of a flexoelectric/dielectric bilayer undergoing folding. We consider $h_f = 1\mu m$, $(h_s + h_f)/h_f = 40$, and $L = 60\mu m$. The number of finest elements of the film (elements to discretize displacement and electric potential fields) is considered to be $\{96, 8\}$ for width and thickness, respectively, while that of the substrate is $\{96, 64\}$. In this section, the following material properties have been considered for the film:

$$\begin{aligned} &G_f = 575MPa, \quad \epsilon = 9.2nJ/V^2m, \quad \mu_{\mathrm{L}} = 100nJ/Vm, \quad \mu_{\mathrm{T}} = 50nJ/Vm, \\ &\ell_2 = 0.5\mu m, \quad \ell_1 = \{0, 0.125, 0.25, 0.5\}\mu m, \quad \mu_{\mathrm{S}} = 0, \end{aligned} \tag{5.3}$$

G_f being the shear modulus of the film.

For the substrate, the following material parameters are considered:

$$G_s = 47.917MPa, \quad \epsilon = 9.2nJ/V^2m, \quad \ell_2 = 1\mu m, \quad \mu_{\mathrm{L}} = \mu_{\mathrm{T}} = \mu_{\mathrm{S}} = \ell_1 = 0, \tag{5.4}$$

G_s being the shear modulus of the substrate. A substrate prestretch $\lambda_0 = 1.4$ has been considered.

Figure 5.4a shows the normalized relative vertical displacement, $\bar{u}_Y$, as a function of overall compressive strain. From this figure, it can be seen that increasing film l_1 can significantly delay the formation of folds in the bilayers. The resulting net vertical electric field on a wrinkle valley (fold tip) has been depicted in Fig. 5.4b. From this figure, it is important to note that l_1 does not noticeably change the electrical response of the system unless through a change in the deformation of the system.

Overall, we showed that the strain gradient elasticity length scale l_1 can contribute to delaying the formation of the folds. Therefore, a natural question to ask is whether other gradient effects e.g. flexoelectricity can contribute to this phenomenon as well. In the next section, we will try to answer this question.

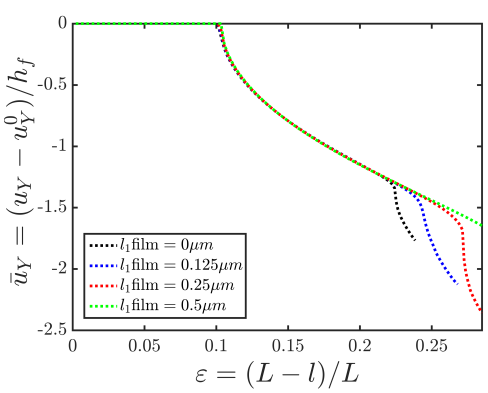

(a) Normalized relative vertical displacement, $\bar{u}_Y$, of the wrinkle valley (fold tip) for different values of the film's strain gradient elasticity length scale, ℓ_1.

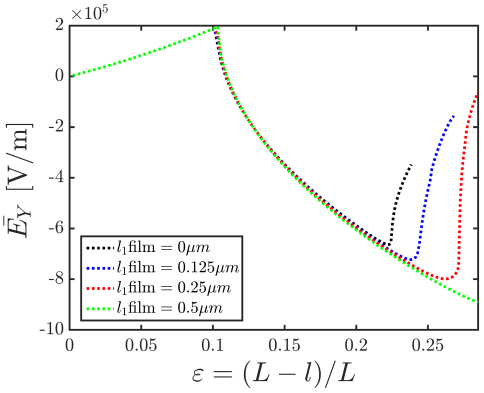

(b) Net vertical electric field at the wrinkle valley (fold tip) for different values of the film's strain gradient elasticity length scale, ℓ_1.

Figure 5.4: Folding in a flexoelectric/dielectric film/substrate system. Effect of film l_1.

5.1.3 Delayed fold formation due to strain gradient elasticity and flexoelectricity

We have shown that strain gradient elasticity can delay the formation of folds in bilayers. In this section, we try to better explore this effect. In all the examples in this section, we consider $h_f = 1\mu m$ and $(h_s + h_f)/h_f = 20$, and $L = 60\mu m$. The number of finest elements of the film (elements to discretize displacement and electric potential fields) is considered to be $\{96, 8\}$ for width and thickness, respectively, while that of the substrate is $\{96, 32\}$, for width and thickness, respectively. In this section, let us consider a more compliant film/substrate system compared to what we considered in previous examples. This is because higher compliance induces higher strains and strain gradients, and thus larger electric response for a given flexoelectric tensor. The following material properties have been considered for the film:

$$\begin{aligned} &G_f = 19.17MPa, && \epsilon = 9.2nJ/V^2m, && \mu_L = \{0, 100\}nJ/Vm, \\ &\mu_T = \{-100, 0, 100, 300\}nJ/Vm, && \mu_S = \{-100, 0, 100\}, && \ell_2 = 0.5\mu m, \\ &\ell_1 = \{0, 0.125\}\mu m, \end{aligned} \tag{5.5}$$

G_f being the shear modulus of the film.

For the substrate, the following material parameters are considered:

$$G_s = 1.60MPa, \qquad \epsilon = 9.2nJ/V^2m, \qquad \ell_2 = 1\mu m, \qquad \mu_L = \mu_T = \mu_S = \ell_1 = 0, \tag{5.6}$$

G_s being the shear modulus of the substrate. A substrate prestretch $\lambda_0 = 1.4$ has been considered. Note that although we are considering a relatively low-stiffness system, we are still far from very soft materials, so the elastocapillarity effects do not play a relevant role (Wang and Zhao,

2013).

Figure 5.5a shows the normalized relative vertical displacement, $\bar{u}_Y$, as a function of overall compressive strain. From this figure, it can be clearly seen that both strain gradient elasticity and flexoelectricity can delay the onset of folding. To better understand the reason behind this behavior, we plot different terms of the energy density in Eq. 2.48 averaged over a semicircular control volume of $1\mu m$ radius around the fold tip as shown in Fig. 5.6, as a function of overall compressive strain. It should be noted that as the electromechanical enthalpy in Eq. 2.48 is related to a Min-Max problem, careful consideration has to be taken to interpret the energies since a physical interpretation of the electromechanical enthalpy is not clear. However, without flexoelectricity, the electromechanical enthalpy is reduced to a mechanical energy density which is related to a minimization problem for which a clear physical interpretation exists. This mechanical energy density is the sum of the strain and strain gradient energy densities shown in Figs. 5.7a and 5.7b. From Figs, 5.7c, 5.7d, and 5.7e it can be seen that for the first two cases (cases without flexoelectricity), the non-mechanical energy densities are zero. So, comparing the first two cases, it can be seen that folding generates very large strain gradients which activate the strain gradient elasticity energy term. As both of the terms have the same sign, the energy required for folds to form is higher for the case with strain gradient elasticity compared to the case without it. As a consequence, this results in a delay in the formation of folds.

To interpret the contribution of flexoelectricity, one may argue that flexoelectricity results in the generation of electric fields that can resist the formation of folds. This can be better understood with the help of Figs. 5.1, 5.5, and 5.7. As discussed, the results provided in Section 5.1.1 are related to a mostly one-way coupled problem (strain gradient generates electric field, but the effect of the electric field on the strain gradient is small). Besides, as the coupling is linear in Fig. 5.1, one could roughly estimate the mean vertical electric field generated on the fold tip for an arbitrary combination (yet in the same order such that the deformations are not affected significantly) of flexoelectric coefficients by superposing the response of each of the coefficients. In the transition from wrinkle to fold, a requirement for the electric field to affect the strain gradient and consequently the deformation state is the change in the slope of the electric field as the system goes from wrinkle to fold. In other words, if the slope of the electric field around the fold tip remains constant during the transition from wrinkle to fold, the generated electric field is decoupled from the change of the strain gradient as the system goes from wrinkle to fold. From Fig. 5.1a, it can be seen that in transition from wrinkle to fold, μ_L and μ_T generate a net vertical electric field of a similar slope (positive), while μ_S generates a net vertical electric field of an opposite slope (negative). With this background, one may expect that the combination of μ_L and μ_T of a similar sign and μ_S of the opposite sign can significantly change the slope of the vertical electric field (concluded from Fig. 5.1) in the transition from wrinkle to fold. Therefore, this case should be significantly affected by the generated electric field. As can be seen in 5.5a, the formation of the folds has been suppressed by flexoelectricity for this case. Besides, for other flexoelectric cases, it can be seen

from 5.5b and 5.5a that the effect of flexoelectricity and the generated electric field on the onset of folding is small for a case where the slope of the mean vertical electric field-overall compressive strain does not noticeably change (the yellow curve).

– –	$\mu_L = 0,$	$\mu_T = 0,$	$\mu_S = 0,$	$l_1 = 0$
– –	$\mu_L = 0,$	$\mu_T = 0,$	$\mu_S = 0,$	$l_1 = 0.125$
·····	$\mu_L = 100,$	$\mu_T = 100,$	$\mu_S = 0,$	$l_1 = 0.125$
·····	$\mu_L = 100,$	$\mu_T = -100,$	$\mu_S = 100,$	$l_1 = 0.125$
·····	$\mu_L = 100,$	$\mu_T = 300,$	$\mu_S = -100,$	$l_1 = 0.125$

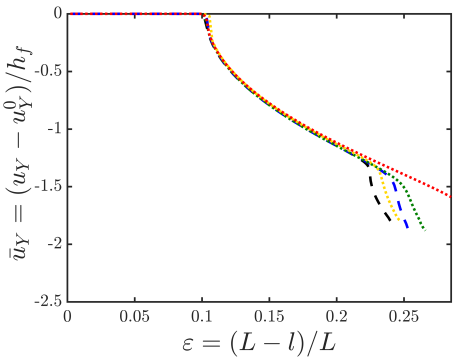

(a) Normalized relative vertical displacement of a fold tip (wrinkle valley) as a function of macroscopic compressive strain ε: Change of the onset of folding due to strain gradient elasticity and flexoelectricity.

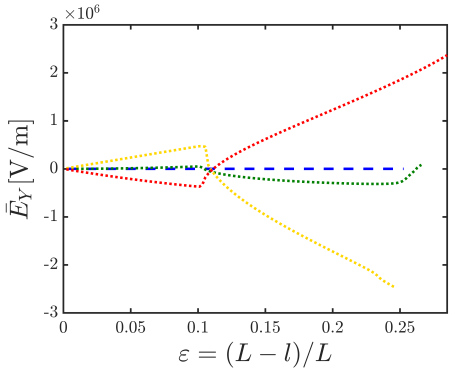

(b) Net vertical electric field generated on a fold tip (wrinkle valley) as a function of macroscopic compressive strain ε.

Figure 5.5: Change of the onset of folding due to strain gradient elasticity and flexoelectricity.

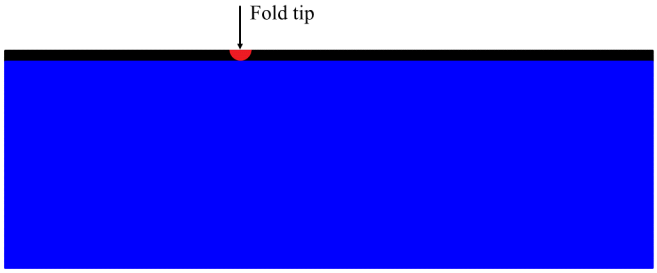

Figure 5.6: A control volume on the fold tip to compute different terms of the energy density in the electromechanical enthalpy (Eq. 2.48).

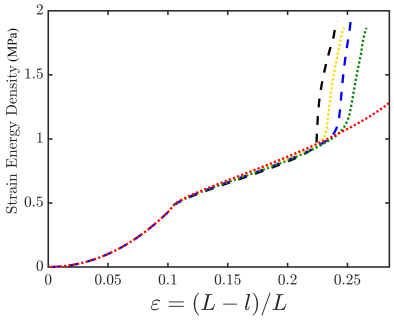

(a) Strain energy density (in MPa) in a semicircular control volume of radius $1\mu m$ around the fold tip (wrinkle valley) as a function of macroscopic comprehensive strain.

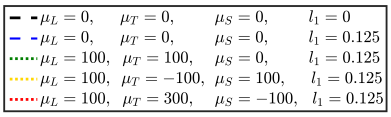

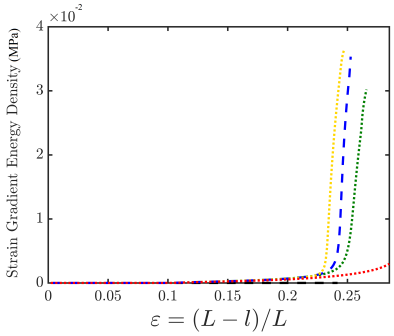

(b) Strain gradient energy density (in MPa) in a semicircular control volume of radius $1\mu m$ around the fold tip (wrinkle valley) as a function of macroscopic comprehensive strain.

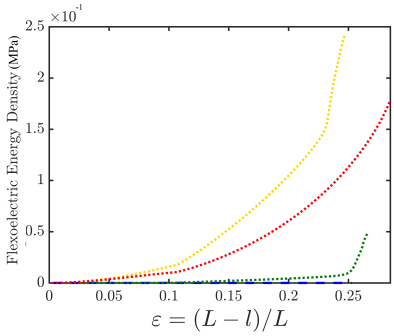

(c) Flexoelectric energy density (in MPa) in a semicircular control volume of radius $1\mu m$ around the fold tip (wrinkle valley) as a function of macroscopic comprehensive strain.

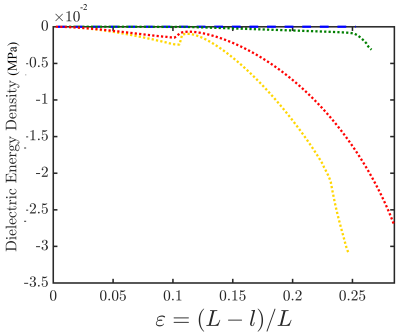

(d) Dielectric energy density (in MPa) in a semicircular control volume of radius $1\mu m$ around the fold tip (wrinkle valley) as a function of macroscopic comprehensive strain.

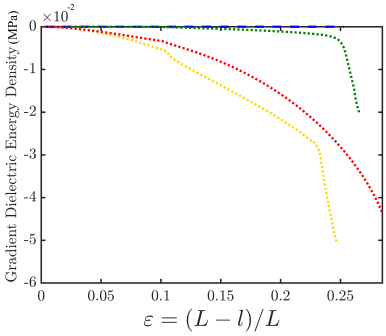

(e) Gradient dielectric energy density (in MPa) in a semicircular control volume of radius $1\mu m$ around the fold tip (wrinkle valley) as a function of macroscopic comprehensive strain.

Figure 5.7: Terms of energy density averaged over a semicircular control volume of radius $1\mu m$ around the fold tip (wrinkle valley).

5.2 Gradient effects cause notch strengthening and flaw-insensitive fracture

It is well known that the presence of flaws e.g. cracks and notches in structural components results in a stress concentration in the vicinity of the crack/notch tip and consequently a weakening effect in brittle or quasi-brittle materials. Cracks and notches are mainly considered to be the critical parts of the structures from which fracture initiates. However, experimental observations on micrometer-sized notched aluminum specimens with average grain size of 50 nm and notch depth of 400-1000 nm showed an absence of any measurable stress concentration in the close vicinity of the notch tip (Kumar *et al.*, 2011). Besides, a few experimental investigations on nanoscale notched specimens demonstrated the possibility of flaw-insensitive fracture (Gu *et al.*, 2013, Kumar *et al.*, 2009). The flaw-insensitivity can be defined as the insensitivity of either the location of the initiation of fracture or the strength of the material to the presence of flaws in a component (Gao *et al.*, 2003, Gu *et al.*, 2013). By in situ fracture tests on aluminum nanoscale thin film with average grain size of 50 nm and notch depth of 500-800 nm, Kumar *et al.* (2009) observed that the brittle fracture occurred far from the preexisting notch. Furthermore, a well-controlled experimental study on nanoscale notched platinum cylinders with an average grain size of 6 nm and circumferential length of 40-200 nm was carried out which showed the possibility of the initiation of brittle fracture far from the prefabricated notch and demonstrated that the strength of the specimens was independent of whether or not the fracture occurred at the notch (Gu *et al.*, 2013). In addition, employing Molecular Dynamics (MD) simulations, Zhang *et al.* (2012) found that although nanocrystalline graphene became flaw tolerant below a critical structural size, the strength of single-crystalline graphene was sensitive to the aspect ratio of the flaw. While different arguments have been raised to explain how the local stress around the flaw tip is relaxed, there has not yet been a consensus about this matter. It appears that the size effect character of these observations is central to the observed material behavior.

A fundamentally relevant phenomenon to the flaw-insensitive fracture is the so-called notch strengthening effect which can be defined as follows: the more severe the notch is in terms of the notch stress intensity factors exhibited at the notch tip, the tougher it becomes. Notch strengthening or weakening was conventionally thought to depend on ductility or brittleness of the material (Hertzberg and Hauser, 1977), but, recent studies suggest that this traditional assumption is not physically sound. Instead, a transition between failure modes may play a pivotal role in this phenomenon (Lei *et al.*, 2015, Qu *et al.*, 2014, Sha *et al.*, 2015, 2019). Recently, it has been observed that bone with a fatigue pre-crack is two times tougher than that with a blunt notch (Tertuliano *et al.*, 2020).

The mentioned observations imply that the classical Linear Elastic Fracture Mechanics (LEFM) and the classical continuum models are not valid tools to accurately describe the stress field in the vicinity of crack/notch tip and therefore to describe material behavior when the main source of heterogeneity in the material e.g. grain size in crystalline materials is

comparable to the size of specimen and external flaw (Mindlin, 1963, Shimada *et al.*, 2015). In other words, LEFM is not able to predict the notch strengthening effect and flaw-insensitive fracture.

Strain gradient enrichment of classical continuum theories has been shown to be successful in reproducing size effects (Askes and Aifantis, 2011a, Mindlin and Eshel, 1968a). Even though non-local enriched continuum models have been well studied in the context of fracture mechanics (Bazant, 1999, 2000, Peerlings *et al.*, 1996, Placidi and Barchiesi, 2018, Zhang and Luo, 2021), surprisingly, they have been barely explored in the context of notch fracture mechanics (Askes *et al.*, 2013, Bagni *et al.*, 2016, Susmel *et al.*, 2013). We will show that continuum simulations based on strain gradient elasticity theories are able to capture the flaw-insensitivity and notch strengthening effect. So, one can introduce the flaw-insensitivity and notch strengthening as gradient effects. With this argument, we expect any physical mechanism related to strain gradients, e.g. flexoelectricity and flexomagnetism (Lee *et al.*, 2017) to have a contribution towards flaw-insensitive fracture and notch strengthening effect. Flexoelectricity has been shown to affect the physics of crack formation and propagation (Abdollahi *et al.*, 2015b, Cordero-Edwards *et al.*, 2019, Núñez-Toldrà *et al.*, 2020, Wang *et al.*, 2019c). Through a computational study, Abdollahi *et al.* (2015b) showed that flexoelectricity produces a toughening effect as well as a toughness asymmetry. The toughness asymmetry predicted by Abdollahi *et al.* (2015b), has recently been observed in an experimental study (Cordero-Edwards *et al.*, 2019). Besides, Wang *et al.* (2019c) demonstrated the presence of a huge flexoelectric polarization around the crack tip which reveals the relevance of flexoelectricity in the fracture phenomenon.

In this study, a higher-order continuum model with the contribution of flexoelectricity will be employed to study the gradient effects in brittle or quasi-brittle materials. Immersed boundary B-Spline method (Codony *et al.*, 2019) is used to solve the fourth-order governing differential equations of the flexoelectric/strain-gradient solid. An energy-based notch fracture criterion namely Averaged Strain Energy Density (ASED) (Lazzarin and Zambardi, 2001) will be employed to evaluate the onset of brittle fracture. ASED has been a powerful method to predict the brittle fracture of notched components made of different materials (Berto and Lazzarin, 2014). This study introduces notch strengthening and flaw-insensitive fracture as gradient effects, provides new insights on gradient effects in the fracture physics of the materials, and shows the contribution of flexoelectricity. This understanding can provide insights into other types of materials, for instance bones (Gao *et al.*, 2003, Núñez-Toldrà *et al.*, 2020, Tertuliano *et al.*, 2020, Vasquez-Sancho *et al.*, 2018), and open a new route to model and optimize flaw-tolerant meta-materials (Montemayor *et al.*, 2016, Zhang *et al.*, 2019).

5.2.1 Methodology

The electromechanical enthalpy density considered in this study has been provided in Eq. 2.10. Lifshitz-invariant flexoelectric model is considered. For details, the reader is invited to refer to Section 2.1.2. To evaluate the gradient effects on the fracture of notched components, we

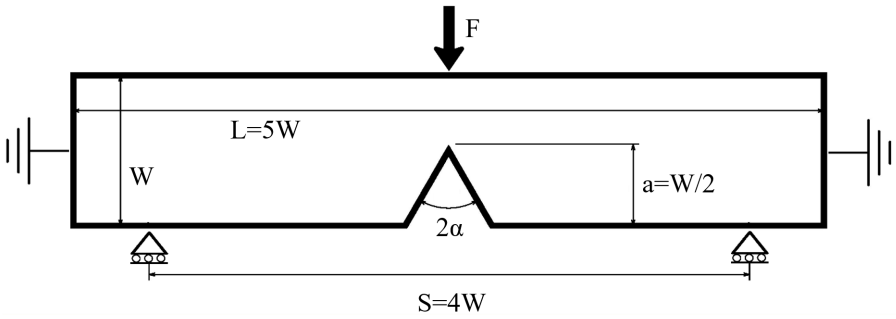

Figure 5.8: Geometry of the specimen under three-point bending configuration and the boundary conditions.

employ an approach based on the well-known ASED fracture criterion (Berto and Lazzarin, 2014, Lazzarin and Zambardi, 2001) which states that the brittle or quasi-brittle fracture occurs, when the averaged value of the strain energy density over a control volume reaches a critical value. The size of the control volume is determined based on material properties, i.e. plain strain fracture toughness, tensile strength, and poisson's ratio (Berto and Lazzarin, 2014). In linear elastic materials, the averaged value of the strain energy density over a small control volume of arbitrary size around the notch tip is directly correlated to the Notch Stress Intensity Factor (NSIF) (Lazzarin *et al.*, 2010). Therefore, under the same loading condition and the specimen size, the inverse of the square root of the ratio between the ASED over a control volume of the same size around two different notches can directly give a meaningful estimate of the ratio between their toughness.

To study the notch strengthening effect, two sharp V-notched beams are considered with notch opening angles (2α) equal to 30° and 150° and a notch depth (a) of W/2, where W is the specimen width. In linear elastic materials, for a sharp V-notch, an increase in the notch opening angle reduces the degree of singularity of the stress field (Filippi *et al.*, 2002), therefore, a notched beam with an opening angle of 30° experiences a more severe stress condition than a notch with an opening angle of 150°. The three-point bending test is simulated, where the specimens are under mode I loading condition (Fig. 5.8). In agreement with ASTM E1820, the aspect ratio of the beam is fixed to L/W=5, L being the length of the notched beam, and the span/width ratio is fixed to S/W=4. A small control volume of the radius R=0.02W is considered to calculate the averaged value of the strain energy density in the vicinity of the notch tip. Although the results may be affected by the chosen size of the control volume, the overall behavior is expected to remain unchanged. All the simulations are carried out under plane strain condition. The right and left faces of the notched beams are assumed to be connected to the ground; i.e. the electric potential is fixed to zero, while the other sides are considered to be charge-free. Due to symmetry, only half of the notched beams are analyzed.

The following material parameters have been considered in the simulations to fit the

behavior of nanocrystalline Barium Strontium Titanate (BST) at its paraelectric phase (Zubko *et al.*, 2013):

$$Y = 152\text{GPa}, \quad \nu = 0.25, \quad \ell_1 = 1\text{nm}, \quad \epsilon = 11\text{nC/Vm}, \quad \mu_{\text{L}} = \mu_{\text{T}} = \{0.121, 121\}\mu\text{C/m},$$
$$\ell_2 = 1\text{nm}, \qquad \mu_{\text{S}} = 0. \tag{5.7}$$

For the flexoelectric coefficients, μ_{L} and μ_{T}, two values have been considered, the larger is associated to BST at its paraelectric phase (Zubko *et al.*, 2013), while the smaller have been considered to represent the behavior of a considerably weaker flexoelectric material. The flexoelectric length scale (Eq. A.6) for BST and the weaker flexoelectric material are $\ell_\mu \sim 3\mu m$ and $\ell_\mu =\sim 3nm$, respectively, the latter is comparable to the strain gradient elasticity length scale, ℓ_1.

5.2.2 Results and discussion

From the simulations, the ASED around the notch tip was calculated. In the remainder, the square root of the ratio between ASED in a control volume around a notch with an opening angle of 30° and that of a notch with an opening angle of 150° is named toughness ratio. A toughness ratio larger than 1 means that a notch with opening angle of 150° is tougher than a notch with opening angle 30°, while a toughness ratio less than 1 means the opposite.

Figure 5.9 shows the toughness ratio as a function of the normalized width of the beam for different physics and material parameters. As expected, without considering strain gradient elasticity and flexoelectricity, for a linear elastic material, the toughness ratio is independent of the size of the specimen which confirms the inability of LEFM and classical continuum theories to predict any size effect such as the notch strengthening effect. By introducing the strain gradient elasticity term, decreasing the specimen's size causes a significant decrease in the toughness ratio followed by a modest increase in very small specimens. Furthermore, the toughness ratio is larger than 1, as expected at the macroscale. Below a certain size, the notch strengthening happens where the severe notch (30°) becomes tougher than a gentle notch (150°). Introducing flexoelectricity increases the notch strengthening effect. This figure predicts that for BST, the notch strengthening effect occurs even in micrometer scales. The increase in the toughness ratio at very small specimens is related to a transition from tensile fracture mode (mode I) to shear mode (mode II). By decreasing the size of the specimens, a stiffening phenomenon happens, so that at very small specimens the contribution of shear stress exceeds that of normal stress (Aifantis, 1999). This can be clearly seen in Fig. 5.10 in which the components of strain of the 30° notched specimen are shown for various normalized specimen's widths W/l_1.

To investigate the flaw-insensitive fracture, let us focus on the V-notched specimen with an opening angle of 30°. From the simulations, a control volume in which the ASED takes its maximum value is found. Then, the square root of the ratio between the maximum ASED and the ASED computed around the notch tip is calculated. The ratio equal to 1 implies that

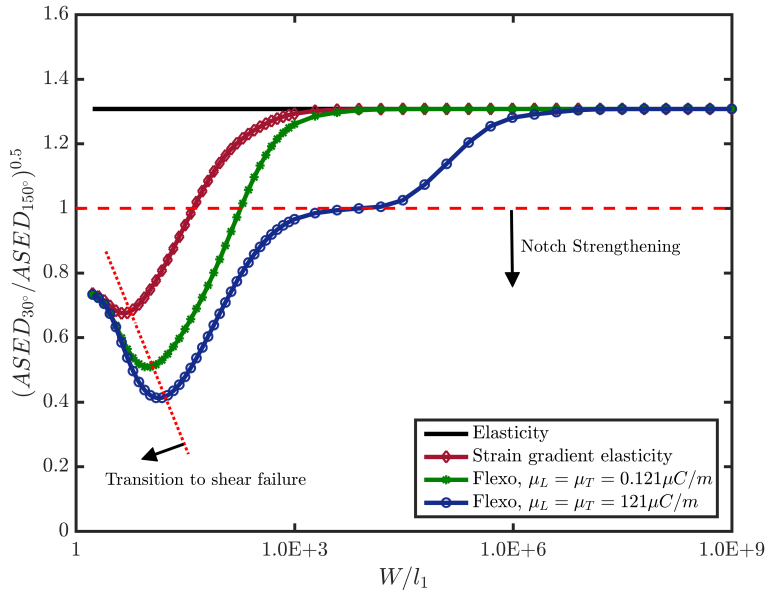

Figure 5.9: Toughness ratio as a function of normalized specimen's width W/l_1.

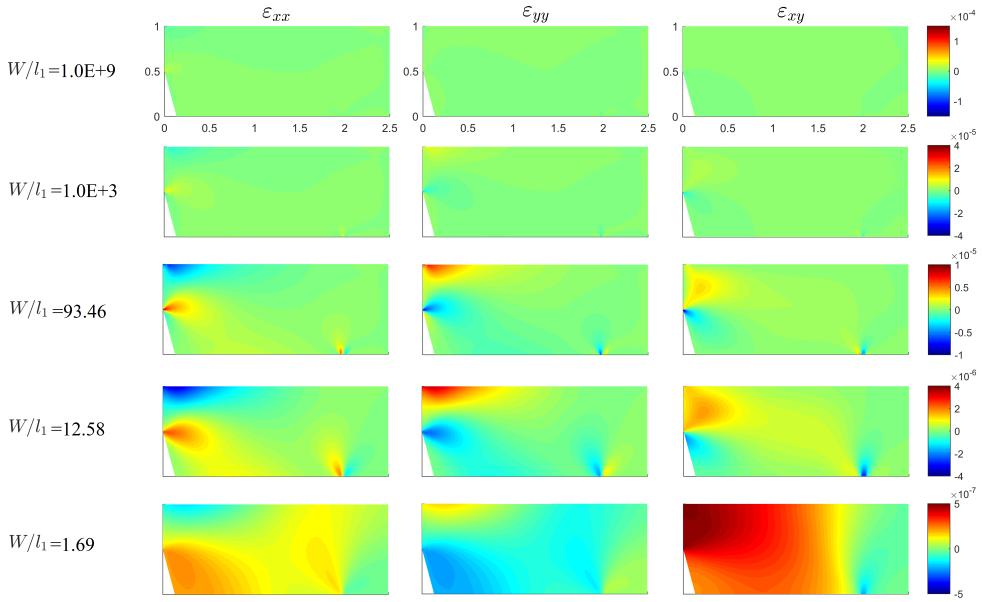

Figure 5.10: Strain components for different specimen size for the case with $\mu_L = \mu_T$ = 121μC/m.

the critical point in the specimen having the maximum ASED is exactly at the notch tip. Any value larger than 1 means that the critical point of the specimen is no longer placed on the

notch tip. From our calculations, it can be seen that flaw-insensitivity does not occur in a linear elastic material. By introducing strain gradient elasticity term, the specimen becomes notch-insensitive for normalized specimen's widths $W/l_1 <\sim 18$. For flexoelectric materials, the specimen becomes insensitive to the notch at higher scales. In particular, our calculations show that BST becomes notch insensitive for normalized specimen's widths $W/l_1 <\sim 94$.

To better interpret the results, the length scale parameter l_1 can be described in terms of the size of the Representative Volume Element (RVE), denoted as L_{RVE}. The expression $l_1^2 = \frac{1}{12} L_{\text{RVE}}^2$ has been found in the literature (Askes and Aifantis, 2011a). In crystalline materials, assuming L_{RVE} to be 20 times as large as the grain size L_{Grain} (Gitman, 2006), we can obtain $l_1 \approx 6 L_{\text{Grain}}$. Therefore, based on the results provided here, without considering flexoelectricity, a strain gradient material can become flaw-insensitive when $W/l_{\text{Grain}} <\sim 108$. This is in agreement with the results provided in (Gu *et al.*, 2013, Kumar *et al.*, 2009, 2011, Zhang *et al.*, 2012). The results show that flexoelectric dielectrics may become flaw-insensitive at larger W/l_{Grain}

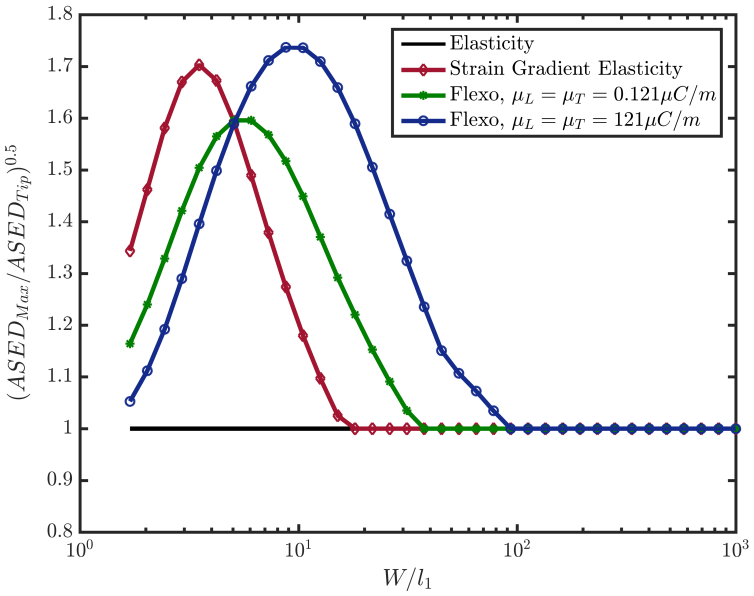

Figure 5.11: Square root of the ratio between maximum averaged strain energy density (ASED_{Max}) and averaged strain energy density computed around the notch tip (ASED_{Tip}) as a function of normalized specimen's width W/l_1 for a 30° notched specimen.

5.3 Conclusions

The focus of this chapter was to explore how flexoelectricity can affect material behaviour. In particular, we put our attention to stress singularities around which very large strain gradients exist. First, we studied folding instability in soft bilyers and showed that flexoelectricity can

cause a delay in the formation of folds, i.e. larger macroscopic compressive strain is needed for the film to fold with flexoelectricity. Then, we studied the fracture of notched specimens made of brittle materials and suggested that flaw-insensitive fracture and notch strengthening are gradient effects. Based on this suggestion, we expect any physical mechanism coupled with strain gradients to have a contribution towards these phenomena. By means of a self-consistent continuum model, we showed that flexoelectricity can have a significant contribution towards notch strengthening and flaw-insensitive fracture, predicting that Barium Strontium Titanate (BST) in its paraelectric phase may exhibit notch strengthening in micrometer scales and become flaw-insensitive below 94 nm.

Chapter 6

Conclusions

In this Ph.D. thesis, we have addressed several questions about the continuum modeling of flexoelectricity in dielectric elastomers, its fundamental manifestations, and potential applications of flexoelectricity in solids. The main contributions can be summarized as follows:

- We started the thesis by exploring the inherent surface effects of flexoelectricity models in infinitesimal strains. We put our main attention to the Lifshitz-invariant model of flexoelectricity and showed that under the application of a homogeneous compression or electric field along the length of a thin film, the surface of the material shows two-way piezoelectric-like behavior. We attributed this behavior to the symmetry-breaking nature of the surfaces and argued that the origin of these effects is inverse flexoelectricity (generation of strain gradient due to the application of homogeneous electric field), and inverse-converse flexoelectricity (generation of electric field gradient due to application of homogeneous deformation). Considering only the direct or converse model of flexoelectricity in the electromechanical enthalpy leads to losing one of the mentioned inherent surface effects which eventually results in a one-way surface piezoelectric-like behavior. We provided closed-form solutions that can describe the inherent surface effects of flexoelectricity and their dependencies.

- We formulated the Lifshitz-invariant model of flexoelectricity for finite strains taking into account material incompressibility and material interfaces. We commented on the connection between energy and enthalpy forms of the Lifshitz-invariant flexoelectricity models for finite deformations.

- We studied surface instabilities in flexoelectric/dielectric bilayers and successfully captured the well-known surface instability patterns namely wrinkle, ridge, period-double, fold, and crease which shows the robustness of our approach for modeling and simulation of surface instabilities. To provide insights into the surface instabilities in flexoelectric/dielectric bilayers, we explored the electromechanical response of each family of instability patterns.

- We observed a linear increase in the electric field in flexoelectric/dielectric bilayers subjected to macroscopic strain in the flat state. With the lessons learned from Section 2, we explained this behavior to be due to the boundary layers that develop under homogeneous macroscopic deformations as a result of surface-induced symmetry breaking and surface relaxation.

- We explored three potential applications for instability-based devices. We first studied the possibility of electrically activating the pattern change in dielectric bilayers commenting on the role of flexoelectricity to cause an asymmetrical response with positive and negative external bias. We then presented the design of a lateral compression sensor and a pressure sensor.

- With the aim to explore the fundamental manifestations of flexoelectricity, we focused on stress singularities such as folds in soft bilayers and notches in hard materials. We showed that flexoelectricity can result in a delay in the formation of folds. Besides, we introduced the notch-strengthening effect and flaw-insensitive fracture as gradient effects and showed that flexoelectricity can contribute to these phenomena. We showed that BST in its paraelectric phase may exhibit notch strengthening in micrometer scale and become flaw tolerant below 94 nm.

Appendices

A Material characterization for the linear model

The electromechanical enthalpy density described in Eq. 2.10 involves five material tensors. We define them in this appendix.

Isotropic elasticity tensor is considered here as

$$\begin{aligned} \mathbb{C}_{iiii} &= C_L, && i = 1,2, \\ \mathbb{C}_{iijj} &= C_T, && i,j = 1,2 \text{ with } i \neq j, \\ \mathbb{C}_{ijij} = \mathbb{C}_{ijji} &= C_S, && i,j = 1,2 \text{ with } i \neq j. \end{aligned} \tag{A.1}$$

In plain strain condition, C_L,C_T and C_S are defined in terms of elasticity modulus Y and Poisson's ratio ν as

$$C_L := \frac{Y(1-\nu)}{(1+\nu)(1-2\nu)}, \qquad C_T := \frac{Y\nu}{(1+\nu)(1-2\nu)}, \qquad C_S := \frac{Y}{2(1+\nu)}. \tag{A.2}$$

We use a simplified form of isotropic strain elasticity tensor which depends on the elasticity modulus Y, the Poisson ratio ν and the internal length scale l_1 as (Altan and Aifantis, 1997, Mindlin, 1964)

$$\begin{aligned} h_{iikiik} &= l_1^2 C_L, && i,k = 1,2, \\ h_{iikjjk} &= l_1^2 C_T, && i,j,k = 1,2 \text{ with } i \neq j, \\ h_{ijkijk} = h_{ijkjik} &= l_1^2 C_S, && i,j,k = 1,2 \text{ with } i \neq j. \end{aligned} \tag{A.3}$$

where the parameters C_L, C_S and C_T are defined in Eq. (A.2).

We use a second-order tensor to describe isotropic dielectricity $\boldsymbol{\kappa}$, which depends on the electric permittivity ϵ as

$$\kappa_{ii} = \epsilon, \qquad i = 1,2. \tag{A.4}$$

Flexoelectricity is represented by a fourth-order tensor $\boldsymbol{\mu}$. Ferroelectric perovskites in their paraelectric phase are characterized by a cubic-symmetric flexoelectricity tensor involving only three independent flexoelectric coefficients, namely longitudinal μ_{L}, transverse μ_{T} and shear μ_{S}.

$$\begin{aligned} \mu_{iiii} &= \mu_L, && i = 1,2, \\ \mu_{ijji} &= \mu_T, && i,j = 1,2 \text{ with } i \neq j, \\ \mu_{iijj} = \mu_{ijij} &= \mu_S, && i,j = 1,2 \text{ with } i \neq j. \end{aligned} \tag{A.5}$$

The flexoelectric length scale can be defined as

$$\ell_{flexo} = \frac{\mu^2}{Y\epsilon}. \tag{A.6}$$

We consider a simplified isotropic gradient dielectricity tensor which depend on electric permittivity of the material ϵ and the length scale ℓ_2 in the following form (Mindlin, 1968):

$$M_{ijij} = \epsilon\ell_2^2. \tag{A.7}$$

B Material characterization for the nonlinear model

The material is fully characterized by specifying the material tensors of strain gradient elasticity **h**, flexoelectricity $\boldsymbol{\mu}$, and gradient dielectricity $\boldsymbol{M}$.

Strain gradient elasticity tensor h.

We consider an isotropic simplified strain gradient elasticity tensor, which depends on shear modulus G and the length scale ℓ_1 in the following form:

$$h_{IJKLMN} = 2G\delta_{IL}\delta_{JM}\delta_{KN}\ell_1^2. \tag{B.1}$$

Flexoelectricity tensor $\boldsymbol{\mu}$.

The cubic flexoelectric tensor depends on the longitudinal μ_{L}, transversal μ_{T} and shear μ_{S} parameters (Codony *et al.*, 2019). In the Cartesian axes, it takes the following form:

$$\mu_{LIJK} = \begin{cases} \mu_{\mathrm{L}}, & \text{for } L = I = J = K, \\ \mu_{\mathrm{T}}, & \text{for } I = J \neq K = L, \\ \mu_{\mathrm{S}}, & \text{for } L = I \neq J = K \text{ or } L = J \neq I = K, \\ 0 & \text{otherwise.} \end{cases} \tag{B.2}$$

The flexoelectric length scale can be defined as

$$\ell_{flexo} = \frac{\mu^2}{Y\epsilon}, \tag{B.3}$$

where $Y = 3G$ is the elasticity modulus for incompressible materials.

Gradient dielectricity tensor M.

We consider a simplified gradient dielectricity tensor which depend on electric permittivity of the material ϵ and the length scale ℓ_2 in the following form (Mindlin, 1968):

$$M_{IJKL} = \epsilon \delta_{IJKL} \ell_2^2, \tag{B.4}$$

where δ_{IJKL} is unity if all indices are identical and zero otherwise.

C Application of divergence, the surface divergence and Stokes theorems on the first variation of $\Pi[\boldsymbol{\chi}, \Phi]$

The divergence, the surface divergence and Stokes theorems can be applied to Eq. (2.57) in order to obtain the definitions of the Neumann terms as well as the strong form of the problem. In the following, we separate the terms on the integrals on the domain in Eq. (2.57) and integrate them by parts. The terms including variations $\delta\chi_{i,J}$ and $\delta\Phi_{,L}$ which are not independent of $\delta\chi_i$ and $\delta\Phi$ are further expanded using the surface divergence and Stokes theorems. For a detailed discussion please refer to (Hu and Shen, 2010). The resulting terms are written as

$$\int_{\Omega_0} \left(\frac{\partial \bar{\Psi}^{\text{Enth}}}{\partial \mathfrak{E}_{IJ}} \delta \mathfrak{E}_{IJ} \right) \mathrm{d}\Omega_0 = \int_{\partial\Omega_0} F_{iI} \hat{S}_{IJ} N_J \delta x_i \, \mathrm{d}\Gamma_0 - \int_{\Omega_0} \left(F_{iI} \hat{S}_{IJ} \right)_{,J} \delta\chi_i \, \mathrm{d}\Omega_0, \tag{C.1}$$

$$\begin{aligned}
\int_{\Omega_0} \left(\frac{\partial \bar{\Psi}^{\text{Enth}}}{\partial \widetilde{\mathfrak{E}}_{IJK}} \delta \widetilde{\mathfrak{E}}_{IJK} \right) \mathrm{d}\Omega_0 &= \int_{\partial\Omega_0} \tilde{F}_{iIK} \tilde{S}_{IJK} N_J \delta\chi_i \, \mathrm{d}\Gamma_0 - \int_{\Omega_0} \left(\tilde{F}_{iIK} \tilde{S}_{IJK} \right)_{,J} \delta\chi_i \, \mathrm{d}\Omega_0 \\
&+ \int_{\partial\Omega_0} F_{iI} \tilde{S}_{IJK} N_K \delta\chi_{i,J} \, \mathrm{d}\Gamma_0 - \int_{\Omega_0} \left(F_{iI} \tilde{S}_{IJK} \right)_{,K} \delta\chi_{i,J} \, \mathrm{d}\Omega_0 \\
&= \int_{\partial\Omega_0} \tilde{F}_{iIK} \tilde{S}_{IJK} N_J \delta\chi_i \, \mathrm{d}\Gamma_0 - \int_{\Omega_0} \left(\tilde{F}_{iIK} \tilde{S}_{IJK} \right)_{,J} \delta\chi_i \, \mathrm{d}\Omega_0 \\
&- \int_{\partial\Omega_0} \left(F_{iI} \tilde{S}_{IJK} \right)_{,K} N_J \delta\chi_i \, \mathrm{d}\Gamma_0 + \int_{\Omega_0} \left(F_{iI} \tilde{S}_{IJK} \right)_{,JK} \delta\chi_i \, \mathrm{d}\Omega_0 \\
&- \int_{\partial\Omega_0} \left(F_{iI} \tilde{S}_{IJK} \right)_{,L} \mathbb{P}_{JL} N_K \delta\chi_i \, \mathrm{d}\Gamma_0 + \int_{\partial\Omega_0} F_{iI} \tilde{S}_{IJK} \left[\widetilde{N} \right]_{JK} \delta\chi_i \, \mathrm{d}\Gamma_0 \\
&+ \int_{\partial\Omega_0} F_{iI} \tilde{S}_{IJK} N_J N_K \partial^N \delta\chi_i \, \mathrm{d}\Gamma_0 + \int_{C_0} [\![F_{iI} \tilde{S}_{IJK} \mathfrak{M}_J N_K]\!] \delta\chi_i \, \mathrm{d}s_0,
\end{aligned} \tag{C.2}$$

$$\int_{\Omega_0} \left(\frac{\partial \bar{\Psi}^{\text{Enth}}}{\partial E_L} \delta E_L \right) \mathrm{d}\Omega_0 = \int_{\partial\Omega_0} \widehat{D}_L N_L \delta\Phi \, \mathrm{d}\Gamma_0 - \int_{\Omega_0} \widehat{D}_{L,L} \delta\Phi \, \mathrm{d}\Omega_0, \tag{C.3}$$

$$\begin{aligned}
\int_{\Omega_0} \left(\frac{\partial \bar{\Psi}^{\text{Enth}}}{\partial \widetilde{E}_{LM}} \delta \widetilde{E}_{LM} \right) \mathrm{d}\Omega_0 &= \int_{\partial\Omega_0} \widetilde{D}_{LM} N_M \delta\Phi_{,L} \, \mathrm{d}\Gamma_0 - \int_{\Omega_0} \widetilde{D}_{LM,M} \delta\Phi_{,L} \, \mathrm{d}\Omega_0 \\
&= - \int_{\partial\Omega_0} \widetilde{D}_{LM,M} N_L \delta\Phi \, \mathrm{d}\Gamma_0 + \int_{\Omega_0} \widetilde{D}_{LM,LM} \delta\Phi \, \mathrm{d}\Omega_0 \\
&- \int_{\partial\Omega_0} \left(\widetilde{D}_{LM} \right)_{,K} \mathbb{P}_{LK} N_M \delta\Phi \, \mathrm{d}\Gamma_0 + \int_{\partial\Omega_0} \widetilde{D}_{LM} \left[\widetilde{N} \right]_{LM} \delta\Phi \, \mathrm{d}\Gamma_0 \\
&+ \int_{\partial\Omega_0} \widetilde{D}_{LM} N_L N_M \partial^N \delta\Phi \, \mathrm{d}\Gamma_0 + \int_{C_0} [\![\widetilde{D}_{LM} \mathfrak{M}_L N_M]\!] \delta\Phi \, \mathrm{d}s_0.
\end{aligned} \tag{C.4}$$

D Second variation of the enthalpy functional

The second variation of the total energy of the domain including the material interface is given by

$$\delta^2\Pi^{\text{Bimaterial}} = \delta^2\Pi + \delta^2\Pi^{\text{Interface}} = \delta\mathcal{R}^{\text{Bimaterial}} = \delta\mathcal{R} + \delta\mathcal{R}^{\text{Interface}}. \tag{D.1}$$

The second variation of Π can be written as

$$\begin{aligned}
&\delta^2\Pi[\chi,\Phi,p;\delta\chi,\delta\Phi,\delta p;\Delta\chi,\Delta\Phi,\Delta p]\\
=&\delta\left(\mathcal{R}[\chi,\Phi,p;\delta\chi,\delta\Phi,\delta p]\right)[\Delta\chi,\Delta\Phi,\Delta p]\\
=&\frac{\partial\mathcal{R}[\chi,\Phi,p;\delta\chi,\delta\Phi,\delta p]}{\partial\chi}\Delta\chi+\frac{\partial\mathcal{R}[\chi,\Phi,p;\delta\chi,\delta\Phi,\delta p]}{\partial\Phi}\Delta\Phi+\frac{\partial\mathcal{R}[\chi,\Phi,p;\delta\chi,\delta\Phi,\delta p]}{\partial p}\Delta p\\
=&\int_{\Omega_0}\Bigg\{\left(\frac{\partial^2\bar{\Psi}^{\text{Enth}}}{\partial\mathfrak{E}_{IJ}\partial\mathfrak{E}_{KL}}\right)\delta\mathfrak{E}_{IJ}\Delta\mathfrak{E}_{KL}+\left(\frac{\partial\bar{\Psi}^{\text{Enth}}}{\partial\mathfrak{E}_{IJ}}\right)\Delta\delta\mathfrak{E}_{IJ}+\left(\frac{\partial^2\bar{\Psi}^{\text{Enth}}}{\partial\widetilde{\mathfrak{E}}_{IJK}\partial\widetilde{\mathfrak{E}}_{LMN}}\right)\delta\widetilde{\mathfrak{E}}_{IJK}\Delta\widetilde{\mathfrak{E}}_{LMN}\\
&+\left(\frac{\partial\bar{\Psi}^{\text{Enth}}}{\partial\widetilde{\mathfrak{E}}_{IJK}}\right)\Delta\delta\widetilde{\mathfrak{E}}_{IJK}+\left(\frac{\partial^2\bar{\Psi}^{\text{Enth}}}{\partial E_L\partial E_M}\right)\delta E_L\Delta E_M\left(\frac{\partial^2\bar{\Psi}^{\text{Enth}}}{\partial\tilde{E}_{LK}\partial\tilde{E}_{MN}}\right)\delta\tilde{E}_{KL}\Delta\tilde{E}_{MN}\\
&+\left(\frac{\partial^2\bar{\Psi}^{\text{Enth}}}{\partial\mathfrak{E}_{IJ}\partial\widetilde{\mathfrak{E}}_{KLM}}\right)\left(\delta\mathfrak{E}_{IJ}\Delta\widetilde{\mathfrak{E}}_{KLM}+\delta\widetilde{\mathfrak{E}}_{KLM}\Delta\mathfrak{E}_{IJ}\right)+\left(\frac{\partial^2\bar{\Psi}^{\text{Enth}}}{\partial\mathfrak{E}_{IJ}\partial E_K}\right)\left(\delta\mathfrak{E}_{IJ}\Delta E_K+\delta E_K\Delta\mathfrak{E}_{IJ}\right)\\
&+\left(\frac{\partial^2\bar{\Psi}^{\text{Enth}}}{\partial\mathfrak{E}_{IJ}\partial\tilde{E}_{KL}}\right)\left(\delta\mathfrak{E}_{IJ}\Delta\tilde{E}_{KL}+\delta\tilde{E}_{KL}\Delta\mathfrak{E}_{IJ}\right)+\left(\frac{\partial^2\bar{\Psi}^{\text{Enth}}}{\partial\mathfrak{E}_{IJ}\partial p}\right)\left(\delta\mathfrak{E}_{IJ}\Delta p+\delta p\Delta\mathfrak{E}_{IJ}\right)\\
&+\left(\frac{\partial^2\bar{\Psi}^{\text{Enth}}}{\partial\widetilde{\mathfrak{E}}_{IJK}\partial E_L}\right)\left(\delta\widetilde{\mathfrak{E}}_{IJK}\Delta E_L+\delta E_L\Delta\widetilde{\mathfrak{E}}_{IJK}\right)\Bigg\}\,\mathrm{d}\Omega_0,
\end{aligned} \tag{D.2}$$

where $\Delta\chi$, $\Delta\Phi$ and Δp are variations of χ, Φ and p, respectively, $\bar{\Psi}^{\text{Enth}} = \Psi^{\text{Enth}} + p(J-1)$ and

$$\Delta E_L := -\frac{\partial(\Delta\Phi)}{\partial X_L}, \tag{D.3a}$$

$$\Delta\tilde{E}_{LM} := -\frac{\partial^2(\Delta\Phi)}{\partial X_L\partial X_M}, \tag{D.3b}$$

$$\Delta F_{iI} := \frac{\partial(\Delta\chi_i)}{\partial X_I}, \tag{D.3c}$$

$$\Delta\tilde{F}_{iIJ} := \frac{\partial^2(\Delta\chi_i)}{\partial X_I\partial X_J}, \tag{D.3d}$$

$$\Delta\mathfrak{E}_{IJ} = \frac{\Delta C_{IJ}}{2} := \operatorname*{symm}_{IJ}\left(\Delta F_{kI}F_{kJ}\right), \tag{D.3e}$$

$$\Delta\widetilde{\mathfrak{E}}_{IJK} = \frac{\Delta\widetilde{C}_{IJK}}{2} := \operatorname*{symm}_{IJ}\left(\Delta F_{kI}\tilde{F}_{kJK}+F_{kI}\Delta\tilde{F}_{kJK}\right), \tag{D.3f}$$

$$(\Delta\delta)\mathfrak{E}_{IJ} = \frac{(\Delta\delta)C_{IJ}}{2} := \operatorname*{symm}_{IJ}\left(\Delta F_{kI}\delta F_{kJ}\right), \tag{D.3g}$$

$$(\Delta\delta)\widetilde{\mathfrak{E}}_{IJK} = \frac{(\Delta\delta)\widetilde{C}_{IJK}}{2} := \operatorname*{symm}_{IJ}\left(\Delta F_{kI}\delta\tilde{F}_{kJK} + \delta F_{kI}\Delta\tilde{F}_{kJK}\right). \tag{D.3h}$$

The second variation of $\Pi^{\text{Interface}}$ can be written as

$$\begin{aligned}
&\delta^2\Pi^{\text{Interface}}[\boldsymbol{\chi}, \Phi, p; \delta\boldsymbol{\chi}, \delta\Phi, \delta p; \Delta\boldsymbol{\chi}, \Delta\Phi, \Delta p] \\
=&\delta\left(\mathcal{R}^{\text{Interface}}[\chi, \Phi, p; \delta\chi, \delta\Phi, \delta p]\right)[\Delta\chi, \Delta\Phi, \Delta p] \\
=&\frac{\partial\mathcal{R}^{\text{Interface}}[\chi, \Phi, p; \delta\chi, \delta\Phi, \delta p]}{\partial\chi}\Delta\chi + \frac{\partial\mathcal{R}^{\text{Interface}}[\chi, \Phi, p; \delta\chi, \delta\Phi, \delta p]}{\partial\Phi}\Delta\Phi \\
&+ \frac{\partial\mathcal{R}^{\text{Interface}}[\chi, \Phi, p; \delta\chi, \delta\Phi, \delta p]}{\partial p}\Delta p = \\
&\int_I \Bigg[\beta^{\chi_I}\left[\!\left[\delta\chi_i N_J\right]\!\right]\left[\!\left[\Delta\chi_i N_J\right]\!\right] - \left[\!\left[\delta\chi_i N_J\right]\!\right]\left\{\Delta T_i N_J\right\}_\gamma \\
&- \left[\!\left[\Delta\chi_i N_J\right]\!\right]\left\{\delta T_i N_J\right\}_\gamma - \left[\!\left[\chi_i N_J\right]\!\right]\left\{(\Delta\delta) T_i N_J\right\}_\gamma\Bigg] \mathrm{d}\Gamma \\
&+ \int_I \Bigg[\beta^{\partial^N\chi_I}\left[\!\left[\partial^N\delta\chi_i\right]\!\right]\left[\!\left[\partial^N\Delta\chi_i\right]\!\right] - \left[\!\left[\partial^N\delta\chi_i\right]\!\right]\left\{\Delta R_i\right\}_\gamma \\
&- \left[\!\left[\partial^N\Delta\chi_i\right]\!\right]\left\{\delta R_i\right\}_\gamma - \left[\!\left[\partial^N\chi_i\right]\!\right]\left\{(\Delta\delta) R_i\right\}_\gamma\Bigg] \mathrm{d}\Gamma \\
&+ \int_I \Bigg[-\beta^{\Phi_I}\left[\!\left[\delta\Phi N_I\right]\!\right]\left[\!\left[\Delta\Phi N_I\right]\!\right] + \left[\!\left[\delta\Phi N_I\right]\!\right]\left\{\Delta W N_I\right\}_\gamma \\
&+ \left[\!\left[\Delta\Phi N_I\right]\!\right]\left\{\delta W N_I\right\}_\gamma + \left[\!\left[\Phi N_I\right]\!\right]\left\{(\Delta\delta) W N_I\right\}_\gamma\Bigg] \mathrm{d}\Gamma \\
&+ \int_I \Bigg[-\beta^{\partial^N\Phi_I}\left[\!\left[\partial^N\delta\Phi\right]\!\right]\left[\!\left[\partial^N\Delta\Phi\right]\!\right] + \left[\!\left[\partial^N\delta\Phi\right]\!\right]\left\{\Delta O\right\}_\gamma \\
&+ \left[\!\left[\partial^N\Delta\Phi\right]\!\right]\left\{\delta O\right\}_\gamma + \left[\!\left[\partial^N\Phi\right]\!\right]\left\{(\Delta\delta) O\right\}_\gamma\Bigg] \mathrm{d}\Gamma \\
&+ \sum_{k=1}^{H}\int_{C^k}\Big[\beta^{\chi_c}(\Delta\chi_i^1 - \Delta\chi_i^2)(\delta\chi_i^1 - \delta\chi_i^2) - (\delta\chi_i^1 - \delta\chi_i^2)(\Delta J_i^1 - \Delta J_i^2) \\
&\quad - (\Delta\chi_i^1 - \Delta\chi_i^2)(\delta J_i^1 - \delta J_i^2) - (\chi_i^1 - \chi_i^2)((\Delta\delta) J_i^1 - (\Delta\delta) J_i^2)\Big] \mathrm{d}s \\
&+ \sum_{k=1}^{H}\int_{C^k}\Big[-\beta^{\Phi_c}(\Delta\Phi^1 - \Delta\Phi^2)(\delta\Phi^1 - \delta\Phi^2) + (\delta\Phi^1 - \delta\Phi^2)(\Delta K^1 - \Delta K^2)
\end{aligned}$$

$$+ (\Delta\Phi^1 - \Delta\Phi^2)(\delta K^1 - \delta K^2) + (\Phi^1 - \Phi^2)((\Delta\delta)K^1 - (\Delta\delta)K^2)\Big] \, \mathrm{ds}, \tag{D.4}$$

where the variations of Neumann terms are defined as

$$\Delta T_i := \Delta_\chi T_i + \Delta_\Phi T_i + \Delta_p T_i, \tag{D.5a}$$
$$\Delta R_i := \Delta_\chi R_i + \Delta_\Phi R_i, \tag{D.5b}$$
$$\Delta J_i := \Delta_\chi J_i + \Delta_\Phi J_i, \tag{D.5c}$$
$$\Delta W := \Delta_\chi W + \Delta_\Phi W, \tag{D.5d}$$
$$\Delta O := \Delta_\chi O + \Delta_\Phi O, \tag{D.5e}$$
$$\Delta K := \Delta_\chi K + \Delta_\Phi K. \tag{D.5f}$$

In the equations above, the variations of Nuemann terms with respect to the field variables can be obtained as

$$\Delta_\chi T_i := \Bigg(\Delta F_{iI} \hat{S}_{IJ} + F_{iI} \Delta_\chi \hat{S}_{IJ} + \Delta \tilde{F}_{iIK} \tilde{S}_{IJK} + \tilde{F}_{iIK} \Delta_\chi \tilde{S}_{IJK}, \tag{D.6}$$

$$- \Delta_\chi \left(\frac{\partial (F_{iI} \tilde{S}_{IJK})}{\partial X_L} \right) \delta_{KL} - \Delta_\chi \left(\frac{\partial (F_{iI} \tilde{S}_{IKJ})}{\partial X_L} \right) \mathbb{P}_{KL} \Bigg) N_J, \tag{D.7}$$

$$+ \left(\Delta F_{iI} \tilde{S}_{IJK} + F_{iI} \Delta_\chi \tilde{S}_{IJK} \right) \left[\widetilde{N} \right]_{JK}, \tag{D.8}$$

$$\Delta_\Phi T_i := \Bigg(F_{iI} \Delta_\Phi \hat{S}_{IJ} + \tilde{F}_{iIK} \Delta_\Phi \tilde{S}_{IJK} - \Delta_\Phi \left(\frac{\partial (F_{iI} \tilde{S}_{IJK})}{\partial X_L} \right) \delta_{KL} - \Delta_\Phi \left(\frac{\partial (F_{iI} \tilde{S}_{IKJ})}{\partial X_L} \right) \mathbb{P}_{KL} \Bigg) N_J, \tag{D.9}$$

$$+ \left(F_{iI} \Delta_\Phi \tilde{S}_{IJK} \right) \left[\widetilde{N} \right]_{JK}, \tag{D.10}$$

$$\Delta_p T_i := F_{iI} \Delta_p \hat{S}_{IJ} N_J, \tag{D.11}$$

$$\Delta_\chi R_i := \left(\Delta F_{iI} \tilde{S}_{IJK} + F_{iI} \Delta_\chi \tilde{S}_{IJK} \right) N_J N_K, \tag{D.12}$$

$$\Delta_\Phi R_i := \left(F_{iI} \Delta_\Phi \tilde{S}_{IJK} \right) N_J N_K, \tag{D.13}$$

$$\Delta_\chi J_i := [\![(\Delta F_{iI} \tilde{S}_{IJK} + F_{iI} \Delta_\chi \tilde{S}_{IJK}) \mathfrak{M}_J N_K]\!], \tag{D.14}$$

$$\Delta_\Phi J_i := [\![(F_{iI} \Delta_\Phi \tilde{S}_{IJK}) \mathfrak{M}_J N_K]\!], \tag{D.15}$$

$$\Delta_\chi W := \Bigg(- \Delta_\chi \widehat{D}_L + \Delta_\chi \left(\frac{\partial \widetilde{D}_{LM}}{\partial X_K} \right) \delta_{KM} + \Delta_\chi \left(\frac{\partial \widetilde{D}_{ML}}{\partial X_K} \right) \mathbb{P}_{KM} \Bigg) N_L - \Delta_\chi \widetilde{D}_{LM} \left[\widetilde{N} \right]_{LM}, \tag{D.16}$$

$$\Delta_\Phi W := \left(-\Delta_\Phi \widehat{D}_L + \Delta_\Phi\left(\frac{\partial \widetilde{D}_{LM}}{\partial X_K}\right)\delta_{KM} + \Delta_\Phi\left(\frac{\partial \widetilde{D}_{ML}}{\partial X_K}\right)\mathbb{P}_{KM} \right) N_L - \Delta_\Phi \widetilde{D}_{LM}\left[\widetilde{N}\right]_{LM}, \tag{D.17}$$

$$\Delta_\chi O := -\Delta_\chi \widetilde{D}_{LM} N_L N_M, \tag{D.18}$$

$$\Delta_\Phi O := -\Delta_\Phi \widetilde{D}_{LM} N_L N_M, \tag{D.19}$$

$$\Delta_\chi K := -[\![\Delta_\chi \widetilde{D}_{LM} \mathfrak{M}_L N_M]\!], \tag{D.20}$$

$$\Delta_\Phi K := -[\![\Delta_\Phi \widetilde{D}_{LM} \mathfrak{M}_L N_M]\!], \tag{D.21}$$

where

$$\Delta_\chi \hat{S}_{IJ} := \left(\left(\frac{\partial^2 \bar{\Psi}^{\text{Enth}}}{\partial \mathfrak{E}_{IJ} \partial \mathfrak{E}_{KL}}\right) \Delta \mathfrak{E}_{KL} + \left(\frac{\partial^2 \bar{\Psi}^{\text{Enth}}}{\partial \mathfrak{E}_{IJ} \partial \widetilde{\mathfrak{E}}_{KLM}}\right) \Delta \widetilde{\mathfrak{E}}_{KLM} \right), \tag{D.22}$$

$$\Delta_\chi \tilde{S}_{IJK} := \left(\left(\frac{\partial^2 \bar{\Psi}^{\text{Enth}}}{\partial \mathfrak{E}_{LM} \partial \widetilde{\mathfrak{E}}_{IJK}}\right) \Delta \mathfrak{E}_{LM} + \left(\frac{\partial^2 \bar{\Psi}^{\text{Enth}}}{\partial \widetilde{\mathfrak{E}}_{IJK} \partial \widetilde{\mathfrak{E}}_{LMN}}\right) \Delta \widetilde{\mathfrak{E}}_{LMN} \right), \tag{D.23}$$

$$\Delta_\chi\left(\frac{\partial (F_{iI} \tilde{S}_{IJK})}{\partial X_L}\right) := \Delta \tilde{F}_{iIL} \tilde{S}_{IJK} + \Delta F_{iI} \frac{\partial \tilde{S}_{IJK}}{\partial X_L} + \tilde{F}_{iIL} \Delta_\chi \tilde{S}_{IJK} + F_{iI} \Delta_\chi\left(\frac{\partial \tilde{S}_{IJK}}{\partial X_L}\right), \tag{D.24}$$

$$\frac{\partial \tilde{S}_{IJK}}{\partial X_L} = \left(\frac{\partial^2 \bar{\Psi}^{\text{Enth}}}{\partial \mathfrak{E}_{MN} \partial \widetilde{\mathfrak{E}}_{IJK}}\right) \widetilde{\mathfrak{E}}_{MNL} + \left(\frac{\partial^2 \bar{\Psi}^{\text{Enth}}}{\partial \widetilde{\mathfrak{E}}_{IJK} \partial \widetilde{\mathfrak{E}}_{MNO}}\right) \widetilde{\widetilde{\mathfrak{E}}}_{MNOL} + \left(\frac{\partial^2 \bar{\Psi}^{\text{Enth}}}{\partial \widetilde{\mathfrak{E}}_{IJK} \partial E_M}\right) \tilde{E}_{ML}, \tag{D.25}$$

$$\Delta_\chi\left(\frac{\partial \tilde{S}_{IJK}}{\partial X_L}\right) := \left(\frac{\partial^3 \bar{\Psi}^{\text{Enth}}}{\partial \mathfrak{E}_{OP} \partial \mathfrak{E}_{MN} \partial \widetilde{\mathfrak{E}}_{IJK}}\right) \widetilde{\mathfrak{E}}_{MNL} \Delta \mathfrak{E}_{OP} + \left(\frac{\partial^2 \bar{\Psi}^{\text{Enth}}}{\partial \mathfrak{E}_{MN} \partial \widetilde{\mathfrak{E}}_{IJK}}\right) \Delta \widetilde{\mathfrak{E}}_{MNL} \tag{D.26}$$

$$+ \left(\frac{\partial^2 \bar{\Psi}^{\text{Enth}}}{\partial \widetilde{\mathfrak{E}}_{IJK} \partial \widetilde{\mathfrak{E}}_{MNO}}\right) \Delta \widetilde{\widetilde{\mathfrak{E}}}_{MNOL} + \left(\frac{\partial^3 \bar{\Psi}^{\text{Enth}}}{\partial \mathfrak{E}_{OP} \partial \widetilde{\mathfrak{E}}_{IJK} \partial E_M}\right) \tilde{E}_{ML} \Delta \mathfrak{E}_{OP}, \tag{D.27}$$

$$\Delta_\Phi \hat{S}_{IJ} := \left(\frac{\partial^2 \bar{\Psi}^{\text{Enth}}}{\partial \mathfrak{E}_{IJ} \partial E_L}\right) \Delta E_L + \left(\frac{\partial^2 \bar{\Psi}^{\text{Enth}}}{\partial \mathfrak{E}_{IJ} \partial \tilde{E}_{LM}}\right) \Delta \tilde{E}_{LM}, \tag{D.28}$$

$$\Delta_\Phi \tilde{S}_{IJK} := \left(\frac{\partial^2 \bar{\Psi}^{\text{Enth}}}{\partial \widetilde{\mathfrak{E}}_{IJK} \partial E_L}\right) \Delta E_L, \tag{D.29}$$

$$\Delta_\Phi\left(\frac{\partial \tilde{S}_{IJK}}{\partial X_L}\right) := \left(\frac{\partial^3 \bar{\Psi}^{\text{Enth}}}{\partial \mathfrak{E}_{MN} \partial \widetilde{\mathfrak{E}}_{IJK} \partial E_O}\right) \widetilde{\mathfrak{E}}_{MNL} \Delta E_O + \left(\frac{\partial^2 \bar{\Psi}^{\text{Enth}}}{\partial \widetilde{\mathfrak{E}}_{IJK} \partial E_M}\right) \Delta \tilde{E}_{ML}, \tag{D.30}$$

$$\Delta_p \hat{S}_{IJ} := \left(\frac{\partial^2 \bar{\Psi}^{\text{Enth}}}{\partial \mathfrak{E}_{IJ} \partial p}\right) \Delta p, \tag{D.31}$$

$$\Delta_\chi \widehat{D}_L := -\left(\frac{\partial^2 \bar{\Psi}^{\text{Enth}}}{\partial \mathfrak{E}_{IJ} \partial E_L}\right) \Delta \mathfrak{E}_{IJ} - \left(\frac{\partial^2 \bar{\Psi}^{\text{Enth}}}{\partial \widetilde{\mathfrak{E}}_{IJK} \partial E_L}\right) \Delta \widetilde{\mathfrak{E}}_{IJK}, \tag{D.32}$$

$$\Delta_\chi \widetilde{D}_{LM} := -\left(\frac{\partial^2 \bar{\Psi}^{\text{Enth}}}{\partial \mathfrak{E}_{IJ} \partial \tilde{E}_{LM}}\right) \Delta \mathfrak{E}_{IJ}, \tag{D.33}$$

$$\frac{\partial \widetilde{D}_{LM}}{\partial X_K} = -\left(\frac{\partial^2 \bar{\Psi}^{\text{Enth}}}{\partial \mathfrak{E}_{IJ} \partial \tilde{E}_{LM}}\right) \widetilde{\mathfrak{E}}_{IJK} - \left(\frac{\partial^2 \bar{\Psi}^{\text{Enth}}}{\partial \tilde{E}_{OP} \partial \tilde{E}_{LM}}\right) \tilde{\tilde{E}}_{OPK}, \tag{D.34}$$

$$\Delta_\chi\left(\frac{\partial \widetilde{D}_{LM}}{\partial X_K}\right) := -\left(\frac{\partial^3 \bar{\Psi}^{\text{Enth}}}{\partial \mathfrak{E}_{QR}\partial \mathfrak{E}_{IJ}\partial \tilde{E}_{LM}}\right)\widetilde{\mathfrak{E}}_{IJK}\Delta\mathfrak{E}_{QR} - \left(\frac{\partial^2 \bar{\Psi}^{\text{Enth}}}{\partial \mathfrak{E}_{IJ}\partial \tilde{E}_{LM}}\right)\Delta\widetilde{\mathfrak{E}}_{IJK}, \tag{D.35}$$

$$\Delta_\Phi \widehat{D}_L := -\left(\frac{\partial^2 \bar{\Psi}^{\text{Enth}}}{\partial E_M \partial E_L}\right)\Delta E_M, \tag{D.36}$$

$$\Delta_\Phi \widetilde{D}_{LM} := -\left(\frac{\partial^2 \bar{\Psi}^{\text{Enth}}}{\partial \tilde{E}_{OP}\partial \tilde{E}_{LM}}\right)\Delta\tilde{E}_{OP}, \tag{D.37}$$

$$\Delta_\Phi\left(\frac{\partial \widetilde{D}_{LM}}{\partial X_K}\right) := -\left(\frac{\partial^2 \bar{\Psi}^{\text{Enth}}}{\partial \tilde{E}_{OP}\partial \tilde{E}_{LM}}\right)\Delta\tilde{\tilde{E}}_{OPK}. \tag{D.38}$$

In the equations above, we have introduced the second gradients of deformation given by

$$\tilde{\tilde{F}}_{iJKL} := \frac{\partial \tilde{F}_{iJK}}{\partial X_L} = \frac{\partial^3 \chi_i}{\partial X_J \partial X_K \partial X_L}, \quad \tilde{\tilde{C}}_{IJKL} := \frac{\partial \widetilde{C}_{IJK}}{\partial X_L} = 2\operatorname*{symm}_{IJ}\left(\tilde{\tilde{F}}_{kIKL}F_{kJ} + \tilde{F}_{kIK}\tilde{F}_{kJL}\right),$$
$$\tilde{\tilde{\mathfrak{E}}}_{IJKL} := \frac{\partial \widetilde{\mathfrak{E}}_{IJK}}{\partial X_L} = \frac{1}{2}\tilde{\tilde{C}}_{IJKL}, \tag{D.39}$$

and the second gradient of the nominal electric field given by

$$\tilde{\tilde{E}}_{IJK} := \frac{\partial \tilde{E}_{IJ}}{\partial X_K} = -\frac{\partial^3 \Phi}{\partial X_I \partial X_J \partial X_K}. \tag{D.40}$$

The derivatives of enthalpy are explicitly derived in E. Note that in the numerical implementation of the variation of the interface residual functional, similar to (Rüberg *et al.*, 2016) the terms containing $(\Delta\delta)T_i$, $(\Delta\delta)R_i$, $(\Delta\delta)W$, $(\Delta\delta)O$, $(\Delta\delta)J_i$ and $(\Delta\delta)K$ in Eq. (D.4) have been neglected, since consideration of these terms are very computationally expensive.

E Derivatives of the enthalpy

The derivatives of enthalpy $\bar{\Psi}^{\text{Enth}} = \Psi^{\text{Enth}} + p(J-1)$ can be derived as follows

$$\hat{S}_{IJ} := \frac{\partial \bar{\Psi}^{\text{Enth}}}{\partial \mathfrak{E}_{IJ}} = G(\delta_{IJ} - C_{IJ}^{-1}) + pJC_{IJ}^{-1} + \frac{J}{2}\mathscr{C}_{MLIJ}\left(\epsilon E_L E_M + \mu_{LABK}E_M\widetilde{\mathfrak{E}}_{ABK} - \mu_{LABK}\tilde{E}_{MK}\mathfrak{E}_{AB}\right) + \frac{1}{2}JC_{AB}^{-1}\mu_{AIJK}\tilde{E}_{BK}, \tag{E.1}$$

$$\tilde{S}_{IJK} := \frac{\partial \bar{\Psi}^{\text{Enth}}}{\partial \widetilde{\mathfrak{E}}_{IJK}} = h_{IJKLMN}\widetilde{\mathfrak{E}}_{LMN} - \frac{1}{2}JC_{LM}^{-1}E_M\mu_{LIJK}, \tag{E.2}$$

$$-\widehat{D}_L := \frac{\partial \bar{\Psi}^{\text{Enth}}}{\partial E_L} = -JC_{KL}^{-1}\left(\epsilon E_K + \frac{1}{2}\mu_{KIJM}\widetilde{\mathfrak{E}}_{IJM}\right), \tag{E.3}$$

$$-\widetilde{D}_{LM} := \frac{\partial \bar{\Psi}^{\text{Enth}}}{\partial \tilde{E}_{LM}} = \frac{1}{2}JC_{AL}^{-1}\mu_{AIJM}\mathfrak{E}_{IJ} - \tilde{E}_{IJ}M_{IJLM}, \tag{E.4}$$

$$\frac{\partial^2 \bar{\Psi}^{\text{Enth}}}{\partial \mathfrak{E}_{XY}\partial \mathfrak{E}_{PQ}} = G(C_{XP}^{-1}C_{YQ}^{-1} + C_{XQ}^{-1}C_{YP}^{-1}) - pJ\mathscr{C}_{XYPQ} + \frac{J}{2}\widetilde{\mathscr{C}}_{MNXYPQ}\epsilon E_M E_N \tag{E.5}$$

$$+ \frac{J}{2}\widetilde{\mathscr{C}}_{MNXYPQ}\mu_{MIJK}(E_N\widetilde{\mathfrak{E}}_{IJK} - \tilde{E}_{NK}\mathfrak{E}_{IJ}) - \frac{J}{2}\tilde{E}_{NK}(\mathscr{C}_{MNXY}\mu_{MPQK} + \mathscr{C}_{MNPQ}\mu_{MXYK}), \tag{E.6}$$

$$\frac{\partial^2 \bar{\Psi}^{\text{Enth}}}{\partial \widetilde{\mathfrak{E}}_{IJK}\partial \widetilde{\mathfrak{E}}_{LMN}} = h_{IJKLMN}, \tag{E.7}$$

$$\frac{\partial^2 \bar{\Psi}^{\text{Enth}}}{\partial E_L \partial E_M} = -\epsilon JC_{LM}^{-1}, \tag{E.8}$$

$$\frac{\partial^2 \bar{\Psi}^{\text{Enth}}}{\partial \tilde{E}_{LK}\partial \tilde{E}_{MN}} = -M_{LKMN}, \tag{E.9}$$

$$\frac{\partial^2 \bar{\Psi}^{\text{Enth}}}{\partial \mathfrak{E}_{IJ}\partial \widetilde{\mathfrak{E}}_{ABK}} = \frac{J}{2}\mathscr{C}_{MLIJ}\mu_{LABK}E_M, \tag{E.10}$$

$$\frac{\partial^2 \bar{\Psi}^{\text{Enth}}}{\partial \mathfrak{E}_{IJ}\partial E_L} = J\mathscr{C}_{KLIJ}\left(\epsilon E_K + \frac{1}{2}\mu_{KABC}\widetilde{\mathfrak{E}}_{ABC}\right), \tag{E.11}$$

$$\frac{\partial^2 \bar{\Psi}^{\text{Enth}}}{\partial \mathfrak{E}_{IJ}\partial \tilde{E}_{MK}} = \frac{1}{2}JC_{AM}^{-1}\mu_{AIJK} - \frac{J}{2}\mathscr{C}_{MLIJ}\mu_{LABK}\mathfrak{E}_{AB}, \tag{E.12}$$

$$\frac{\partial^2 \bar{\Psi}^{\text{Enth}}}{\partial \mathfrak{E}_{IJ}\partial p} = JC_{IJ}^{-1}, \tag{E.13}$$

$$\frac{\partial^2 \bar{\Psi}^{\text{Enth}}}{\partial \widetilde{\mathfrak{E}}_{IJK}\partial E_M} = -\frac{1}{2}JC_{LM}^{-1}\mu_{LIJK}, \tag{E.14}$$

$$\frac{\partial^3 \bar{\Psi}^{\text{Enth}}}{\partial \mathfrak{E}_{XY}\partial \mathfrak{E}_{PQ}\partial \widetilde{\mathfrak{E}}_{IJK}} = \frac{J}{2}\widetilde{\mathscr{C}}_{MNXYPQ}\mu_{MIJK}E_N, \tag{E.15}$$

$$\frac{\partial^3 \bar{\Psi}^{\text{Enth}}}{\partial \mathfrak{E}_{IJ} \partial \widetilde{\mathfrak{E}}_{ABK} \partial E_M} = \frac{J}{2} \mathscr{C}_{MLIJ} \mu_{LABK}, \tag{E.16}$$

$$\frac{\partial^3 \bar{\Psi}^{\text{Enth}}}{\partial \mathfrak{E}_{XY} \partial \mathfrak{E}_{PQ} \partial \tilde{E}_{NK}} = -\frac{J}{2} \widetilde{\mathscr{C}}_{MNXYPQ} \mu_{MIJK} \mathfrak{E}_{IJ} - \frac{J}{2} (\mathscr{C}_{MNXY} \mu_{MPQK} + \mathscr{C}_{MNPQ} \mu_{MXYK}), \tag{E.17}$$

with

$$\mathscr{C}_{ABCD} := -\frac{2}{J} \frac{\partial \left(J C_{AB}^{-1} \right)}{\partial C_{CD}} = \left(C_{AC}^{-1} C_{BD}^{-1} + C_{BC}^{-1} C_{AD}^{-1} - C_{AB}^{-1} C_{CD}^{-1} \right), \tag{E.18}$$

$$\widetilde{\mathscr{C}}_{ABCDEF} := \frac{2}{J} \frac{\partial \left(J \mathscr{C}_{ABCD} \right)}{\partial C_{EF}} = (\mathbb{D}_{ACBDEF} + \mathbb{D}_{BDACEF} + \mathbb{D}_{ADBCEF} + \mathbb{D}_{BCADEF} - \mathbb{D}_{ABCDEF} - \mathbb{D}_{CDABEF}), \tag{E.19}$$

where $\mathbb{D}_{ABCDEF} := C_{AB}^{-1} \left(\frac{1}{2} C_{CD}^{-1} C_{EF}^{-1} - C_{CE}^{-1} C_{DF}^{-1} - C_{CF}^{-1} C_{DE}^{-1} \right)$.

F Assessment of the equivalence of the flexoelectric models based on internal energy and electromechanical enthalpy

In a flexoelectric continuum, neglecting the term quadratic to polarization gradient for simplicity, the Lagrangian internal energy density per unit undeformed volume can be written as

$$\tilde{\Psi}^{\text{Int}}(\mathfrak{E}, \widetilde{\mathfrak{E}}, \boldsymbol{P}, \tilde{\boldsymbol{P}}) = \Psi^{\text{Elast}}(\mathfrak{E}) + \Psi^{\text{SGEla}}(\widetilde{\mathfrak{E}}) + \tilde{\Psi}^{\text{Diele}}(\mathfrak{E}, \boldsymbol{P}) + \tilde{\Psi}^{\text{Flexo}}(\mathfrak{E}, \widetilde{\mathfrak{E}}, \boldsymbol{P}, \tilde{\boldsymbol{P}}) \tag{F.1}$$

where Ψ^{Elast} and Ψ^{SGEla} have been defined in Eq. (2.49) and Eq. (2.50), respectively. The isotropic dielectric energy density per unit undeformed volume (Codony *et al.*, 2020) can be expressed as

$$\tilde{\Psi}^{\text{Diele}}(\mathfrak{E}, \boldsymbol{P}) = \frac{1}{2J(\epsilon - \epsilon_0)} P_I C_{IJ} P_J, \tag{F.2}$$

where ϵ_0 is the electric permittivity of vacuum. One can postulate a flexoelectric energy density per unit undeformed volume which explicitly takes into the account the direct and the converse flexoelectricity as

$$\tilde{\Psi}^{\text{Flexo}}(\mathfrak{E}, \widetilde{\mathfrak{E}}, \boldsymbol{P}, \tilde{\boldsymbol{P}}) = -\frac{1}{2} f_{LIJK} \left(P_L \widetilde{\mathfrak{E}}_{IJK} - \tilde{P}_{LK} \mathfrak{E}_{IJ} \right), \tag{F.3}$$

where $\boldsymbol{f}$ is a Lagrangian tensor discussed in detail in (Codony *et al.*, 2020). A partial Legendre transformation can be employed to find an internal energy density in terms of $\boldsymbol{E}$ and $\tilde{\boldsymbol{E}}$ as

$$\Psi^{\text{Int}}(\mathfrak{E}, \widetilde{\mathfrak{E}}, \boldsymbol{E}, \tilde{\boldsymbol{E}}) = \min_{\boldsymbol{P}, \tilde{\boldsymbol{P}}} (\tilde{\Psi}^{\text{Int}}(\mathfrak{E}, \widetilde{\mathfrak{E}}, \boldsymbol{P}, \tilde{\boldsymbol{P}}) - \boldsymbol{P}.\boldsymbol{E}). \tag{F.4}$$

The associated stationary conditions of minimization result in definition of the following variables

$$\check{E}_L = \frac{\partial \tilde{\Psi}^{\text{Int}}}{\partial P_L} = \frac{1}{J(\epsilon - \epsilon_0)} C_{LJ} P_J - \frac{1}{2} f_{LIJK} \widetilde{\mathfrak{E}}_{IJK} \tag{F.5}$$

$$\check{E}_{LK} = \frac{\partial \tilde{\Psi}^{\text{Int}}}{\partial \tilde{P}_{LK}} = \frac{1}{2} f_{LIJK} \mathfrak{E}_{IJ}. \tag{F.6}$$

The nominal electric field and its gradient can be expressed as

$$E_L = \check{E}_L - \check{E}_{LK,K} = \check{E}_L - \frac{1}{2} f_{LIJK} \widetilde{\mathfrak{E}}_{IJK} \tag{F.7}$$

$$\tilde{E}_{LM} = E_{L,M} = \frac{\partial \left(\check{E}_L - \frac{1}{2} f_{LIJK} \widetilde{\mathfrak{E}}_{IJK} \right)}{\partial X_M} \tag{F.8}$$

Invoking Eq. (F.5) results in finding $\boldsymbol{P}$ and its gradient $\tilde{\boldsymbol{P}}$ as

$$P_M = JC^{-1}_{ML}(\epsilon - \epsilon_0)\left(\check{E}_L + \frac{1}{2}f_{LIJK}\widetilde{\mathfrak{E}}_{IJK}\right) \tag{F.9}$$

$$\tilde{P}_{MK} = \frac{\partial P_J}{\partial X_K} = \frac{\partial (JC^{-1}_{ML})}{\partial X_K}(\epsilon - \epsilon_0)\left(\check{E}_L + \frac{1}{2}f_{LIJK}\widetilde{\mathfrak{E}}_{IJK}\right) + JC^{-1}_{ML}(\epsilon - \epsilon_0)\frac{\partial\left(\check{E}_L + \frac{1}{2}f_{LIJK}\widetilde{\mathfrak{E}}_{IJK}\right)}{\partial X_K} \tag{F.10}$$

Substituting Eq. (F.7), Eq. (F.9) and Eq. (F.10) in Eq. (F.4) and invoking Eq. (F.8) result in

$$\begin{aligned}\Psi^{\text{Int}}(\mathfrak{E}, \widetilde{\mathfrak{E}}, \boldsymbol{E}, \tilde{\boldsymbol{E}}) =& \Psi^{\text{Elast}}(\mathfrak{E}) + \Psi^{\text{SGEla}}(\widetilde{\mathfrak{E}}) - \frac{1}{2}J(\epsilon - \epsilon_0)E_K C^{-1}_{KL}E_L - \frac{1}{2}JC^{-1}_{AB}(\epsilon - \epsilon_0)f_{AIJK}E_B\widetilde{\mathfrak{E}}_{IJK} \\ &+ \frac{1}{2}JC^{-1}_{AB}(\epsilon - \epsilon_0)f_{AIJK}\tilde{E}_{BK}\mathfrak{E}_{IJ} + \frac{1}{2}\frac{\partial (JC^{-1}_{ML})}{\partial X_K}(\epsilon - \epsilon_0)f_{LIJK}\mathfrak{E}_{IJ}(E_M + f_{MABC}\widetilde{\mathfrak{E}}_{ABC}) \\ &\frac{1}{2}JC^{-1}_{ML}(\epsilon - \epsilon_0)f_{LIJK}\mathfrak{E}_{IJ}f_{MABC}\frac{\partial \widetilde{\mathfrak{E}}_{ABC}}{\partial X_K}\end{aligned} \tag{F.11}$$

The total electromechanical enthalpy including electrostatic energy density (Codony *et al.*, 2020) can be written as

$$\begin{aligned}\Psi^{\text{Enth}^*} = \Psi^{\text{Int}} - \frac{1}{2}J\epsilon_0 E_K C^{-1}_{KL}E_L =& \Psi^{\text{Elast}}(\mathfrak{E}) + \Psi^{\text{SGEla}}(\widetilde{\mathfrak{E}}) - \frac{1}{2}J\epsilon E_K C^{-1}_{KL}E_L - \frac{1}{2}JC^{-1}_{AB}\mu_{AIJK}E_B\widetilde{\mathfrak{E}}_{IJK} \\ &+ \frac{1}{2}JC^{-1}_{AB}\mu_{AIJK}\tilde{E}_{BK}\mathfrak{E}_{IJ} + \frac{1}{2}\frac{\partial (JC^{-1}_{ML})}{\partial X_K}\mu_{LIJK}\mathfrak{E}_{IJ}(E_M + f_{MABC}\widetilde{\mathfrak{E}}_{ABC}) \\ &\frac{1}{2}JC^{-1}_{ML}\mu_{LIJK}\mathfrak{E}_{IJ}f_{MABC}\frac{\partial \widetilde{\mathfrak{E}}_{ABC}}{\partial X_K}\end{aligned} \tag{F.12}$$

where $\mu = (\epsilon - \epsilon_0)\boldsymbol{f}$ is the flexoelectric tensor. Note that the last term will vanish since it involves a higher-order measure of deformation. Comparing Eq. (F.12) with Eq. (2.48), it can be observed that both models incorporate similar flexoelectric terms. Eq. (F.12) involves an additional term (sixth term) which we do not consider in our model.

G Modeling pre-deformation

To mathematically model the pre-deformation, let us consider a deformable continuum body denoted by Ω_0 in the undeformed configuration, by Ω_p in the pre-deformed configuration, and by Ω in the deformed configuration. The deformation map $\boldsymbol{\chi_p} : \Omega_0 \longrightarrow \Omega_p$ carries every point $\boldsymbol{X} \in \Omega_0$ to a point $\boldsymbol{x}_p = \boldsymbol{\chi_p}(\boldsymbol{X}) \in \Omega_p$, $\mathbf{F}_p$ being its deformation gradient. Similarly, the deformation map $\boldsymbol{\chi} : \Omega_p \longrightarrow \Omega$ carries every point $\boldsymbol{x}_p \in \Omega_p$ to a point $\boldsymbol{x} = \boldsymbol{\chi}(\boldsymbol{x}_p) \in \Omega$, $\mathbf{F}$ being its deformation gradient. Note that the total deformation gradient between undeformed and deformed configurations can be written as $\mathbf{F}_{tot} = \mathbf{F}.\mathbf{F}_p$. The energy used for two consecutive deformations must be equal to that of the total deformation which yields

$$\begin{aligned}\int_{\Omega_0} \bar{\Psi}^{\text{Enth}}(\mathfrak{E}_{tot}, \widetilde{\mathfrak{E}}, \boldsymbol{E}, \tilde{\boldsymbol{E}}, p)\, \mathrm{d}\Omega_0 &= \int_{\Omega_0} \bar{\Psi}^{\text{Enth}}(\mathfrak{E}_p, 0, 0, 0, 0)\, \mathrm{d}\Omega_0 + \int_{\Omega_p} \bar{\Psi}_p^{\text{Enth}}(\mathfrak{E}, \widetilde{\mathfrak{E}}, \boldsymbol{E}, \tilde{\boldsymbol{E}}, p)\, \mathrm{d}\Omega_p \\ &= \int_{\Omega_0} \bar{\Psi}^{\text{Enth}}(\mathfrak{E}_p, 0, 0, 0, 0)\, \mathrm{d}\Omega_0 + \int_{\Omega_p} \bar{\Psi}_p^{\text{Enth}}(\mathfrak{E}, \widetilde{\mathfrak{E}}, \boldsymbol{E}, \tilde{\boldsymbol{E}}, p) J_p\, \mathrm{d}\Omega_0\end{aligned} \tag{G.1}$$

where $\mathfrak{E}_{tot}$ and $\mathfrak{E}_p$ are the Green-Lagrange strains resulting from $\mathbf{F}_{tot}$ and $\mathbf{F}_p$, respectively, $J_p := \det(\mathbf{F}_p)$, and $\bar{\Psi}^{\text{Enth}} = \Psi^{\text{Enth}} + p(J-1)$. Therefore, the enthalpy density of the pre-deformed state can be written as:

$$\bar{\Psi}_p^{\text{Enth}}(\mathfrak{E}, \widetilde{\mathfrak{E}}, \boldsymbol{E}, \tilde{\boldsymbol{E}}, p) = \frac{1}{J_p}\left(\bar{\Psi}^{\text{Enth}}(\mathfrak{E}_{tot}, \widetilde{\mathfrak{E}}, \boldsymbol{E}, \tilde{\boldsymbol{E}}, p) - \bar{\Psi}^{\text{Enth}}(\mathfrak{E}_p, 0, 0, 0, 0)\right) \tag{G.2}$$

Therefore:

$$\frac{\partial \bar{\Psi}_p^{\text{Enth}}(\mathfrak{E}, \widetilde{\mathfrak{E}}, \boldsymbol{E}, \tilde{\boldsymbol{E}}, p)}{\partial \mathfrak{E}} = \frac{1}{J_p}\left(\frac{\partial \bar{\Psi}^{\text{Enth}}(\mathfrak{E}_{tot}, \widetilde{\mathfrak{E}}, \boldsymbol{E}, \tilde{\boldsymbol{E}}, p)}{\partial \mathfrak{E}}\right) = \frac{1}{J_p}\left(\frac{\partial \bar{\Psi}^{\text{Enth}}(\mathfrak{E}_{tot})}{\partial \mathfrak{E}_{tot}} \frac{\partial \mathfrak{E}_{tot}}{\partial \mathfrak{E}}\right). \tag{G.3}$$

Similarly, other required derivatives can be obtained.

H Analytical derivation for the case of electrical actuation of a thin flexoelectric film along its length

Consider a thin flexoelectric film along the x-direction occupying $[-T/2, T/2]$ in the y-coordinate. Suppose we apply far-field horizontal electric field $\bar{E}_x$ to the system. Consequently, the applied electric field results in y-dependent shear strain $\varepsilon_{xy}(y) = \varepsilon_{yx}(y)$. Note that $\varepsilon_{xx} = \varepsilon_{yy} = 0$ and $E_y = 0$. Therefore:

$$\boldsymbol{\varepsilon} = \begin{bmatrix} 0 & \varepsilon_{xy}(y) \\ \varepsilon_{xy}(y) & 0 \end{bmatrix}, \qquad \boldsymbol{E} = \begin{bmatrix} \bar{E}_x \\ 0 \end{bmatrix}. \tag{H.1}$$

Accordingly, components of the constitutive equations can be written as:

$$\hat{\sigma}_{xy} = \hat{\sigma}_{yx} = 2C_S\varepsilon_{xy}(y), \tag{H.2}$$
$$\hat{\sigma}_{xx} = \hat{\sigma}_{yy} = 0, \tag{H.3}$$

$$\tilde{\sigma}_{xyy} = \tilde{\sigma}_{yxy} = 2C_S l_1^2 \varepsilon_{xy,y} - 2(1-\zeta)\mu_S \bar{E}_x, \tag{H.4}$$
$$\tilde{\sigma}_{xxx} = -(1-\zeta)\mu_L \bar{E}_x, \tag{H.5}$$
$$\tilde{\sigma}_{yyx} = -(1-\zeta)\mu_T \bar{E}_x, \tag{H.6}$$
$$\tilde{\sigma}_{yyy} = \tilde{\sigma}_{xyx} = \tilde{\sigma}_{yxx} = \tilde{\sigma}_{xxy} = 0, \tag{H.7}$$

$$\hat{D}_x = \epsilon\bar{E}_x + 2(1-\zeta)\mu_S\varepsilon_{xy,y}(y), \tag{H.8}$$
$$\hat{D}_y = 0, \tag{H.9}$$

$$\widetilde{D}_{xy} = \widetilde{D}_{yx} = -2\zeta\mu_S\varepsilon_{xy}(y), \tag{H.10}$$
$$\widetilde{D}_{xx} = \widetilde{D}_{yy} = 0. \tag{H.11}$$

Therefore, the components of physical stress and physical electric displacement are:

$$\sigma_{xy} = \sigma_{yx} = 2C_S\varepsilon_{xy}(y) - 2C_S l_1^2 \varepsilon_{xy,yy}(y), \tag{H.12}$$
$$\sigma_{xx} = \sigma_{yy} = 0, \tag{H.13}$$

$$D_x = \epsilon\bar{E}_x + 2\mu_S\varepsilon_{xy,y}(y) \tag{H.14}$$
$$D_y = 0. \tag{H.15}$$

Therefore, the following equilibrium equation in the y-direction is the only non-trivial

equation that needs to be satisfied:

$$2C_S\varepsilon_{xy,y}(y) - 2l_1^2 C_S\varepsilon_{xy,yyy}(y) = 0, \tag{H.16}$$

Note that the electrical equilibrium equation and its associated boundary conditions in the y-direction are trivially satisfied. The solution of the ODE (H.16) must then satisfy the following non-trivial boundary condition that is the homogeneous Neumann boundary condition related to double traction (Eq. (2.23)):

$$2l_1^2 C_S\varepsilon_{xy,y}(y) - 2(1-\zeta)\mu_S\bar{E}_x = 0, \quad \text{on} \quad y = \{-T/2, T/2\}. \tag{H.17}$$

Note that the low-order mechanical boundary condition (Eq. (2.22)) in the y-direction is also trivially satisfied. The following is the solution for the above ODE (H.16) satisfying Eq. (H.17):

$$\varepsilon_{xy}(y) = \frac{-(1-\zeta)\mu_S\bar{E}_x}{(1+\exp(-T/l_1))\, C_S l_1}\left[\exp\left(\frac{-y-T/2}{l_1}\right) - \exp\left(\frac{y-T/2}{l_1}\right)\right]. \tag{H.18}$$

I Analytical derivation for the case of in-plane compression of a thin flexoelectric film along its length

Consider a thin flexoelectric film along the x-direction occupying $[-T/2, T/2]$ in the y-coordinate. Suppose we apply far-field plane-strain horizontal compression $\bar{\varepsilon}_{xx}$ to the system. Both the deformation field and electric potential are independent of x-direction. Therefore, the applied compression results in y-dependent vertical strain $\varepsilon_{yy}(y)$ and electric field $E_y(y)$. Note that $\varepsilon_{xy} = \varepsilon_{yx} = 0$ and $E_x = 0$. Therefore:

$$\boldsymbol{\varepsilon} = \begin{bmatrix} \bar{\varepsilon}_{xx} & 0 \\ 0 & \varepsilon_{yy}(y) \end{bmatrix}, \qquad \boldsymbol{E} = \begin{bmatrix} 0 \\ E_y(y) \end{bmatrix}. \tag{I.1}$$

Accordingly, components of the constitutive equations can be written as:

$$\hat{\sigma}_{xx} = C_L\bar{\varepsilon}_{xx} + C_T\varepsilon_{yy}(y) + \zeta\mu_T E_{y,y}(y), \tag{I.2}$$
$$\hat{\sigma}_{yy} = C_T\bar{\varepsilon}_{xx} + C_L\varepsilon_{yy}(y) + \zeta\mu_L E_{y,y}(y), \tag{I.3}$$
$$\hat{\sigma}_{xy} = \hat{\sigma}_{yx} = 0, \tag{I.4}$$

$$\tilde{\sigma}_{yyy} = l_1^2 C_L\varepsilon_{yy,y}(y) - (1-\zeta)\mu_L E_y(y), \tag{I.5}$$
$$\tilde{\sigma}_{xyx} = \tilde{\sigma}_{yxx} = -(1-\zeta)\mu_S E_y(y), \tag{I.6}$$
$$\tilde{\sigma}_{xxy} = l_1^2 C_T\varepsilon_{yy,y}(y) - (1-\zeta)\mu_T E_y(y), \tag{I.7}$$
$$\tilde{\sigma}_{xxx} = \tilde{\sigma}_{xyy} = \tilde{\sigma}_{yyx} = \tilde{\sigma}_{yxy} = 0, \tag{I.8}$$

$$\hat{D}_y = \epsilon E_y(y) + (1-\zeta)\mu_L \varepsilon_{yy,y}(y), \tag{I.9}$$
$$\hat{D}_x = 0, \tag{I.10}$$

$$\widetilde{D}_{xx} = -\zeta\mu_L \bar{\varepsilon}_{xx} - \zeta\mu_T \varepsilon_{yy}(y), \tag{I.11}$$
$$\widetilde{D}_{yy} = l_2^2 \epsilon E_{y,y}(y) - \zeta\mu_L \varepsilon_{yy}(y) - \zeta\mu_T \bar{\varepsilon}_{xx}, \tag{I.12}$$
$$\widetilde{D}_{xy} = \widetilde{D}_{yx} = 0. \tag{I.13}$$

Therefore, the components of physical stress and physical electric displacement are:

$$\sigma_{xx} = C_L \bar{\varepsilon}_{xx} + C_T \varepsilon_{yy}(y) + \mu_T E_{y,y}(y) - l_1^2 C_T \varepsilon_{yy,yy}(y), \tag{I.14}$$
$$\sigma_{yy} = C_T \bar{\varepsilon}_{xx} + C_L \varepsilon_{yy}(y) + \mu_L E_{y,y}(y) - l_1^2 C_L \varepsilon_{yy,yy}(y), \tag{I.15}$$
$$\sigma_{xy} = \sigma_{yx} = 0, \tag{I.16}$$

$$D_y = \epsilon E_y(y) + \mu_L \varepsilon_{yy,y}(y) - l_2^2 \epsilon E_{y,yy}(y), \tag{I.17}$$
$$D_x = 0. \tag{I.18}$$

Therefore, equilibrium equations in y-direction read:

$$C_L \varepsilon_{yy,y}(y) + \mu_L E_{y,yy}(y) - l_1^2 C_L \varepsilon_{yy,yyy}(y) = 0, \tag{I.19}$$
$$\epsilon E_{y,y}(y) + \mu_L \varepsilon_{yy,yy}(y) - l_2^2 \epsilon E_{y,yyy}(y) = 0, \tag{I.20}$$

subjected to high-order homogeneous Neumann boundary conditions (Eqs. (2.23), (2.25)):

$$l_1^2 C_L \varepsilon_{yy,y}(y) - (1-\zeta)\mu_L E_y(y) = 0, \quad \text{on} \quad y = \{-T/2, T/2\}, \tag{I.21}$$
$$l_2^2 \epsilon E_{y,y}(y) - \zeta\mu_L \varepsilon_{yy}(y) - \zeta\mu_T \bar{\varepsilon}_{xx} = 0, \quad \text{on} \quad y = \{-T/2, T/2\}. \tag{I.22}$$

The low-order homogeneous Neumann boundary conditions (Eqs. (2.22),(2.24)) will naturally be satisfied with the solution we will postulate.

Extracting $E_{y,y}$ and $\varepsilon_{yy,y}$ from (I.15) and (I.17), respectively, and replacing them into (I.19) and (I.20), respectively, we obtain:

$$(l_1^2 l_2^2) E_{y,yyyy}(y) - (l_1^2 + l_2^2 + l_\mu^2) E_{y,yy}(y) + E_y(y) = \frac{D_y - l_1^2 D_{y,yy}}{\epsilon}, \tag{I.23}$$
$$(l_1^2 l_2^2) \varepsilon_{yy,yyyy}(y) - (l_1^2 + l_2^2 + l_\mu^2) \varepsilon_{yy,yy}(y) + \varepsilon_{yy}(y) = \frac{\sigma_{yy} - l_2^2 \sigma_{yy,yy}}{C_L} - \frac{C_T}{C_L} \bar{\varepsilon}_{xx}. \tag{I.24}$$

where $l_\mu^2 = \frac{\mu_L^2}{C_L \epsilon}$.

One can postulate the solutions to be of the form:

$$E_y = k_1 \exp\left(\frac{-y - T/2}{a_1}\right) + k_2 \exp\left(\frac{-y - T/2}{a_2}\right) + k_3 \exp\left(\frac{y - T/2}{a_1}\right) + k_4 \exp\left(\frac{y - T/2}{a_2}\right), \tag{I.25}$$

$$\varepsilon_{yy}(y) = k_5 \exp\left(\frac{-y - T/2}{a_1}\right) + k_6 \exp\left(\frac{-y - T/2}{a_2}\right) + k_7 \exp\left(\frac{y - T/2}{a_1}\right) + k_8 \exp\left(\frac{y - T/2}{a_2}\right) - \frac{C_T}{C_L}\bar{\varepsilon}_{xx}, \tag{I.26}$$

for $y \in [-T/2, T/2]$, with:

$$a_1, a_2 = \sqrt{\frac{2l_1^2 l_2^2}{l_1^2 + l_2^2 + l_\mu^2 \pm \sqrt{(l_1^2 + l_2^2 + l_\mu^2)^2 - 4l_1^2 l_2^2}}}. \tag{I.27}$$

Note that $k_1 = -k_3$, $k_2 = -k_4$, $k_5 = k_7$, $k_6 = k_8$ due to symmetry. Substituting the E_y and ε_{yy} from Eqs. (I.25) and (I.26) to Eqs. (I.19), (I.20), (I.21) and (I.22), we obtain the unknowns k_i.

$$k_1 = -k_3 = \frac{-\beta_2 \bar{\varepsilon}_{xx} \zeta (C_L \mu_T - C_T \mu_L)}{C_L \epsilon (a_1 \beta_2 \gamma_1 - a_2 \beta_1 \gamma_2)}, \tag{I.28}$$

$$k_2 = -k_4 = \frac{\beta_1 \bar{\varepsilon}_{xx} \zeta (C_L \mu_T - C_T \mu_L)}{C_L \epsilon (a_1 \beta_2 \gamma_1 - a_2 \beta_1 \gamma_2)}, \tag{I.29}$$

$$k_5 = k_7 = \frac{-a_1 \alpha_1 \beta_2 \bar{\varepsilon}_{xx} \zeta (C_L \mu_T - C_T \mu_L)}{C_L \mu_L (a_1 \beta_2 \gamma_1 - a_2 \beta_1 \gamma_2)}, \tag{I.30}$$

$$k_6 = k_8 = \frac{a_2 \alpha_2 \beta_1 \bar{\varepsilon}_{xx} \zeta (C_L \mu_T - C_T \mu_L)}{C_L \mu_L (a_1 \beta_2 \gamma_1 - a_2 \beta_1 \gamma_2)}. \tag{I.31}$$

where

$$\alpha_i = 1 - \frac{l_2^2}{a_i^2}, \tag{I.32}$$

$$\beta_i = (1 - \exp(-T/a_i)) \left(\frac{l_1^2}{l_\mu^2}\alpha_i + 1 - \zeta\right), \tag{I.33}$$

$$\gamma_i = (1 + \exp(-T/a_i)) \left(\frac{l_2^2}{a_i^2}(1 - \zeta) + \zeta\right). \tag{I.34}$$

J Analytical derivation for the case of uniform bending of a slender beam

Consider thin flexoelectric film along the x-direction occupying $[-T/2, T/2]$ in the y-coordinate. The beam is uniformly bent so that the curvature of the beam κ is the same in all cross-sections normal to it. Following a slender beam approximation, the strains and electric fields can be

written as:

$$\boldsymbol{\varepsilon} = \begin{bmatrix} -\kappa y & 0 \\ 0 & \varepsilon_{yy}(y) \end{bmatrix}, \qquad \boldsymbol{E} = \begin{bmatrix} 0 \\ E_y(y) \end{bmatrix}. \tag{J.1}$$

Accordingly, components of the constitutive equations can be written as:

$$\hat{\sigma}_{xx} = -C_L \kappa y + C_T \varepsilon_{yy}(y) + \zeta \mu_T E_{y,y}(y), \tag{J.2}$$
$$\hat{\sigma}_{yy} = -C_T \kappa y + C_L \varepsilon_{yy}(y) + \zeta \mu_L E_{y,y}(y), \tag{J.3}$$
$$\hat{\sigma}_{xy} = \hat{\sigma}_{yx} = 0, \tag{J.4}$$

$$\tilde{\sigma}_{yyy} = l_1^2 C_L \varepsilon_{yy,y}(y) - (1-\zeta)\mu_L E_y(y) - l_1^2 C_T \kappa, \tag{J.5}$$
$$\tilde{\sigma}_{xyx} = \tilde{\sigma}_{yxx} = -(1-\zeta)\mu_S E_y(y), \tag{J.6}$$
$$\tilde{\sigma}_{xxy} = l_1^2 C_T \varepsilon_{yy,y}(y) - (1-\zeta)\mu_T E_y(y) - l_1^2 C_L \kappa, \tag{J.7}$$
$$\tilde{\sigma}_{xxx} = \tilde{\sigma}_{xyy} = \tilde{\sigma}_{yyx} = \tilde{\sigma}_{yxy} = 0, \tag{J.8}$$

$$\hat{D}_y = \epsilon E_y(y) + (1-\zeta)\mu_L \varepsilon_{yy,y}(y) - (1-\zeta)\mu_T \kappa, \tag{J.9}$$
$$\hat{D}_x = 0, \tag{J.10}$$

$$\widetilde{D}_{xx} = \zeta \mu_L \kappa y - \zeta \mu_T \varepsilon_{yy}(y), \tag{J.11}$$
$$\widetilde{D}_{yy} = l_2^2 \epsilon E_{y,y}(y) - \zeta \mu_L \varepsilon_{yy}(y) + \zeta \mu_T \kappa y, \tag{J.12}$$
$$\widetilde{D}_{xy} = \widetilde{D}_{yx} = 0. \tag{J.13}$$

Therefore, the components of physical stress and physical electric displacement are:

$$\sigma_{xx} = -C_L \kappa y + C_T \varepsilon_{yy}(y) + \mu_T E_{y,y}(y) - l_1^2 C_T \varepsilon_{yy,yy}(y), \tag{J.14}$$
$$\sigma_{yy} = -C_T \kappa y + C_L \varepsilon_{yy}(y) + \mu_L E_{y,y}(y) - l_1^2 C_L \varepsilon_{yy,yy}(y), \tag{J.15}$$
$$\sigma_{xy} = \sigma_{yx} = 0, \tag{J.16}$$

$$D_y = \epsilon E_y(y) + \mu_L \varepsilon_{yy,y}(y) - \mu_T \kappa - l_2^2 \epsilon E_{y,yy}(y), \tag{J.17}$$
$$D_x = 0. \tag{J.18}$$

Therefore, equilibrium equations in y-direction read:

$$-C_T \kappa + C_L \varepsilon_{yy,y}(y) + \mu_L E_{y,yy}(y) - l_1^2 C_L \varepsilon_{yy,yyy}(y) = 0, \tag{J.19}$$
$$\epsilon E_{y,y}(y) + \mu_L \varepsilon_{yy,yy}(y) - l_2^2 \epsilon E_{y,yyy}(y) = 0, \tag{J.20}$$

subjected to homogeneous Neumann boundary conditions (Eqs. (2.23),(2.25)):

$$l_1^2 C_L \varepsilon_{yy,y}(y) - (1-\zeta)\mu_L E_y(y) - l_1^2 C_T \kappa = 0, \quad \text{on} \quad y = \{-\frac{T}{2}, \frac{T}{2}\}, \tag{J.21}$$

$$l_2^2 \epsilon E_{y,y}(y) - \zeta \mu_L \varepsilon_{yy}(y) + \zeta \mu_T \kappa y = 0, \quad \text{on} \quad y = \{-\frac{T}{2}, \frac{T}{2}\}. \tag{J.22}$$

The low-order homogeneous Neumann boundary conditions (Eqs. (2.22),(2.24)) will be satisfied with the solution we will postulate.

Extracting $E_{y,y}$ and $\varepsilon_{yy,y}$ from (J.15) and (J.17), respectively, and replacing them into (J.19) and (J.20), respectively, we obtain:

$$(l_1^2 l_2^2) E_{y,yyyy}(y) - (l_1^2 + l_2^2 + l_\mu^2) E_{y,yy}(y) + E_y(y) = \frac{D_y - l_1^2 D_{y,yy}}{\epsilon} - \frac{\kappa}{\epsilon}(\mu_L \frac{C_T}{C_L} - \mu_T), \tag{J.23}$$

$$(l_1^2 l_2^2) \varepsilon_{yy,yyyy}(y) - (l_1^2 + l_2^2 + l_\mu^2) \varepsilon_{yy,yy}(y) + \varepsilon_{yy}(y) = \frac{\sigma_{yy} - l_2^2 \sigma_{yy,yy}}{C_L} + \frac{C_T}{C_L}\kappa y. \tag{J.24}$$

where $l_\mu^2 = \frac{\mu_L^2}{C_L \epsilon}$.

One can postulate the solutions to be of the form:

$$\begin{aligned} E_y =& k_1 \exp\left(\frac{-y - T/2}{a_1}\right) + k_2 \exp\left(\frac{-y - T/2}{a_2}\right) + k_3 \exp\left(\frac{y - T/2}{a_1}\right) + k_4 \exp\left(\frac{y - T/2}{a_2}\right) \\ & - \frac{\kappa}{\epsilon}\left(\mu_L \frac{C_T}{C_L} - \mu_T\right), \end{aligned} \tag{J.25}$$

$$\begin{aligned} \varepsilon_{yy}(y) =& k_5 \exp\left(\frac{-y - T/2}{a_1}\right) + k_6 \exp\left(\frac{-y - T/2}{a_2}\right) + k_7 \exp\left(\frac{y - T/2}{a_1}\right) + k_8 \exp\left(\frac{y - T/2}{a_2}\right) \\ & + \frac{C_T}{C_L}\kappa y, \end{aligned} \tag{J.26}$$

for $y \in [-T/2, T/2]$, with:

$$a_1, a_2 = \sqrt{\frac{2 l_1^2 l_2^2}{l_1^2 + l_2^2 + l_\mu^2 \pm \sqrt{(l_1^2 + l_2^2 + l_\mu^2)^2 - 4 l_1^2 l_2^2}}}. \tag{J.27}$$

Note that $k_1 = k_3$, $k_2 = k_4$, $k_5 = -k_7$, $k_6 = -k_8$ due to symmetry. Substituting the E_y and ε_{yy} from Eqs. (J.25) and (J.26) to Eqs. (J.19), (J.20), (J.21) and (J.22), we obtain the unknowns k_i.

$$k_1 = k_3 = \frac{-\kappa(C_L \mu_T - C_T \mu_L)(2 a_2 \hat{\gamma}_2 (\zeta - 1) + \hat{\beta}_2 T \zeta)}{2 C_L \epsilon (a_1 \hat{\beta}_2 \hat{\gamma}_1 - a_2 \hat{\beta}_1 \hat{\gamma}_2)}, \tag{J.28}$$

$$k_2 = k_4 = \frac{\kappa(C_L \mu_T - C_T \mu_L)(2 a_1 \hat{\gamma}_1 (\zeta - 1) + \hat{\beta}_1 T \zeta)}{2 C_L \epsilon (a_1 \hat{\beta}_2 \hat{\gamma}_1 - a_2 \hat{\beta}_1 \hat{\gamma}_2)}, \tag{J.29}$$

$$k_5 = -k_7 = \frac{-a_1\alpha_1\kappa(C_L\mu_T - C_T\mu_L)(2a_2\hat{\gamma}_2(\zeta - 1) + \hat{\beta}_2 T\zeta)}{2C_L\mu_L(a_1\hat{\beta}_2\hat{\gamma}_1 - a_2\hat{\beta}_1\hat{\gamma}_2)}, \tag{J.30}$$

$$k_6 = -k_8 = \frac{a_2\alpha_2\kappa(C_L\mu_T - C_T\mu_L)(2a_1\hat{\gamma}_1(\zeta - 1) + \hat{\beta}_1 T\zeta)}{2C_L\mu_L(a_1\hat{\beta}_2\hat{\gamma}_1 - a_2\hat{\beta}_1\hat{\gamma}_2)}. \tag{J.31}$$

where

$$\alpha_i = 1 - \frac{l_2^2}{a_i^2}, \tag{J.32}$$

$$\hat{\beta}_i = (1 + \exp(-T/a_i))\left(\frac{l_1^2}{l_\mu^2}\alpha_i + 1 - \zeta\right), \tag{J.33}$$

$$\hat{\gamma}_i = (1 - \exp(-T/a_i))\left(\frac{l_2^2}{a_i^2}(1 - \zeta) + \zeta\right). \tag{J.34}$$

Bibliography

A. Abdollahi, D. Millán, C. Peco, M. Arroyo, and I. Arias. Revisiting pyramid compression to quantify flexoelectricity: A three-dimensional simulation study. *Phys. Rev. B* **91**, 104103 (2015a).

A. Abdollahi, N. Domingo, I. Arias, and G. Catalan. Converse flexoelectricity yields large piezoresponse force microscopy signals in non-piezoelectric materials. *Nature communications* **10**, 1 (2019).

A. Abdollahi, C. Peco, D. Millan, M. Arroyo, and I. Arias. Computational evaluation of the flexoelectric effect in dielectric solids. *Journal of Applied Physics* **116**, 93502 (2014).

A. Abdollahi, C. Peco, D. Millán, M. Arroyo, G. Catalan, and I. Arias. Fracture toughening and toughness asymmetry induced by flexoelectricity. *Physical Review B* **92**, 94101 (2015b).

F. Ahmadpoor, Q. Deng, L. Liu, and P. Sharma. Apparent flexoelectricity in lipid bilayer membranes due to external charge and dipolar distributions. *Physical Review E* **88**, 050701 (2013).

F. Ahmadpoor and P. Sharma. Flexoelectricity in two-dimensional crystalline and biological membranes. *Nanoscale* **7**, 16555 (2015).

E. C. Aifantis. Strain gradient interpretation of size effects. *Fracture scaling* , 299 (1999).

H. G. Allen. Chapter 8 - Wrinkling and other forms of local instability. in *Analysis and Design of Structural Sandwich Panels*. The Commonwealth and International Library: Structures and Solid Body Mechanics Division. edited by H. G. Allen (Pergamon, 1969) pp. 156–189.

B. S. Altan and E. C. Aifantis. On some aspects in the special theory of gradient elasticity. *Journal of the Mechanical Behavior of Materials* **8**, 231 (1997).

V. Amoli, J. S. Kim, S. Y. Kim, J. Koo, Y. S. Chung, H. Choi, and D. H. Kim. Ionic tactile sensors for emerging human-interactive technologies: a review of recent progress. *Advanced Functional Materials* **30**, 1904532 (2020).

L. Anqing, Z. Shenjie, Q. Lu, and C. Xi. A flexoelectric theory with rotation gradient effects for elastic dielectrics. *Modell. Simul. Mater. Sci. Eng.* **24**, 015009 (2015).

H. Askes, P. Livieri, L. Susmel, D. Taylor, and R. Tovo. Intrinsic material length, Theory of Critical Distances and Gradient Mechanics: analogies and differences in processing linear-elastic crack tip stress fields. *Fatigue & Fracture of Engineering Materials & Structures* **36**, 39 (2013).

H. Askes and E. C. Aifantis. Gradient elasticity in statics and dynamics: An overview of formulations, length scale identification procedures, finite element implementations and new results. *International Journal of Solids and Structures* **48**, 1962 (2011a).

H. Askes and E. C. Aifantis. Gradient elasticity in statics and dynamics: an overview of formulations, length scale identification procedures, finite element implementations and new results. *Int. J. Solids Struct.* **48**, 1962 (2011b).

A. Auguste, L. Jin, Z. Suo, and R. C. Hayward. The role of substrate pre-stretch in post-wrinkling bifurcations. *Soft Matter* **10**, 6520 (2014).

C. Bagni, H. Askes, and L. Susmel. Gradient elasticity: a transformative stress analysis tool to design notched components against uniaxial/multiaxial high-cycle fatigue. *Fatigue & Fracture of Engineering Materials & Structures* **39**, 1012 (2016).

J. Barceló-Mercader, D. Codony, S. Fernández-Méndez, and I. Arias. Weak enforcement of interface continuity and generalized periodicity in high-order electromechanical problems. *International Journal for Numerical Methods in Engineering* **123**, 901 (2022).

J. Barceló-Mercader, D. Codony, A. Mocci, and I. Arias. High-order generalized periodicity conditions for architected materials with application to flexoelectricity. (2023). Under review.

Z. Bazant. Size effect on structural strength: a review. *Archive of applied Mechanics* **69**, 703 (1999).

Z. Bazant. Size effect. *International Journal of Solids and Structures* **37**, 69 (2000).

S. P. Beeby, M. J. Tudor, and N. White. Energy harvesting vibration sources for microsystems applications. *Measurement science and technology* **17**, R175 (2006).

F. Berto and P. Lazzarin. Recent developments in brittle and quasi-brittle failure assessment of engineering materials by means of local approaches. *Materials Science and Engineering: R: Reports* **75**, 1 (2014).

U. K. Bhaskar, N. Banerjee, A. Abdollahi, Z. Wang, D. G. Schlom, G. Rijnders, and G. Catalan. A flexoelectric microelectromechanical system on silicon. *Nature nanotechnology* **11**, 263 (2016).

N. B. Bowden, S. T. Brittain, A. G. Evans, J. W. Hutchinson, and G. M. Whitesides. Spontaneous Formation of Ordered Structures in Thin Films of Metals Supported on an Elastomeric Polymer. *Nature* **393**, 146 (1998).

F. Brau, P. Damman, H. Diamant, and T. A. Witten. Wrinkle to fold transition: influence of the substrate response. *Soft Matter* **9**, 8177 (2013).

F. Brau, H. Vandeparre, A. Sabbah, C. Poulard, A. Boudaoud, and P. Damman. Multiple-length-scale elastic instability mimics parametric resonance of nonlinear oscillators. *Nature Physics* **7**, 56 (2011).

K. D. Breneman, W. E. Brownell, and R. D. Rabbitt. Hair cell bundles: flexoelectric motors of the inner ear. *PLoS One* **4**, e5201 (2009).

S. Budday, E. Kuhl, and J. W. Hutchinson. Period-doubling and period-tripling in growing bilayered systems. *Philosophical Magazine* **95**, 3208 (2015).

J. M. Bursian and O. I. Zaikovskii. Changes in curvature of a ferroelectric film due to polarization. *Soviet Physics Solid State* **10**, 1121 (1968).

S. Cai, D. Chen, Z. Suo, and R. C. Hayward. Creasing instability of elastomer films. *Soft Matter* **8**, 1301 (2012).

C. Cao, H. F. Chan, J. Zang, K. W. Leong, and X. Zhao. Harnessing localized ridges for high-aspect-ratio hierarchical patterns with dynamic tunability and multifunctionality. *Advanced materials* **26**, 1763 (2014).

Y. Cao and J. W. Hutchinson. From wrinkles to creases in elastomers: the instability and imperfection-sensitivity of wrinkling. *Proceedings of the Royal Society A: Mathematical, Physical and Engineering Sciences* **468**, 94 (2012a).

Y. Cao and J. W. Hutchinson. Wrinkling phenomena in neo-Hookean film/substrate bilayers. *Journal of applied mechanics* **79**, 31019 (2012b).

G. Catalan, L. Sinnamon, and J. Gregg. The effect of flexoelectricity on the dielectric properties of inhomogeneously strained ferroelectric thin films. *J. Condens. Matter Phys.* **16**, 2253 (2004).

T. Chen, Y. Xue, A. K. Roy, and L. Dai. Transparent and stretchable high-performance supercapacitors based on wrinkled graphene electrodes. *Acs Nano* **8**, 1039 (2013).

T. Chen, Y. Xue, A. K. Roy, and L. Dai. Transparent and stretchable high-performance supercapacitors based on wrinkled graphene electrodes. *ACS nano* **8**, 1039 (2014).

S. H. Cho, S. W. Lee, S. Yu, H. Kim, S. Chang, D. Kang, I. Hwang, H. S. Kang, B. Jeong, E. H. Kim, and Others. Micropatterned pyramidal ionic gels for sensing broad-range pressures with high sensitivity. *ACS applied materials & interfaces* **9**, 10128 (2017).

S.-B. Choi and G.-W. Kim. Measurement of flexoelectric response in polyvinylidene fluoride films for piezoelectric vibration energy harvesters. *Journal of Physics D: Applied Physics* **50**, 75502 (2017).

A. Chortos, J. Liu, and Z. Bao. Pursuing prosthetic electronic skin. *Nature materials* **15**, 937 (2016).

D. Codony, A. Mocci, J. Barceló-Mercader, and I. Arias. Mathematical and computational modeling of flexoelectricity. *Journal of Applied Physics* **130**, 231102 (2021).

D. Codony. Mathematical and computational modeling of flexoelectricity at mesoscopic and atomistic scales. (2021).

D. Codony, P. Gupta, O. Marco, and I. Arias. Modeling flexoelectricity in soft dielectrics at finite deformation. *Journal of the Mechanics and Physics of Solids* , 104182 (2020).

D. Codony, O. Marco, S. Fernández-Méndez, and I. Arias. An Immersed Boundary Hierarchical B-spline method for flexoelectricity. *Computer Methods in Applied Mechanics and Engineering* (2019).

K. Cordero-Edwards, H. Kianirad, C. Canalias, J. Sort, and G. Catalan. Flexoelectric fracture-ratchet effect in ferroelectrics. *Physical review letters* **122**, 135502 (2019).

L. E. Cross. Flexoelectric effects: Charge separation in insulating solids subjected to elastic strain gradients. *Journal of Materials Science* **41**, 53 (2006).

C. Dagdeviren, P. Joe, O. L. Tuzman, K.-I. Park, K. J. Lee, Y. Shi, Y. Huang, and J. A. Rogers. Recent progress in flexible and stretchable piezoelectric devices for mechanical energy harvesting, sensing and actuation. *Extreme mechanics letters* **9**, 269 (2016).

S. Dai, M. Gharbi, P. Sharma, and H. S. Park. Surface piezoelectricity: size effects in nanostructures and the emergence of piezoelectricity in non-piezoelectric materials. *Journal of Applied Physics* **110**, 104305 (2011).

A. Danescu. Hyper-pre-stress vs. strain-gradient for surface relaxation in diamond-like structures. *Journal of the Mechanics and Physics of Solids* **60**, 623 (2012).

F. Deng, Q. Deng, W. Yu, and S. Shen. Mixed finite elements for flexoelectric solids. *Journal of Applied Mechanics* **84**, 81004 (2017).

Q. Deng, F. Ahmadpoor, W. E. Brownell, and P. Sharma. The collusion of flexoelectricity and Hopf bifurcation in the hearing mechanism. *Journal of the Mechanics and Physics of Solids* **130**, 245 (2019).

Q. Deng, M. Kammoun, A. Erturk, and P. Sharma. Nanoscale flexoelectric energy harvesting. *International Journal of Solids and Structures* **51**, 3218 (2014a).

Q. Deng, L. Liu, and P. Sharma. Flexoelectricity in soft materials and biological membranes. *Journal of the Mechanics and Physics of Solids* **62**, 209 (2014b).

M. D. Dickey. Stretchable and soft electronics using liquid metals. *Advanced Materials* **29**, 1606425 (2017).

B. Dortdivanlioglu, A. Krischok, L. da Veiga, and C. Linder. Mixed isogeometric analysis of strongly coupled diffusion in porous materials. *International Journal for Numerical Methods in Engineering* **114**, 28 (2018).

B. Dortdivanlioglu and C. Linder. Diffusion-driven swelling-induced instabilities of hydrogels. *Journal of the Mechanics and Physics of Solids* **125**, 38 (2019).

E. A. Eliseev, M. D. Glinchuk, V. Khist, V. V. Skorokhod, R. Blinc, and A. N. Morozovska. Linear magnetoelectric coupling and ferroelectricity induced by the flexomagnetic effect in ferroics. *Phys. Rev. B* **84**, 174112 (2011).

E. Eliseev, A. Morozovska, M. Glinchuk, and R. Blinc. Spontaneous flexoelectric/flexomagnetic effect in nanoferroics. *Phys. Rev. B* **79**, 165433 (2009).

L. Evans. *Partial Differential Equations*. Graduate studies in mathematics (American Mathematical Society, 2010).

S. Filippi, P. Lazzarin, and R. Tovo. Developments of some explicit formulas useful to describe elastic stress fields ahead of notches in plates. *International Journal of Solids and Structures* **39**, 4543 (2002).

H. Gao, B. Ji, I. L. Jäger, E. Arzt, and P. Fratzl. Materials become insensitive to flaws at nanoscale: lessons from nature. *Proceedings of the national Academy of Sciences* **100**, 5597 (2003).

I. M. Gitman. Representative volumes and multi-scale modelling of quasi-brittle materials. (2006).

S. Gong and W. Cheng. One-dimensional nanomaterials for soft electronics. *Advanced Electronic Materials* **3**, 1600314 (2017).

M. Grasinger, K. Mozaffari, and P. Sharma. Flexoelectricity in soft elastomers and the molecular mechanisms underpinning the design and emergence of giant flexoelectricity. *Proceedings of the National Academy of Sciences* **118** (2021).

X. W. Gu, Z. Wu, Y.-W. Zhang, D. J. Srolovitz, and J. R. Greer. Microstructure versus flaw: mechanisms of failure and strength in nanostructures. *Nano letters* **13**, 5703 (2013).

A. R. Hadjesfandiari. Size-dependent piezoelectricity. *Int. J. Solids Struct.* **50**, 2781 (2013).

G. H. Haertling. Ferroelectric ceramics: history and technology. *Journal of the American Ceramic Society* **82**, 797 (1999).

M. L. Hammock, A. Chortos, B. C.-K. Tee, J. B.-H. Tok, and Z. Bao. 25th anniversary article: the evolution of electronic skin (e-skin): a brief history, design considerations, and recent progress. *Advanced materials* **25**, 5997 (2013).

B. He, B. Javvaji, and X. Zhuang. Characterizing flexoelectricity in composite material using the element-free Galerkin method. *Energies* **12**, 271 (2019).

R. W. Hertzberg and F. E. Hauser. Deformation and fracture mechanics of engineering materials. (1977).

S. Hu and S. Shen. Variational principles and governing equations in nano-dielectrics with the flexoelectric effect. *Science China Physics, Mechanics and Astronomy* **53**, 1497 (2010).

W. Huang, S.-R. Kwon, S. Zhang, F.-G. Yuan, and X. Jiang. A trapezoidal flexoelectric accelerometer. *Journal of Intelligent Material Systems and Structures* **25**, 271 (2014).

W. Huang, X. Yan, S. R. Kwon, S. Zhang, F.-G. Yuan, and X. Jiang. Flexoelectric strain gradient detection using Ba0. 64Sr0. 36TiO3 for sensing. *Applied Physics Letters* **101**, 252903 (2012).

T. Ikeda. *Fundamentals of piezoelectricity* (Oxford university press, 1996).

B. Jaffe, R. Roth, and S. Marzullo. Properties of piezoelectric ceramics in the solid-solution series lead titanate-lead zirconate-lead oxide: tin oxide and lead titanate-lead hafnate. *Journal of research of the National Bureau of Standards* **55**, 239 (1955).

H. Jaffe. Piezoelectric ceramics. *Journal of the American Ceramic Society* **41**, 494 (1958).

B. Ji, Y. Mao, Q. Zhou, J. Zhou, G. Chen, Y. Gao, Y. Tian, W. Wen, and B. Zhou. Facile preparation of hybrid structure based on mesodome and micropillar arrays as flexible electronic skin with tunable sensitivity and detection range. *ACS applied materials & interfaces* **11**, 28060 (2019).

X. Jiang, W. Huang, and S. Zhang. Flexoelectric nano-generator: Materials, structures and devices. *Nano Energy* **2**, 1079 (2013).

L. Jin, A. Takei, and J. W. Hutchinson. Mechanics of wrinkle/ridge transitions in thin film/substrate systems. *Journal of the Mechanics and Physics of Solids* **81**, 22 (2015).

Y. Joo, J. Byun, N. Seong, J. Ha, H. Kim, S. Kim, T. Kim, H. Im, D. Kim, and Y. Hong. Silver nanowire-embedded PDMS with a multiscale structure for a highly sensitive and robust flexible pressure sensor. *Nanoscale* **7**, 6208 (2015).

C. Kadapa, W. G. Dettmer, and D. Perić. Subdivision based mixed methods for isogeometric analysis of linear and nonlinear nearly incompressible materials. *Computer Methods in Applied Mechanics and Engineering* **305**, 241 (2016).

C. Keplinger, J.-Y. Sun, C. C. Foo, P. Rothemund, G. M. Whitesides, and Z. Suo. Stretchable, transparent, ionic conductors. *Science* **341**, 984 (2013).

S. M. Kogan. Piezoelectric effect during inhomogeneous deformation and acoustic scattering of carriers in crystals. *Sov. Phys. Solid State* **5**, 2069 (1964).

M. Kollosche, J. Zhu, Z. Suo, and G. Kofod. Complex interplay of nonlinear processes in dielectric elastomers. *Physical Review E* **85**, 51801 (2012).

R. Kornbluh, R. Pelrine, J. Eckerle, and J. Joseph. Electrostrictive polymer artificial muscle actuators. in *Proceedings. 1998 IEEE international conference on robotics and automation (Cat. No. 98CH36146)*. Vol. 3 (IEEE, 1998) pp. 2147–2154.

S. Kumar, M. A. Haque, and H. Gao. Notch insensitive fracture in nanoscale thin films. *Applied Physics Letters* **94**, 253104 (2009).

S. Kumar, X. Li, A. Haque, and H. Gao. Is stress concentration relevant for nanocrystalline metals? *Nano letters* **11**, 2510 (2011).

S. R. Kwon, W. B. Huang, S. J. Zhang, F. G. Yuan, and X. N. Jiang. Study on a flexoelectric microphone using barium strontium titanate. *Journal of Micromechanics and Microengineering* **26**, 45001 (2016).

M. Lallart, P.-J. Cottinet, D. Guyomar, and L. Lebrun. Electrostrictive polymers for mechanical energy harvesting. *Journal of Polymer Science Part B: Polymer Physics* **50**, 523 (2012).

D. C. Lam, F. Yang, A. Chong, J. Wang, and P. Tong. Experiments and theory in strain gradient elasticity. *Journal of the Mechanics and Physics of Solids* **51**, 1477 (2003).

L. D. Landau and E. M. Lifshitz. *Course of theoretical physics* (Elsevier, 2013).

P. Lazzarin and R. Zambardi. A finite-volume-energy based approach to predict the static and fatigue behavior of components with sharp V-shaped notches. *International Journal of Fracture* **112**, 275 (2001).

P. Lazzarin, F. Berto, and M. Zappalorto. Rapid calculations of notch stress intensity factors based on averaged strain energy density from coarse meshes: Theoretical bases and applications. *International Journal of Fatigue* **32**, 1559 (2010).

J. H. Lee, K.-E. Kim, B.-K. Jang, A. A. Ünal, S. Valencia, F. Kronast, K.-T. Ko, S. Kowarik, J. Seidel, and C.-H. Yang. Strain-gradient-induced magnetic anisotropy in straight-stripe mixed-phase bismuth ferrites: Insight into flexomagnetism. *Physical Review B* **96**, 64402 (2017).

X. Lei, C. Li, X. Shi, X. Xu, and Y. Wei. Notch strengthening or weakening governed by transition of shear failure to normal mode fracture. (2015).

A. Li, S. Zhou, L. Qi, and X. Chen. A reformulated flexoelectric theory for isotropic dielectrics. *J. Phys. D: Appl. Phys.* **48**, 465502 (2015).

T. Li, H. Luo, L. Qin, X. Wang, Z. Xiong, H. Ding, Y. Gu, Z. Liu, and T. Zhang. Flexible capacitive tactile sensor based on micropatterned dielectric layer. *Small* **12**, 5042 (2016).

Y. Li, J. J. Peterson, S. B. Jhaveri, and K. R. Carter. Patterned polymer films via reactive silane infusion-induced wrinkling. *Langmuir* **29**, 4632 (2013).

E. Lifshitz and L. Landau. Statistical Physics (Course of Theoretical Physics, Volume 5). (1984).

C. Liu, J. Wang, G. Xu, M. Kamlah, and T.-Y. Zhang. An isogeometric approach to flexoelectric effect in ferroelectric materials. *International Journal of Solids and Structures* **162**, 198 (2019).

L. Liu. An energy formulation of continuum magneto-electro-elasticity with applications. *Journal of the Mechanics and Physics of Solids* **63**, 451 (2014a).

L. Liu. An energy formulation of continuum magneto-electro-elasticity with applications. *J. Mech. Phys. Solids* **63**, 451 (2014b).

L. Liu and P. Sharma. Flexoelectricity and thermal fluctuations of lipid bilayer membranes: Renormalization of flexoelectric, dielectric, and elastic properties. *Physical Review E* **87**, 032715 (2013).

Y. Liu, J. Chen, H. Deng, G. Hu, D. Zhu, and N. Dai. Anomalous thermoelectricity in strained Bi 2 Te 3 films. *Scientific reports* **6**, 32661 (2016).

H. Lu, C.-W. Bark, D. E. De Los Ojos, J. Alcala, C.-B. Eom, G. Catalan, and A. Gruverman. Mechanical writing of ferroelectric polarization. *Science* **336**, 59 (2012).

W. Ma and L. E. Cross. Observation of the flexoelectric effect in relaxor Pb ($Mg_{1/3}$ $Nb_{2/3}$) O_3 ceramics. *Appl. Phys. Lett.* **78**, 2920 (2001).

W. Ma and L. E. Cross. Flexoelectric polarization of barium strontium titanate in the paraelectric state. *Applied Physics Letters* **81**, 3440 (2002).

S. C. B. Mannsfeld, B. C. K. Tee, R. M. Stoltenberg, C. V. Chen, S. Barman, B. V. O. Muir, A. N. Sokolov, C. Reese, and Z. Bao. Highly sensitive flexible pressure sensors with microstructured rubber dielectric layers. *Nature materials* **9**, 859 (2010).

S. Mao, P. K. Purohit, and N. Aravas. Mixed finite-element formulations in piezoelectricity and flexoelectricity. *Proceedings of the Royal Society A: Mathematical, Physical and Engineering Sciences* **472**, 20150879 (2016).

R. Maranganti, N. Sharma, and P. Sharma. Electromechanical coupling in nonpiezoelectric materials due to nanoscale nonlocal size effects: Green's function solutions and embedded inclusions. *Phys. Rev. B* **74**, 014110 (2006).

V. Mashkevich and K. Tolpygo. Electrical, optical and elastic properties of diamond type crystals. *Sov. Phys. JETP* **5**, 435 (1957).

A. T. McBride, D. Davydov, and P. Steinmann. Modelling the flexoelectric effect in solids: a micromorphic approach. *Computer Methods in Applied Mechanics and Engineering* **371**, 113320 (2020).

V. I. Merupo, B. Guiffard, R. Seveno, M. Tabellout, and A. Kassiba. Flexoelectric response in soft polyurethane films and their use for large curvature sensing. *Journal of Applied Physics* **122**, 144101 (2017).

R. B. Meyer. Piezoelectric effects in liquid crystals. *Physical Review Letters* **22**, 918 (1969).

R. D. Mindlin. Influence of couple-stresses on stress concentrations. *Experimental mechanics* **3**, 1 (1963).

R. D. Mindlin and N. N. Eshel. On first strain-gradient theories in linear elasticity. *International Journal of Solids and Structures* **4**, 109 (1968a).

R. D. Mindlin and N. N. Eshel. On first strain-gradient theories in linear elasticity. *Int. J. Solids Struct.* **4**, 109 (1968b).

R. D. Mindlin and H. F. Tiersten. Effects of couple-stresses in linear elasticity. *Arch. Ration. Mech. Anal.* **11**, 415 (1962).

R. D. Mindlin. Micro-structure in linear elasticity. *Archive for Rational Mechanics and Analysis* **16**, 51 (1964).

R. D. Mindlin. Polarization gradient in elastic dielectrics. *International Journal of Solids and Structures* **4**, 637 (1968).

C. A. Mizzi, A. Y. W. Lin, and L. D. Marks. Does flexoelectricity drive triboelectricity? *Physical review letters* **123**, 116103 (2019).

C. A. Mizzi and L. D. Marks. When Flexoelectricity Drives Triboelectricity. *Nano letters* **22**, 3939 (2022).

A. Mocci, J. Barceló-Mercader, D. Codony, and I. Arias. Geometrically polarized architected dielectrics with apparent piezoelectricity. *Journal of the Mechanics and Physics of Solids* **157**, 104643 (2021).

P. Mohammadi, L. Liu, and P. Sharma. A theory of flexoelectric membranes and effective properties of heterogeneous membranes. *Journal of Applied Mechanics* **81** (2014).

L. C. Montemayor, W. H. Wong, Y.-W. Zhang, and J. R. Greer. Insensitivity to flaws leads to damage tolerance in brittle architected meta-materials. *Scientific reports* **6**, 20570 (2016).

A. N. Morozovska, V. V. Khist, M. D. Glinchuk, C. M. Scherbakov, M. V. Silibin, D. V. Karpinsky, and E. A. Eliseev. Flexoelectricity induced spatially modulated phases in ferroics and liquid crystals. *Journal of Molecular liquids* **267**, 550 (2018).

E. Ng, Y. Yang, V. Hong, C. Ahn, D. Heinz, I. Flader, Y. Chen, C. Everhart, B. Kim, R. Melamud, *et al.*. The long path from MEMS resonators to timing products. in *2015 28th IEEE International Conference on Micro Electro Mechanical Systems (MEMS)* (IEEE, 2015) pp. 1–2.

B. H. Nguyen, X. Zhuang, and T. Rabczuk. NURBS-based formulation for nonlinear electro-gradient elasticity in semiconductors. *Computer Methods in Applied Mechanics and Engineering* **346**, 1074 (2019).

T. D. Nguyen, S. Mao, Y.-W. Yeh, P. K. Purohit, and M. C. McAlpine. Nanoscale flexoelectricity. *Adv. Mater.* **25**, 946 (2013a).

T. D. Nguyen, S. Mao, Y.-W. Yeh, P. K. Purohit, and M. C. McAlpine. Nanoscale Flexoelectricity. *Advanced Materials* **25**, 946 (2013b).

B. Nie, R. Li, J. Cao, J. D. Brandt, and T. Pan. Flexible transparent iontronic film for interfacial capacitive pressure sensing. *Advanced Materials* **27**, 6055 (2015).

R. Núñez-Toldrà, F. Vasquez-Sancho, N. Barroca, and G. Catalan. investigation of the cellular Response to Bone fractures: evidence for flexoelectricity. *Scientific reports* **10**, 1 (2020).

X. Pan, S. Yu, and X. Feng. A continuum theory of surface piezoelectricity for nanodielectrics. *Science China Physics, Mechanics and Astronomy* **54**, 564 (2011).

J. Park, M. Kim, Y. Lee, H. S. Lee, and H. Ko. Fingertip skin–inspired microstructured ferroelectric skins discriminate static/dynamic pressure and temperature stimuli. *Science advances* **1**, e1500661 (2015).

S.-J. Park, J. Kim, M. Chu, and M. Khine. Highly flexible wrinkled carbon nanotube thin film strain sensor to monitor human movement. *Advanced Materials Technologies* **1**, 1600053 (2016).

R. H. Peerlings, R. de Borst, W. M. Brekelmans, and J. de Vree. Gradient enhanced damage for quasi-brittle materials. *International Journal for numerical methods in engineering* **39**, 3391 (1996).

R. Pelrine, R. Kornbluh, J. Joseph, and S. Chiba. Electrostriction of polymer films for microactuators. in *Proceedings IEEE the tenth annual international workshop on micro electro mechanical systems. An investigation of micro structures, sensors, actuators, machines and robots* (IEEE, 1997) pp. 238–243.

R. E. Pelrine, R. D. Kornbluh, and J. P. Joseph. Electrostriction of polymer dielectrics with compliant electrodes as a means of actuation. *Sensors and Actuators A: Physical* **64**, 77 (1998).

Q. Peng, J. Chen, T. Wang, X. Peng, J. Liu, X. Wang, J. Wang, and H. Zeng. Recent advances in designing conductive hydrogels for flexible electronics. *InfoMat* **2**, 843 (2020).

A. G. Petrov. Liquid crystal physics and the physics of living matter. *Molecular Crystals and Liquid Crystals Science and Technology. Section A. Molecular Crystals and Liquid Crystals* **332**, 577 (1999).

L. Placidi and E. Barchiesi. Energy approach to brittle fracture in strain-gradient modelling. *Proceedings of the Royal Society A: Mathematical, Physical and Engineering Sciences* **474**, 20170878 (2018).

R. Poya, A. J. Gil, R. Ortigosa, and R. Palma. On a family of numerical models for couple stress based flexoelectricity for continua and beams. *Journal of the Mechanics and Physics of Solids* **125**, 613 (2019).

S. Priya, R. Taneja, R. Myers, and R. Islam. Piezoelectric energy harvesting using bulk transducers. *Piezoelectric and Acoustic Materials for Transducer Applications* , 373 (2008).

Z. Qiu, Y. Wan, W. Zhou, J. Yang, J. Yang, J. Huang, J. Zhang, Q. Liu, S. Huang, N. Bai, and Others. Ionic skin with biomimetic dielectric layer templated from calathea zebrine leaf. *Advanced Functional Materials* **28**, 1802343 (2018).

R. Qu, P. Zhang, and Z. Zhang. Notch effect of materials: strengthening or weakening? *Journal of Materials Science and Technology* **30**, 599 (2014).

A. H. Rahmati, S. Bauer, and P. Sharma. Nonlinear bending deformation of soft electrets and prospects for engineering flexoelectricity and transverse (d 31) piezoelectricity. *Soft matter* **15**, 127 (2019).

A. D. Rey. Liquid crystal model of membrane flexoelectricity. *Physical Review E* **74**, 011710 (2006).

T. Rüberg and F. Cirak. Subdivision-stabilised immersed b-spline finite elements for moving boundary flows. *Computer Methods in Applied Mechanics and Engineering* **209**, 266 (2012).

T. Rüberg, F. Cirak, and J. M. G. Aznar. An unstructured immersed finite element method for nonlinear solid mechanics. *Advanced Modeling and Simulation in Engineering Sciences* **3**, 22 (2016).

S. R. A. Ruth, V. R. Feig, H. Tran, and Z. Bao. Microengineering pressure sensor active layers for improved performance. *Advanced Functional Materials* **30**, 2003491 (2020).

E. Sahin and S. Dost. A strain-gradients theory of elastic dielectrics with spatial dispersion. *Int. J. Eng. Sci.* **26**, 1231 (1988).

Y. Saito, H. Takao, T. Tani, T. Nonoyama, K. Takatori, T. Homma, T. Nagaya, and M. Nakamura. Lead-free piezoceramics. *Nature* **432**, 84 (2004).

Z. D. Sha, Q. X. Pei, Z. S. Liu, Y. W. Zhang, and T. J. Wang. Necking and notch strengthening in metallic glass with symmetric sharp-and-deep notches. *Scientific Reports* **5**, 10797 (2015).

Z. Sha, Y. Teng, L. H. Poh, Q. Pei, G. Xing, and H. Gao. Notch strengthening in nanoscale metallic glasses. *Acta Materialia* **169**, 147 (2019).

H. Shang, X. Liang, F. Deng, S. Hu, and S. Shen. Flexoelectricity in wrinkled thin films. *International Journal of Mechanical Sciences* , 107685 (2022).

N. D. Sharma, C. M. Landis, and P. Sharma. Piezoelectric thin-film superlattices without using piezoelectric materials. *Journal of Applied Physics* **108**, 1 (2010).

N. D. Sharma, R. Maranganti, and P. Sharma. On the possibility of piezoelectric nanocomposites without using piezoelectric materials. *Journal of the Mechanics and Physics of Solids* **55**, 2328 (2007).

P. Sharma, S. Ryu, J. Burton, T. Paudel, C. Bark, Z. Huang, E. Tsymbal, G. Catalan, C. Eom, and A. Gruverman. Mechanical tuning of LaAlO3/SrTiO3 interface conductivity. *Nano letters* **15**, 3547 (2015).

S. Shen and S. Hu. A theory of flexoelectricity with surface effect for elastic dielectrics. *Journal of the Mechanics and Physics of Solids* **58**, 665 (2010).

T. Shimada, K. Ouchi, Y. Chihara, and T. Kitamura. Breakdown of continuum fracture mechanics at the nanoscale. *Scientific reports* **5**, 8596 (2015).

J. Y. Shu, W. E. King, and N. A. Fleck. Finite elements for materials with strain gradient effects. *International Journal for Numerical Methods in Engineering* **44**, 373 (1999).

L. Shu, S. Ke, L. Fei, W. Huang, Z. Wang, J. Gong, X. Jiang, L. Wang, F. Li, S. Lei, and Others. Photoflexoelectric effect in halide perovskites. *Nature materials* , 1 (2020).

L. Shui, Y. Liu, B. Li, C. Zou, C. Tang, L. Zhu, and X. Chen. Mechanisms of electromechanical wrinkling for highly stretched substrate-free dielectric elastic membrane. *Journal of the Mechanics and Physics of Solids* **122**, 520 (2019).

C. M. Stafford, C. Harrison, K. L. Beers, A. Karim, E. J. Amis, M. R. VanLandingham, H.-C. Kim, W. Volksen, R. D. Miller, and E. E. Simonyi. A buckling-based metrology for measuring the elastic moduli of polymeric thin films. *Nature materials* **3**, 545 (2004).

T. Stevenson, D. Martin, P. Cowin, A. Blumfield, A. Bell, T. Comyn, and P. Weaver. Piezoelectric materials for high temperature transducers and actuators. *Journal of Materials Science: Materials in Electronics* **26**, 9256 (2015).

S. Su, H. Huang, Y. Liu, and Z. H. Zhu. Wrinkling of flexoelectric nano-film/substrate systems. *Journal of Physics D: Applied Physics* **51**, 75309 (2018a).

S. Su, H. Huang, and Z. H. Zhu. Flexoelectric energy harvesters utilizing controllably wrinkled micro-dielectric film. *Energy* **224**, 120056 (2021).

Y. Su, H. C. Broderick, W. Chen, and M. Destrade. Wrinkles in soft dielectric plates. *Journal of the Mechanics and Physics of Solids* **119**, 298 (2018b).

Y. Su, B. Wu, W. Chen, and M. Destrade. Pattern evolution in bending dielectric-elastomeric bilayers. *Journal of the Mechanics and Physics of Solids* , 103670 (2019).

J.-Y. Sun, C. Keplinger, G. M. Whitesides, and Z. Suo. Ionic skin. *Advanced Materials* **26**, 7608 (2014).

J.-Y. Sun, S. Xia, M.-W. Moon, K. H. Oh, and K.-S. Kim. Folding wrinkles of a thin stiff layer on a soft substrate. *Proceedings of the Royal Society A: Mathematical, Physical and Engineering Sciences* **468**, 932 (2011).

L. Susmel, H. Askes, T. Bennett, and D. Taylor. Theory of critical distances versus gradient mechanics in modelling the transition from the short to long crack regime at the fatigue limit. *Fatigue & Fracture of Engineering Materials & Structures* **36**, 861 (2013).

A. K. Tagantsev. Piezoelectricity and flexoelectricity in crystalline dielectrics. *Phys. Rev. B* **34**, 5883 (1986).

A. K. Tagantsev. Electric polarization in crystals and its response to thermal and elastic perturbations. *Phase Transit. A* **35**, 119 (1991).

A. K. Tagantsev and A. S. Yurkov. Flexoelectric effect in finite samples. *Journal of Applied Physics* **112**, 44103 (2012).

S. Terry, J. Eckerle, R. Kornbluh, T. Low, and C. Ablow. Silicon pressure transducer arrays for blood-pressure measurement. *Sensors and Actuators A: Physical* **23**, 1070 (1990).

O. A. Tertuliano, B. W. Edwards, L. R. Meza, V. S. Deshpande, and J. R. Greer. Nanofibril-mediated Fracture Resistance of Bone. (2020). arXiv:2008.09955 [cond-mat.mtrl-sci] .

T. Q. Thai, T. Rabczuk, and X. Zhuang. A large deformation isogeometric approach for flexoelectricity and soft materials. *Computer Methods in Applied Mechanics and Engineering* **341**, 718 (2018).

K. Tolpygo. Long wavelength oscillations of diamond-type crystals including long range forces. *Sov. Phys. Solid State* **4**, 1297 (1963).

F. Vasquez-Sancho, A. Abdollahi, D. Damjanovic, and G. Catalan. Flexoelectricity in bones. *Advanced materials* **30**, 1705316 (2018).

J. Ventura, D. Codony, and S. Fernández-Méndez. A C0 interior penalty finite element method for flexoelectricity. *Journal of Scientific Computing* **88**, 1 (2021).

B. Wang, Y. Gu, S. Zhang, and L.-Q. Chen. Flexoelectricity in solids: Progress, challenges, and perspectives. *Progress in Materials Science* **106**, 100570 (2019a).

C. Wang, L. Dong, D. Peng, and C. Pan. Tactile sensors for advanced intelligent systems. *Advanced Intelligent Systems* **1**, 1900090 (2019b).

C. Wang, C. Wang, Z. Huang, and S. Xu. Materials and structures toward soft electronics. *Advanced Materials* **30**, 1801368 (2018).

H. Wang, X. Jiang, Y. Wang, R. W. Stark, P. A. van Aken, J. Mannhart, and H. Boschker. Direct observation of huge flexoelectric polarization around crack tips. *Nano Letters* **20**, 88 (2019c).

J.-W. Wang, B. Li, Y.-P. Cao, and X.-Q. Feng. Surface wrinkling patterns of film–substrate systems with a structured interface. *Journal of Applied Mechanics* **82** (2015).

Q. Wang and X. Zhao. Creasing-wrinkling transition in elastomer films under electric fields. *Physical Review E* **88**, 42403 (2013).

Q. Wang and X. Zhao. Phase diagrams of instabilities in compressed film-substrate systems. *Journal of applied mechanics* **81**, 51004 (2014).

Q. Wang and X. Zhao. A three-dimensional phase diagram of growth-induced surface instabilities. *Scientific reports* **5**, 8887 (2015).

Y. Wang, R. Yang, Z. Shi, L. Zhang, D. Shi, E. Wang, and G. Zhang. Super-elastic graphene ripples for flexible strain sensors. *ACS nano* **5**, 3645 (2011).

X. Wen, D. Li, K. Tan, Q. Deng, and S. Shen. Flexoelectret: An Electret with a Tunable Flexoelectriclike Response. *Physical review letters* **122**, 148001 (2019).

X. Wen, K. Tan, Q. Deng, and S. Shen. Inverse flexoelectret effect: bending dielectrics by a uniform electric field. *Physical Review Applied* **15**, 14032 (2021).

J. Wu. Perovskite lead-free piezoelectric ceramics. *Journal of Applied Physics* **127**, 190901 (2020).

J. Yang, S. Luo, X. Zhou, J. Li, J. Fu, W. Yang, and D. Wei. Flexible, tunable, and ultrasensitive capacitive pressure sensor with microconformal graphene electrodes. *ACS applied materials & interfaces* **11**, 14997 (2019a).

J. C. Yang, J.-O. Kim, J. Oh, S. Y. Kwon, J. Y. Sim, D. W. Kim, H. B. Choi, and S. Park. Microstructured porous pyramid-based ultrahigh sensitive pressure sensor insensitive to strain and temperature. *ACS applied materials & interfaces* **11**, 19472 (2019b).

J. C. Yang, J. Mun, S. Y. Kwon, S. Park, Z. Bao, and S. Park. Electronic skin: recent progress and future prospects for skin-attachable devices for health monitoring, robotics, and prosthetics. *Advanced Materials* **31**, 1904765 (2019c).

M.-M. Yang, D. J. Kim, and M. Alexe. Flexo-photovoltaic effect. *Science* **360**, 904 (2018).

X.-Y. Yin, Y. Zhang, X. Cai, Q. Guo, J. Yang, and Z. L. Wang. 3D printing of ionic conductors for high-sensitivity wearable sensors. *Materials Horizons* **6**, 767 (2019).

P. V. Yudin and A. K. Tagantsev. Fundamentals of flexoelectricity in solids. *Nanotechnology* **24**, 432001 (2013).

A. S. Yurkov and A. K. Tagantsev. Strong surface effect on direct bulk flexoelectric response in solids. *Appl. Phys. Lett.* **108**, 22904 (2016).

J. Yvonnet and L. P. Liu. A numerical framework for modeling flexoelectricity and Maxwell stress in soft dielectrics at finite strains. *Computer Methods in Applied Mechanics and Engineering* **313**, 450 (2017).

J. Zang, S. Ryu, N. Pugno, Q. Wang, Q. Tu, M. J. Buehler, and X. Zhao. Multifunctionality and control of the crumpling and unfolding of large-area graphene. *Nature materials* **12**, 321 (2013).

J. Zang, X. Zhao, Y. Cao, and J. W. Hutchinson. Localized ridge wrinkling of stiff films on compliant substrates. *Journal of the Mechanics and Physics of Solids* **60**, 1265 (2012).

J.-W. Zha, M.-S. Zheng, B.-H. Fan, and Z.-M. Dang. Polymer-based dielectrics with high permittivity for electric energy storage: A review. *Nano Energy* **89**, 106438 (2021).

B. Zhang and J. Luo. A phase field model for fracture based on the strain gradient elasticity theory with hybrid formulation. *Engineering Fracture Mechanics* **256**, 107975 (2021).

S. Zhang, K. Liu, T. Wu, M. Xu, and S. Shen. Tunable Flexoelectricity of Elastomers. *The Journal of Physical Chemistry C* (2020a).

S. Zhang, K. Liu, M. Xu, and S. Shen. A curved resonant flexoelectric actuator. *Applied Physics Letters* **111**, 82904 (2017).

S. Zhang, Y. Wang, X. Yao, P. Le Floch, X. Yang, J. Liu, and Z. Suo. Stretchable electrets: nanoparticle–elastomer composites. *Nano letters* **20**, 4580 (2020b).

T. Zhang, X. Li, S. Kadkhodaei, and H. Gao. Flaw insensitive fracture in nanocrystalline graphene. *Nano letters* **12**, 4605 (2012).

X. Zhang, A. Vyatskikh, H. Gao, J. R. Greer, and X. Li. Lightweight, flaw-tolerant, and ultrastrong nanoarchitected carbon. *Proceedings of the National Academy of Sciences* **116**, 6665 (2019).

X. Zhao and Z. Suo. Method to analyze electromechanical stability of dielectric elastomers. *Applied Physics Letters* **91**, 61921 (2007).

J. Zhu, M. Kollosche, T. Lu, G. Kofod, and Z. Suo. Two types of transitions to wrinkles in dielectric elastomers. *Soft Matter* **8**, 8840 (2012).

R. Zhu, Z. Wang, H. Ma, G. Yuan, F. Wang, Z. Cheng, and H. Kimura. Poling-free energy harvesters based on robust self-poled ferroelectric fibers. *Nano energy* **50**, 97 (2018).

X. Zhuang, S. S. Nanthakumar, and T. Rabczuk. A meshfree formulation for large deformation analysis of flexoelectric structures accounting for the surface effects. *Engineering Analysis with Boundary Elements* **120**, 153 (2020a).

X. Zhuang, B. H. Nguyen, S. S. Nanthakumar, T. Q. Tran, N. Alajlan, and T. Rabczuk. Computational Modeling of Flexoelectricity—A Review. *Energies* **13**, 1326 (2020b).

Q. Zou, Z. Lei, T. Xue, S. Li, Z. Ma, and Q. Su. Highly sensitive flexible pressure sensor based on ionic dielectric layer with hierarchical ridge microstructure. *Sensors and Actuators A: Physical* **313**, 112218 (2020a).

Q. Zou, S. Li, T. Xue, Z. Ma, Z. Lei, and Q. Su. Highly sensitive ionic pressure sensor with broad sensing range based on interlaced ridge-like microstructure. *Sensors and Actuators A: Physical* **313**, 112173 (2020b).

P. Zubko, G. Catalan, and A. K. Tagantsev. Flexoelectric effect in solids. *Annual Review of Materials Research* **43** (2013).